Coherent Spin Control in a SU(N) Quantum Gas of Strontium-87

Doctoral Thesis
Presented by
Husain AHMED

in partial fulfillment of the requirements for the degree
of
Doctor of Philosophy(PhD)

Submitted to the INSTITUT GALILÉE

UNIVERSITÉ
SORBONNE
PARIS NORD

Carried out at Laboratoire de Physique des Lasers

Defended in December, 2024

In front of the jury composed of:

M.	Alexandre GAUGUET	Rapporteur
M.	Patrick CHEINET	Rapporteur
Mrs.	Mathilde HUGBART	Examiner
M.	Sebastien BIZE	Examiner
M.	Gabriel DUTIER	Examiner
M.	Bruno LABURTHE-TOLRA	Thesis co-supervisor
M.	Martin ROBERT-DE-SAINT-VINCENT	Thesis co-supervisor

ABSTRACT

Ensembles of large-spin $S > 1/2$ atoms offer richer potential applications in areas like quantum computing, quantum simulations, and quantum magnetism as compared to what is possible with effective spin-half $S = 1/2$ atoms. For instance, in quantum simulations, large-spin atoms can be used to simulate high-spin models in optical lattices or traps which are crucial for exploring strongly correlated systems and high T_c superconductivity. Moreover, in quantum computing, atoms with large spins enable more complex forms of quantum entanglement because of the multiple spin degrees of freedom that can be simultaneously entangled. These systems can serve as qubits with higher dimensions (qudits) and enable more complex quantum gate operations. Furthermore, in quantum magnetism, atoms with large spins can exhibit SU(N) symmetry in their interactions (N being $2S + 1$). In such systems, instead of traditional spin-1/2 particles interacting through simple spin-exchange mechanisms, there can be higher-rank spin interactions that can lead to richer quantum magnetism.

In this thesis, Firstly, I present experimental results for manipulating the nuclear spins of ultracold atoms of ^{87}Sr. To achieve spin state selectivity, a tensor light shift is introduced into the ground state manifold. Then a two-photon Raman transition between two spin states enables us to control the final spin state deterministically. We can drive adiabatic Raman passages between the selected two spin states with a one-way efficiency of 80%. These passages are efforts towards realizing the superexchange interactions when are done inside optical lattices. In the future, this work will lead us closer to investigating quantum magnetism.

Secondly, I show that we can perform Ramsey interferometry between the chosen two spin states. Taking advantage of a large spin manifold of ^{87}Sr, we developed two interferometers that utilize a series of unitary rotations between the two chosen spin states. These interferometers are run with four spin states. The first interferometer measures the tensor light shift and the combination of vector light shift and linear Zeeman splitting in one shot. The second interferometer is capable of measuring the two collective atomic variables simultaneously. This interferometer can be used to measure quantum correlations in one shot. In general, these interferometric ideas can be applied to quantum computing and metrology.

At last, I present our first result on the measurement of SU(N) symmetry within the ground state of ^{87}Sr with the help of Ramsey interferometry. There are two measurements: one in the 1D lattice and the other in bulk gas. I observe the SU(N) asymmetry to be smaller than the relative uncertainty 10^{-2}, where the theoretical prediction is about 10^{-9}. Subsequently, I outline the immediate objectives to lower this uncertainty by an order of magnitude. This measurement leads us towards a better understanding of atoms with large spins that can exhibit SU(N) symmetry.

CONTENTS

1

INTRODUCTION

Significant progress has been made in quantum computing, metrology, and quantum simulation because of the ability to manipulate atomic spins with great precision and long coherences. Ultracold atoms offer a highly versatile platform to achieve these goals. For instance, in metrology, ultracold atoms play a significant role in precise measurements and tests for fundamental physics [Aidelsburger et al., 2022; Derevianko and Katori, 2011; Giovanazzi, 2005]. When trapped in optical lattices, they provide a tunable platform to study quantum many-body dynamics [Bloch et al., 2008; Buluta and Nori, 2009; Gross and Bloch, 2017]. Ultracold atoms with SU(N) symmetry offer a platform for higher-dimensional entanglement and enhanced quantum information processing [Miguel A Cazalilla and Rey, 2014a; A. V. Gorshkov et al., 2010; Taie, Takasu, Sugawa, Yamazaki, Tsujimoto, < f. R. Murakami, et al., 2010]. These platforms are also useful for simulating magnetism under SU(N) symmetry, which opens the door to the study of exotic quantum phases because N can be substantially bigger than two [Aguado and Vidal, 2008; Greiner et al., 2002; Schulte et al., 2008]. These versatile properties bring ultracold atomic systems to the forefront of research in quantum technologies and fundamental physics.

Quantum simulation

In recent years, interest in quantum simulation has been rapidly growing. One of the reasons is that technologies required for coherent control of quantum systems are reaching the stage of practical applicability. Quantum simulation is a valuable tool throughout numerous active research fields in physics, chemistry, and even biology [Georgescu et al., 2014; Kassal et al., 2011; Outeiral et al., 2021]. For instance, quantum simulation offers a technique to address several challenging issues in condensed matter physics, including high-Tc superconductivity and quantum magnetism. Other potential applications of quantum simulation are in the areas including high-energy physics, quantum chemistry, cosmology, nuclear physics, etc [Georgescu et al., 2014]. A quantum simulator can be built on several platforms like atoms in optical lattices, trapped ions, atomic spins, superconducting circuits, spins in semiconductors, etc [Buluta and Nori, 2009; Georgescu et al., 2014].

Neutral atoms in optical lattices offer an excellent platform for building a quantum simulator due to their tunability and minimal defects. One key experimental advantage of optical lattices is that they allow for the manipulation of lattice geometry and dimensionality by simply adjusting the intensity, frequency, or phase of the lasers used for creating the optical potentials [Bloch et al., 2008; Georgescu et al., 2014; Gross and Bloch, 2017]. Therefore, atoms in optical lattices have shown to be highly flexible, providing control over key factors such as coupling between internal quantum states, on-site interactions, and tunneling strength. Furthermore, both Bosonic and Fermionic atoms can be used for quantum simulation in optical lattices.

There are various implementations of neutral atom-based quantum simulators in different areas of physics. For instance, in condensed matter physics: Observation of quantum phase transition from superfluid to Mott insulating phase [Greiner et al., 2002], Simulating a chain of interacting quantum ising spins [Simon et al., 2011], dynamics of Bloch oscillations in disordered lattice potential [Schulte et al., 2008], and the also observation of Anderson localization [Billy et al., 2008]. In addition to these experiments, there are theory models such as describing topological order [Aguado and Vidal, 2008]. The applications of quantum simulators take us beyond condensed matter physics, for example, in high energy physics: quantum simulation for lattice gauge theories [Aidelsburger et al., 2022] and a proposal for quantum simulation of Dirac-Weyl fermions using ultracold atoms in a 2D optical lattice [Lan et al., 2011]. In cosmology: to study Hawking radiation [Giovanazzi, 2005].

Quantum computing

Several physical platforms can be utilized to build a quantum processor [Ladd et al., 2010]. Among them, arrays of single neutral atoms manipulated by light beams appear as a very powerful and scalable technology to manipulate quantum processors with up to a few thousand qubits [Henriet et al., 2020]. The control achieved at the single-particle level in optical trap arrays, while preserving the fundamental properties of quantum matter such as coherence and entanglement makes these technologies prime candidates for implementing disruptive computation paradigms. [Saffman, 2016].

Metrology

Ultracold atoms also play a crucial role in metrology, atom interferometry, and tests of fundamental physics due to their precise controllability. They provide unmatched

accuracy in atom interferometry and are a critical tool in probing the fundamental tests for gravity [Canuel et al., 2018; Jeffrey B Fixler et al., 2007; Peters et al., 2001]. When employed in atomic clocks that have achieved unprecedented accuracy, reaching fractional uncertainties at the 10^{-18} level [Derevianko and Katori, 2011], and the list goes on.

Alkaline earth atoms (AEA)

Whether to build a quantum simulator, quantum computer, or a device for metrological purposes, the central question is always coherence and entanglement. AEA naturally have a long coherences due to their weak sensitivity to external magnetic fields. This property arises because of the closed-shell electronic configuration in the $^1S_0$ ground state, which is decoupled from external magnetic fields. Furthermore, some of the fermionic species have a rich hyperfine structure and nuclear spin greater than $1/2$, which provides the possibility to entangle more than two quantum states. Atoms like ^{87}Sr allow for the encoding of higher-dimensional entangled states, which can be used to simulate complex quantum systems.

One of the most appealing properties of AEA is an emergent SU(N) symmetry in the nuclear spin degrees of freedom. They can be used to study many-body phenomena characterized by the SU(N) group with N as large as 10 [Alexey Vyacheslavovich Gorshkov et al., 2010]. For instance, the realization of the SU(6) Hubbard model by loading a nuclear spin mixture of ^{173}Yb atoms in a 3D lattice [Taie, Takasu, Sugawa, Yamazaki, Tsujimoto, < f. R. Murakami, et al., 2010]. On top of this experiment, various theoretical studies involving quantum magnetism beyond SU(2) symmetry have been done [Miguel A Cazalilla, A. Ho, et al., 2009; Hermele et al., 2011].

^{87}Sr, with the largest nuclear spin, I = 9/2, in the atomic ground state $^1S_0$, is an ideal candidate for the study of magnetism in enlarged SU(N) symmetry. Furthermore, the atom has unique atomic properties like narrow linewidth $^1S_0 \leftrightarrow {}^3P_0$ and insensitivity to external perturbations due to the closed shell, which make them ideal for the realization of ultra-precise atomic clocks. Fermionic AEA, such as Sr or Yb, are used in state-of-the-art optical atomic clocks [Derevianko and Katori, 2011].

Strontium 87

^{87}Sr atoms are widely used in cold atom experiments due to their unique electronic structure and properties such as narrow optical transitions, and long-lived metastable

states. The first quantum degenerate gas of ^{87}Sr was realised [DeSalvo et al., 2010]. Since then, the strontium clocks became popular beating the precision of previous clocks [Baillard et al., 2008; Blatt et al., 2008; Martin M Boyd et al., 2007; Le Targat et al., 2006]. These clocks have already surpassed the accuracy of the Cs standard with a fractional uncertainty of 10^{-18} [Andrew D Ludlow, Zelevinsky, et al., 2008]. People have explored relativistic time dilation by comparing ^{87}Sr clocks at different heights, testing general relativity with unprecedented precision [Lisdat et al., 2016].

Furthermore, in interferometry, ^{87}Sr atom interferometers are used for precise gravitational measurements [Poli et al., 2011]. Two-dimensional superfluidity and phase coherence in ^{87}Sr optical lattices are observed, providing insights into quantum phase transitions [Büchler et al., 2007].

In our experiment, we utilize 7.4 kHz narrow intercombination line $^1S_0 \leftrightarrow ^3P_1$ of ^{87}Sr. The hyperfine splitting of the state $^3P_1$ is several orders of magnitude larger than the linewidth of this line. Therefore, this transition offers ideal conditions for realizing spin-orbit coupling schemes with less spontaneous emission [Miguel A Cazalilla and Rey, 2014a]. The fine structure splitting caused by spin-orbit coupling allows precise control over the energy levels in the ground state manifold $^1S_0$. It contributes to the stability of the optical transitions used in precision measurement-related experiments.

Our experiment deals with ultracold gases of ^{87}Sr. The first path of the experiment is to explore collective phenomena such as quantum magnetism with ^{87}Sr atoms loaded in the optical lattices. In particular, the geometry of the spin-independent lattice in our experiment is designed to realize the 2D Fermi-Hubbard model [Das et al., 2024] with the atoms of ^{87}Sr with enlarged SU(N) symmetry. Using a spin-dependent lattice [André Heinz et al., 2020] on top of the spin-independent one, we will be able to write the spin texture realizing Néel spin order [Mazurenko et al., 2017]. By adjusting the depth of the spin-independent lattice the dynamics of the spins interactions can be tuned. It will be possible to slowly approach the regime where many-body physics is driven by super-exchange interactions, within a spin-independent lattice. These interactions that can result in the squeezing of the alternate magnetization [Comparin et al., 2022] that can be probed by the same spin-dependent lattice.

In addition, the second direction of the experiment is to realize physics in the bulk gases. Taking advantage of the large spin symmetry of strontium atoms, there is the possibility to generate ideas based on high dimensional interferometry. These schemes are useful in building a quantum sensor and quantum processor.

Therefore, my PhD thesis is divided roughly into two sections. Initially, I set up a path to investigate many-body physics in optical lattices. Second, I make use of ^{87}Sr's large spin (N=2I+1=10) symmetry to construct two interferometric schemes and a test to measure the SU(N) symmetry.

THESIS OVERVIEW

The first chapter highlights the experimental results for coherent spin manipulation in the ground state manifold of ^{87}Sr. At the beginning of the chapter, I described the theoretical calculation of spin-dependent light shifts associated with the narrow intercombination line. Using spin-dependent light shifts, we can manipulate the nuclear spin states with low spontaneous emission. To accomplish this, we lift the degeneracy within the $^1S_0$ ground state manifold. Then, we isolate and manipulate a system of two nuclear spin states from the entire manifold. Our technique relies on a two-photon Raman transition. I demonstrate an experimental result for an adiabatic scheme to selectively and coherently manipulate the two selected nuclear spin states of ^{87}Sr. We achieved adiabatic passages with a one-way efficiency of approximately 80%, restricted by the spontaneous emission rate. With ongoing improvements in the experimental setup, the efficiency is expected to reach 97%. These results are presented in bulk gases. Then, I outline the configuration of a 3D lattice to achieve this coherent manipulation locally on each alternative lattice site. In the future, this spin manipulation in the lattice will be used to write spin textures and study spin-spin interactions.

Furthermore, I show the coherent Rabi oscillations between the nuclear spin states that differ by $\Delta mF = 1$. I present the experimental results for Rabi oscillations between three pairs of nuclear spin states. Then, I discuss the coherence associated with these Rabi oscillations. I improved the coherence time from 5 ms to 300 ms approximately by changing the waist of the beam that drives the two-photon Raman transition. After the improvement, we observe the Rabi oscillations with a quality factor Q ~ 100. Finally, I present a scheme to achieve coherent coupling of the nuclear spin states that differ by $\Delta mF = 2$.

In the second chapter, I present the result of Ramsey interferometry within two isolated nuclear spin states. Using a Ramsey interferometer, I show the measurement of the coherence time of the qubit state associated with the nuclear spin states. First, in the presence of an external magnetic field and the light used to generate the spin-

dependent light shift. We observed a coherence time of roughly 50 ms limited by the variations in the vector light shift from the light. Second, which is only in the presence of the external magnetic field the coherence time is observed to be comparable to the lifetime of the Fermi gas which is of the order of a few seconds.

Next in this chapter, I present two interferometric schemes involving four nuclear spin states. In these schemes, a series of two spin-state unitary operations are applied within the four spin-state manifolds. The first interferometric scheme measures the tensor light shift and the combination of vector light shift and linear Zeeman splitting in one shot. This type of interferometer can be used to sense multiple fields at once. The second interferometric scheme is capable of measuring the two or more collective atomic variables simultaneously. This interferometer can be used to measure quantum correlations and performs tomography in one shot. Lastly, I highlight the different types of noises that appears as uncertainty in our interferometric results.

In the last chapter, I present our first result on the measurement of SU(N) symmetry within the ground state of ^{87}Sr with the help of Ramsey interferometry. There are two measurements: one in the 1D lattice and the other in bulk gas. I observe no SU(N) asymmetry with a fractional uncertainty of 10^{-2}, where the theoretical prediction is about 10^{-9}. Subsequently, I outline the immediate objectives to increase this uncertainty by an order of magnitude, which is 10^{-3}.

2 | MANIPULATION OF NUCLEAR SPIN STATES OF ^{87}Sr

ermionic ^{87}Sr has a large nuclear spin I=9/2, which offers a platform to work with ten (2I+1) nuclear spin states. External magnetic fields have a very weak coupling to these ten nuclear spin states because the ground state $^1S_0$ of Fermionic ^{87}Sr has a closed electronic structure. Therefore, it is impractical to probe and manipulate these nuclear spin states in the ground manifold with external magnetic fields. On the other hand, for fermionic ^{87}Sr, the excited states with J $\neq$ 0 couples the total momentum J with the large nuclear spin I=9/2 such that the orbital degrees of freedom are mixed and entangled with the spin degrees of freedom. For instance, the excited state $^3P_1$ with angular momentum J = 1 is split into three hyperfine states F = 11/2, 9/2, 7/2. These hyperfine states are separated over ∼ 2.6GHz, which makes them highly resolved compared to the line width of the optical transition $\Gamma/2\pi$ = 7.4 kHz. Due to this property of the ^{87}Sr atom, the polarizability associated with this intercombination line can be highly sensitive to the nuclear spin states in the ground manifold, with low spontaneous emission.

The spin-dependence of polarizability allows us to engineer spin-dependent light shifts that can be used for resolving, manipulating, and probing the nuclear spins [C. Shi et al., 2015]. Manipulation of nuclear spins offers a platform for studying quantum many-body phenomena in optical lattices with an emergent SU(N) symmetry [M A Cazalilla et al., 2009; Taie, Yamazaki, et al., 2012]. It can be achieved in alkaline earth metals like strontium and ytterbium. Particularly in the case of strontium, the N can be up to 10. Moreover, the Fermi mixture of alkaline earth metals opens the door to discovering novel quantum phases of matter [Tey et al., 2010]. Measurement of these phenomena requires probing nuclear spins. One such scheme for spin-dependent imaging has been demonstrated for strontium [Stellmer et al., 2011a].

In this chapter, I will first recall a brief introduction to the estimation of these spin-dependent light shifts and the scattering rate associated with them. A detailed version of the mathematical calculations is presented in the thesis [Litvinov, 2023]. I will demonstrate that our Raman spectroscopic scheme allows us to measure these

spin-dependent light shifts in the experiment. Then, I will present the experimental measurement of the scattering rate associated with spin-dependent light shifts, which is approximately three times higher than the expected value. This is explained based on amplified spontaneous emission which is being solved by the filtering cavity.

In our experimental setup, we use an optical beam that I will call *beam 1* to lift the degeneracy of the ground manifold quadratically. Combined with *beam 1*, a second beam *beam 2* is used to select and couple two spin states coherently and deterministically via a two-photon Raman process. I will show how we isolate a two-level system of two spin states from an entire ground state manifold to drive coherent Rabi oscillations between them. This is achieved by minimizing the ratio of the Rabi couplings associated with *beam 2* and *beam 1*. We achieved the Rabi oscillations between the spin states that differ by $\Delta m_F = 1$ and $\Delta m_F = 2$. With our scheme, we can manipulate up to 10 spin states coherently across the entire $^1S_0$ manifold. In addition, it is possible to carry out adiabatic passages with spin selectivity across 10 different spin states with 80 % one-way efficiency. Finally, I will provide an outlook for a scheme for the spatial selectivity of the spin-dependent light shifts.

2.1 SPIN DEPENDENT LIGHT SHIFTS

2.1.1 Tensor polarizability with intercombination line

In the presence of hyperfine structure, the AC Stark shift can depend on the spin states, i.e. the Zeeman sub-levels. The calculation of this AC Stark follows straight from the second-order perturbation theory. In this section, I will briefly describe the light shift calculation that depends on the spin states, which I will refer to as $|m_F\rangle$. Some references contain the calculation of atomic tensor polarizability for Rb and Sr with experimental verification [M. Safronova and U. Safronova, 2011; C. Shi et al., 2015; Steck, 2001]. Please refer to [Varshalovich et al., 1988] for the theory of angular momentum, particularly spherical tensors.

Interaction Hamiltonian between an electric dipole atom $\vec{d}$ under the dipole approximation and the monochromatic light $\vec{E}$ can be written as $\mathcal{H} = -\vec{d}.\vec{E}$. Where the light field can be described as $\vec{E} = \frac{1}{2}\vec{\epsilon}|E|e^{i(\omega_l t + \phi)} + cc$. This monochromatic light has the frequency $\nu_l = \omega_l/2\pi$. Under an approximation where the wavelength of the light is much larger than the typical size of the atom, the amplitude of the electric field felt by the atom is constant over the spacial size of the atom. Starting from the second-order

perturbation theory, we can calculate the light shift produced by the laser atom inter-
action Hamiltonian described above. The result is called AC stark shift and given by
the general expression.

$$\Delta E = -\frac{1}{4}\alpha|\mathbf{E}|^2 \tag{2.1.1}$$

where $\alpha = \alpha(\alpha_s, \alpha_v, \alpha_t)$ is the polarizablity of the atom. This polarizability has a
scalar part α_s which is independent of m_F, a vector α_v part that has a linear depen-
dence on m_F and a tensor α_t component that has a quadratic dependence on m_F. The
state of an atom in hyperfine basis is described by the quantum numbers $|n, J, F, m\rangle$,
where symbols have their usual meanings. In this chapter for the manipulation of
nuclear spins, we will be addressing the intercombination line $(5S^2)^1S_0 \leftrightarrow (5S5P)^3P_1$.
There is no change in the value of the principal quantum number n for this transition.
Therefore, the state of the atom can be fully described by the quantum numbers $|F, m\rangle$,
where F=J+I. Overall, the AC Stark shift which leads to π transition only is given by
[M. Safronova, U. Safronova, and Porsev, 2013]:

$$\Delta E = -\frac{1}{4}\vec{E}_\pi^* \cdot \vec{E}_\pi \sum_{F'} \frac{|\langle F, m |\vec{d} \cdot \vec{\epsilon_\pi}| F', m \rangle|^2}{\hbar\Delta_{F,F'}} \tag{2.1.2}$$

Where $\Delta_{F,F'}$ is the energy difference between the states $|F\rangle$ and $|F'\rangle$. $|F'\rangle$ is the excited
state. Furthermore, the effective two-photon Rabi coupling for these states for an
arbitrary polarization of the laser is given by:

$$\hbar\Omega_{eff} = -\frac{1}{4}\vec{E}_{q_2}^* \cdot \vec{E}_{q_1} \times$$

$$\sum_{F',q_1,q_2} \frac{\langle F, m + q_1 - q_2 |\vec{d} \cdot \vec{\epsilon}_{q_2}| F', m + q_1 \rangle \langle F', m + q_1 |\vec{d} \cdot \vec{\epsilon}_{q_1}| F, m \rangle}{\hbar\Delta_{F,F'}} \tag{2.1.3}$$

where $(q_1, q_2) = (0, \pm 1) = (\pi, \pm\sigma)$ depending upon the polarisation of the light.
Notice the conservation of angular momentum, the initial spin state $|F, m\rangle$ coupled to
excited state $|F', m + q_1\rangle$ via polarization q_1, similarly the excited state $|F', m + q_1\rangle$ is
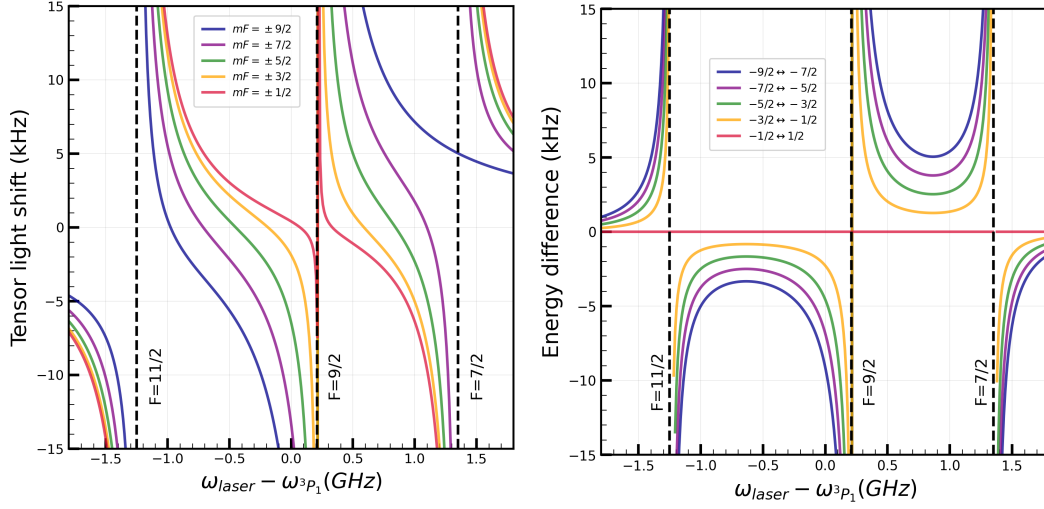coupled to another spin state in the ground manifold $|F, m + q_1 - q_2\rangle$ via polarization
q_2.

Figure 1: Left: Numerical estimation of spin-dependent tensor light shift when the laser frequency scanned over the hyperfine structure of $^3P_1$ state. The parameters in *beam 1* such as laser power are kept at 4.5 mW with a waist of 320 μm felt by the atoms. Right: For the same light shift, expected resonances between neighboring $|m_F\rangle \leftrightarrow |m_{F+1}\rangle$ spin states. On both the plots, black dashed lines represent the three hyperfine resonances in $^3P_1$ state. The color scheme represents different m_F spin states. It should be noted that the detuning of the laser from the excited state is in GHz.

To summarise, we observe that there is spin dependence in the polarizability. The light shift over the entire manifold m=2F+1 can be calculated using the equation 2.1.2. The equation 2.1.3 gives the effective Rabi coupling between the spin state $|F, m\rangle$ and $|F, m + q_1 - q_2\rangle$. The two equations are sufficient to calculate the matrix elements for the Hamiltonian $\mathcal{H}$ for the second-order processes. Furthermore, the light shift is quadratic. Therefore, we can select and isolate the two spin states from the entire manifold of several spin states, as we shall see later in this chapter. Dipole matrix part $\left\langle F, m_1 \left| \vec{D} \cdot \vec{\epsilon}_\pi \right| F', m_2 \right\rangle$ can be calculated with the help of dipole reduction methods such as Wigner-Eckart theorem. Where m1 and m2 can be arbitrary. These matrix elements depend upon the atomic properties only for a given polarization of light. Upon solving the algebra, we can estimate the light shift and effective Rabi couplings over the entire manifold.

The spin-dependent light shift in kHz for the intercombination line $^1S_0 \leftrightarrow ^3P_1$ for a π polarized light is shown in the figure left 1. As the frequency of the light is scanned over the hyperfine structure of the excited state $^3P_1$, we can see the divergence of the light shifts at the location of three hyperfine resonances F=11/2,9/2,7/2 respectively. We also observe that all the spin states $|m_F\rangle$ experience from attractive to repulsive AC

Stark shift, which makes this spin-dependent potential highly tunable. Furthermore, based on the simulation (not shown here), light shifts for $\sigma^+ + \sigma^-$ polarized light were calculated. In this case, the lower values of Clebsch–Gordan (CG) coefficients resulted in less resolved spin states. The energy difference between the two successive $|m_F\rangle \leftrightarrow |m_F + 1\rangle$ spin states are plotted as a function of $\omega_{laser} - \omega_{3P_1}$ in the picture on the right. Between F=11/2 and F=7/2 resonances, the transitions weakly depend upon ω_{laser}, except at the resonance where they diverge. This results in a highly robust selection of spin states over a wide frequency range compared to the linewidth Γ_{3P_1}. We notice that for the π polarized light, the spin states with high $|m_F\rangle$ are resolved better, whereas the spin states with $m_F = \pm 1/2$ are least resolved.

We now have calculated the light shift associated with the intercombination line. For π polarized light and a given detuning $\omega_{laser} - \omega_{3P_1}$, the light shifts are known theoretically. The next step is to calculate the associated scattering rate.

2.1.2 Scattering rate associated with the intercombination line

Spontaneously emitted photons from an atom in the excited state $^3P_1$ to the ground state $^1S_0$ possess random polarization. Because of this, the atom's ground state manifold experiences stochastic changes in its spin states, which disperse the spin states over the $|m_F\rangle, |m_{F+1}\rangle, |m_{F-1}\rangle$ manifold (assuming the atom's initial state was $|mF\rangle$). This redistribution of spin states results from the selection rules governing dipole transitions, which allow changes in the magnetic quantum number m_F by ± 1 or 0, depending on the polarization of the emitted photon. As a consequence, we lose the control over spin selectivity. Therefore, it's crucial to understand and quantify the photon scattering rate. The imaginary part of the polarizability in the equation 2.1.3 directly corresponds to the photon scattering rate.

The left figure in 2 shows the scattering rate as the laser frequency is scanned over the hyperfine structure of the excited state. As the laser frequency is close to F=9/2, larger spin states $|m_F|$ experience maximum light shifts accompanied by a greater scattering rate. While near F= 11/2 and F=7/2, smaller spin states $|m_F|$ are shifted more with a greater scattering rate. The energy difference between two neighboring spin states is compared to the mean scattering rate of the spin states to analyze the two situations. The ratio of these lights shift between two neighboring spin states to the mean scattering rate is plotted in the figure 2 right. We observe that the optimal ratio occurs within the frequency range surrounding the resonance frequency for F=9/2, typically at -0.4 GHz and 0.7 GHz. It also worth noticing that the larger the $|m_F|$,
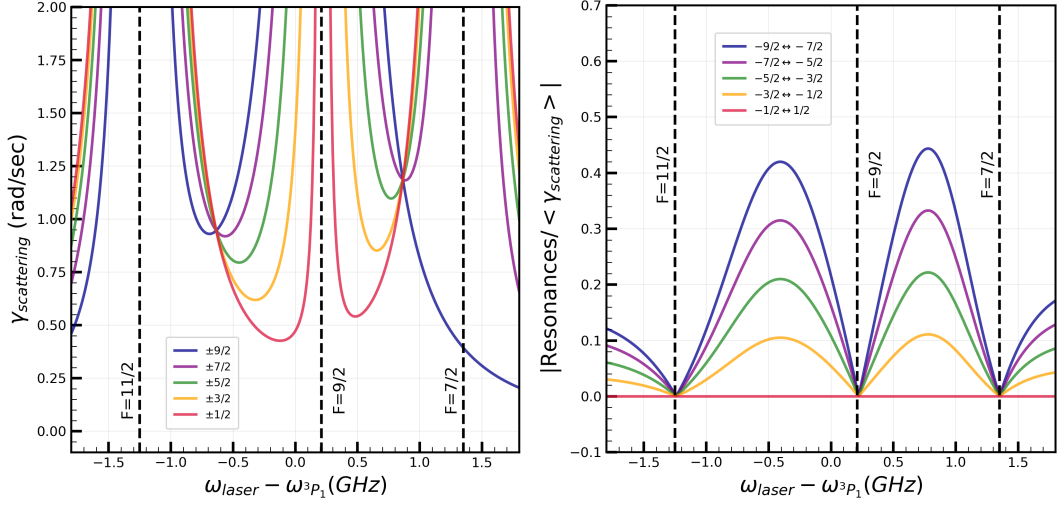
Figure 2: The figure shows an estimation of the scattering rate for the intercombination line. The frequency of the laser is scanned over the hyperfine structure in the excited state $^3P_1$. The laser power in *beam 1* is kept at 4.5 mW with a beam waist 324 μm and polarization π. Left: Scattering rate in rad/sec for each spin state $|m_F\rangle$. Right: Light shifts between neighboring spin states $|m_F\rangle \leftrightarrow |m_{F+1}\rangle$ over the mean scattering rate for each spin state. Different color of lines shows each spin states m_F.

the better is the optimization for the light shift to scattering rate ratio. We will later use this fact for various schemes for spin manipulation in this chapter. Since we can characterize the spin-dependent light shifts and scattering rate associated with them, we shall now move on to the experimental realization of the two quantities.

2.2 PREPARATION FOR NUCLEAR SPIN MANIPULATION IN THE GROUND STATE MANIFOLD

This section aims to experimentally show how we prepare for coherently manipulating two spin states within the ground state manifold. We want to achieve this goal with minimum spontaneous emission. Therefore, we lock the laser responsible for inducing spin-dependent light shift at the detuning of -600 MHz from the excited state F=9/2, $^3P_1$. Since the tensor light shifts are quadratic, we can isolate the two-level system from the entire ground state manifold to engineer coherent processes like spin-selective adiabatic passages and spin-selective Rabi oscillations.

I will start this section by explaining the experimental setup we have designed to achieve our objectives. With the help of the Raman resonance scheme, we identify the resonances between spin states $|m_F\rangle \leftrightarrow |m_F + 1\rangle$ quantifying the spin-dependent light shifts. Then, I will compare the experimental results of the measurement of spin-dependent light shifts with the theoretical estimation in the previous section. Finally, We will measure the scattering rate associated with spin-dependent light shifts and compare it with the expected value.

In our experiment, the oven's temperature is set to 770 K, corresponding to an outgoing with Boltzmann velocity distribution with a most probable axial velocity of about v ~ 500 m/s. This hot atomic vapor is optically collimated with 2D optical molasses. Then, the axial flux of atoms is slowed with a 50 cm long Zeeman slower, and the axial velocity of the atoms reaches from v ~ 500 m/s to the capture velocity of about 20 m/s of our broadband MOT.

The atoms are then captured in a 3D MOT, which is on the broad-band transition $^1S_0 \leftrightarrow^1 P_1$ at 461 nm and cooled down to a Doppler limit T_D ~ 1 mK corresponding to this transition. This transition is not cyclic, and atoms are continuously shelved from the ground state into the state $^3P_2$. The temperature of the atoms accumulated in $^3P_2$ is approximately the Doppler temperature of the broad-band MOT, which is too hot to be directly loaded in the optical dipole trap for the next stage of optical cooling. To achieve optical cooling effectively, we employ a second narrow MOT stage, which necessitates that the atoms are in the ground state. Therefore, we use the optical transition $^3P_2 \leftrightarrow 5s6d^3D_2$ at 403 nm to repump atoms back in the ground state with a two-photon radiative decay through $^3P_1$.

The second optical cooling stage in our experiment is associated with the 7.4 kHz intercombination line $^1S_0 \leftrightarrow^3 P_1$ at 689 nm. The laser used for this cooling has a spectrum that is as narrow as 1 kHz which is sufficient for the targeted 7.4 kHz linewidth. In the final narrow MOT stage, the bulk gas of ^{87}Sr extends over nearly 600 μm with 6 million atoms at T ~ 3 μK.

The 1070 nm laser beams used to create an optical dipole trap are activated right after the narrow MOT stage. The atoms are attracted by the dipole trap of depth nearly 50 μK. The gas is finally cooled down to Fermi degeneracy, with forced evaporation inside the dipole trap. A typical forced evaporation runs over 8 to 10 seconds, and the gas reaches degenerate regime T $\leqslant$ 0.5 T_F with approximately 4000 atoms per spin state. Throughout this thesis, the experiments are done on this Fermi gas.

LASER COOLING BROAD LINE (Doppler limited)	REPUMPING	LASER COOLING NARROW LINE (Recoil limited)	EVAPORATION IN DIPOLE TRAP	DEGENERATE FERMI GAS
• 461 nm • Oven: 500°C (500m/s) • Blue MOT:~ mK	• 403 nm	• 6M atoms • T ~ 3 μK	• 2.5M atoms • $a_S = 97 \, a_0$ • Lifetime ~ 8 s	• **~40000 atoms** • **T ~ 40-100 nK** • **Typically: T/T_F ~ 0.15-0.40**
• 5-10 s	• ~ 10 ms	• ~ 300 ms	~ 5-10 s	
		Time of the experimental cycle		

Figure 3: Typical parameters at each experimental stage for producing the Fermi gas.

2.2.1 Experimental setup for spin dependent light shifts

The Moglabs laser [MOGLabs, n.d.] generates the spin-dependent tensor light shift. The red laser [Radiant Dyes Laser & Accessories GmbH, n.d.], which is utilized for laser cooling at the narrow MOT stage, is beat-locked with the Moglabs. We can beat-lock the Moglabs laser with minimal fluctuations because the red laser is ultra-stable. Considering the bandwidth of locking electronics, it's possible to tune the beat frequency generated by the two lasers within a 1GHz frequency window around the F = 9/2 resonance in the excited $^3P_1$ state. Therefore, we can lock the laser at the detuning of -600 MHz from the excited state F=9/2, $^3P_1$.

The optical setup used for creating spin-dependent light shifts on the atoms is illustrated in figure 4. In the figure, a PBS is used to split the main optical beam into two beams. This setup includes two independent optical beams controlled by separate AOMs. The first beam, which controls spin-dependent light shifts in the ground state $^1S_0$, will be named *beam 1* in this thesis. The second beam is orthogonal to *beam 1* in terms of polarization and will be called *beam 2*. The RF drive of the two AOMs that control the frequency of two beams is from the same direct digital synthesizer (DDS), which makes the two beams' phase coherent. The two beams combined through a PBS before being injected inside the same optical fiber. Injecting both beams in the same optical fiber aligns them simultaneously on the atoms. Since both beams come to the experimental cell from the same optical fiber, both beams are naturally superimposed. The two distinct polarizations cannot be maintained as precisely as they would be if the optical fiber contained a single polarization, which is a disadvantage of this setup. But our scheme is robust enough to drive coherent Rabi oscillations with sufficiently long coherence time as I will explain later in the chapter 2.5.2.
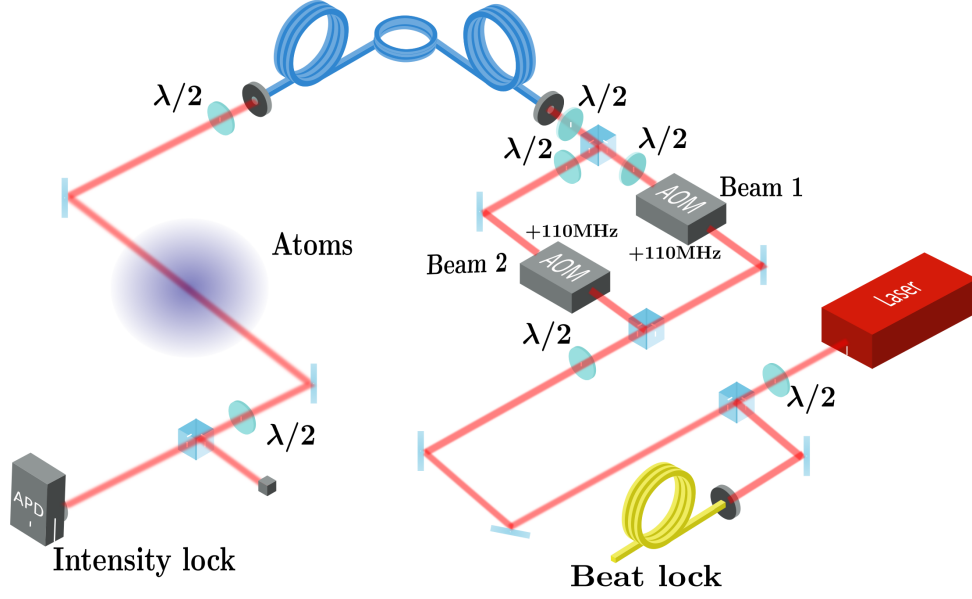
Figure 4: The above figure shows an optical setup designed to create spin-dependent light shifts and to facilitate various processes that are selective to spins. The master laser of this setup is beat-locked with the red laser used for laser cooling. The master laser's optical beam is split into two beams using a PBS. Each of these two beams is controlled independently using two acousto-optical modulators. Throughout the chapter, I will refer to these two beams as *beam 1* and *beam 2*. Before injecting into the same fiber, these two beams again combined with orthogonal polarization.

Furthermore, in all our experiments, the quantization axis is set parallel to the direction of the electric field wavevector of *beam 1* meaning the $\vec{B}\|\vec{E}$, where $\vec{B}$ is the external magnetic field. Therefore, the polarization of *beam 1* is π. The polarization of *beam 2* is $\sigma_+ + \sigma_-$ in this particular frame. The waist of the two beams at the atoms is measured to be $320 \pm 5\mu m$. The experimental configuration that will be utilized for the coherent manipulation of the spins is now complete. Now, we are ready to drive a two-photon process with this scheme of two orthogonal beams. One can think of this process as the absorption of a π photon in *beam 1* and emission of a $\sigma_\pm$ photon in *beam 2* and vice versa.

2.2.2 Resonance spectroscopy of tensor light shifts

Resonance spectroscopy allows us to measure spin-dependent light shifts and identify all the ten resonances m_F's in the ground state manifold $^1S_0$. I will show three of these resonances $|-5/2\rangle \leftrightarrow |-7/2\rangle, |-5/2\rangle \leftrightarrow |-3/2\rangle, |-7/2\rangle \leftrightarrow |-9/2\rangle$ and compare them with the theoretical predictions. For this spectroscopy, we prepare Fermi gas initially
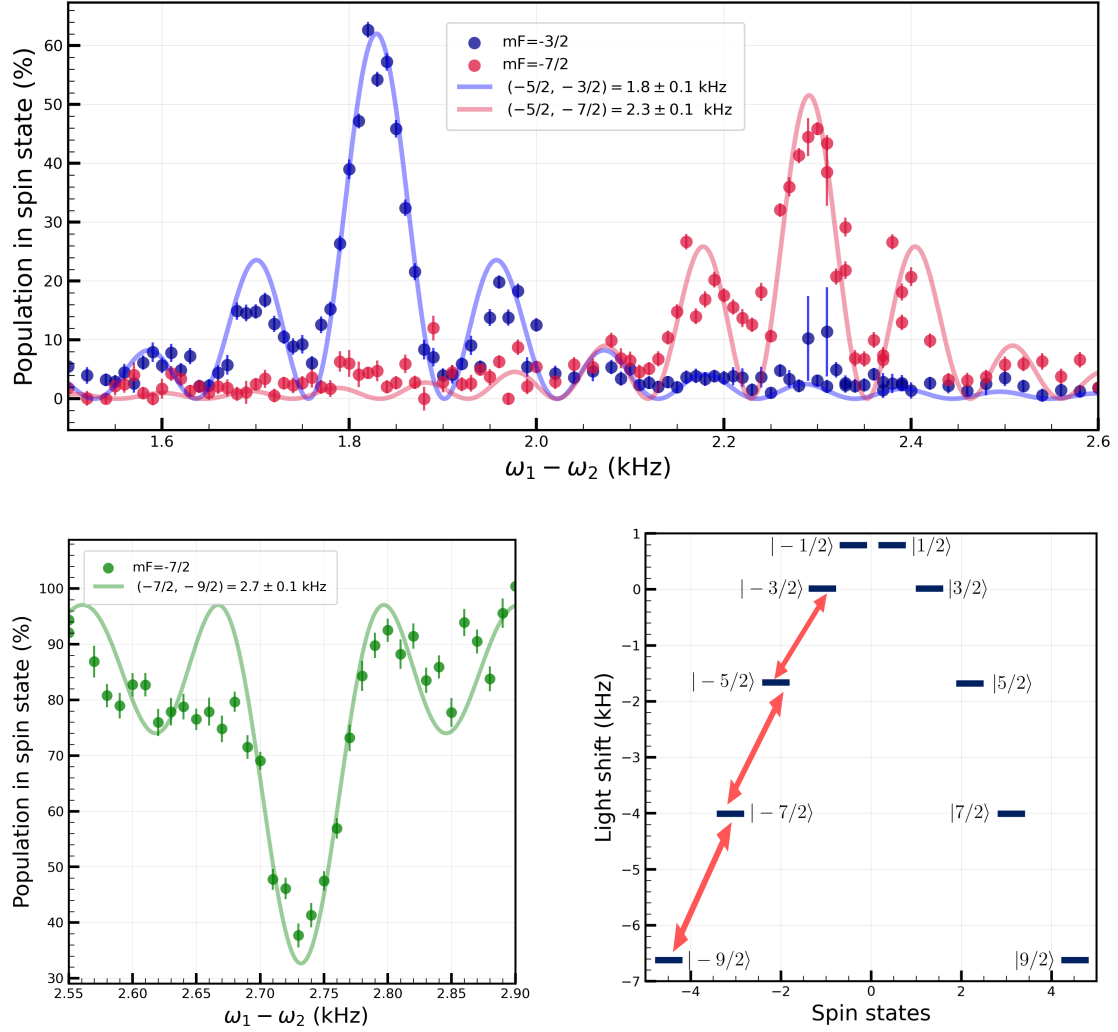
Figure 5: The figure shows experimental data observed from the Raman resonance spectroscopy scheme. Both the beams have the detuning $\Delta = -600\text{MHz}$ to the excited hyperfine state $F = 9/2, {}^3P_1$. The optical powers in the {*beam 1, beam 2*} are $\{4.5\text{mW}, 0.8\mu W\}$ respectively with the same beam waist of $320 \pm 5\mu\text{m}$. Up: blue dots represent the population of atoms in spin state $|-3/2\rangle$ for the resonance $|-3/2\rangle \leftrightarrow |-5/2\rangle$, and the red dots represent the population of atoms in spin state $|-7/2\rangle$ for the resonance $|-7/2\rangle \leftrightarrow |-5/2\rangle$. The graph displays the population of the target spin state for both resonances. Bottom left: green dots represent the population of atoms in the spin state $|-7/2\rangle$ for the resonance $|-7/2\rangle \leftrightarrow |-9/2\rangle$. The graph displays the population in the initial spin state. Bottom right: Figure representing the measured value of the resonances confirming the quadratic degeneracy lift. The figure is extended to cover the entire ground state manifold of ${}^{87}\text{Sr}$.

in the state $\text{mF} = |-5/2\rangle$ for all these resonances. In principle, we can choose any spin state as an initial state. An optical pumping sequence produces a mixture of a

desired spin state $|mF\rangle$ and $|-9/2\rangle$. Subsequently, an on-resonance pulse removes $|-9/2\rangle$ from the trap by radiation pressure. The whole process is described in detail here [Litvinov, 2023].

After the preparation of Fermi gas, the magnetic field is aligned adiabatically along the direction of the electric field vector of the *beam 1*. Then *beam 1* is turned on adiabatically to lift the degeneracy in the ground manifold quadratically. The intensity of this beam is locked to minimize fluctuations in intensity appearing as fluctuations in light shifts. At the locking point, the power of *beam 1* is set to approximately 4.5 mW, and power in *beam 1* may vary a bit depending on the day the experiment was performed. Afterward, the *beam 2* turned on with a 10-millisecond square pulse. The power of *beam 2* is kept at 0.8 µW to reduce the power broadening of the resonances. I chose 10 ms of pulse duration such that Fourier broadening of the resonance due to pulse time is less than the light shifts. The pulse time of *beam 2* cannot be arbitrarily long as the spontaneous emission from *beam 1* can depolarize the Fermi gas. The frequency of *beam 2* is tuned by the driving AOM to make the spectrum, which shows the resonances between states $|mF\rangle \leftrightarrow |mF \pm 1\rangle$. Depending on our choice, the spin-dependent momentum transfer technique [Bataille et al., 2020] can measure the initial spin state or target.

In order to do the spectroscopy, the frequency of *beam 2* was scanned within a few kHz range detuned from *beam 1*. Depending upon the detuning two resonances can be found $|-5/2\rangle \leftrightarrow |-3/2\rangle$ and $|-5/2\rangle \leftrightarrow |-7/2\rangle$. For our scheme that is with $(\pi - \sigma)$ configuration of the two beams, I look for the resonance in the neighboring states $|m_F\rangle \leftrightarrow |m_{F\pm1}\rangle$ only, I repeat this experiment with the initial state $mF = |-7/2\rangle$ to find the third resonance between $|-7/2\rangle \leftrightarrow |-9/2\rangle$. The populations in each spin state were fitted with the formula for the Rabi cycle in a two-level system to find the resonances. A detail about Rabi oscillations can be found in section 2.5.1. One important remark here is that the Rabi frequency is smaller than the width of the resonance. Hence, you can see Rabi cycles inside the resonance curves. In order to measure the resonances, the data is fitted with the eqaution:

$$P(t)_{m_F \to m_{F\pm1}} = \frac{\Omega_{eff}^2}{\Omega_{eff}^2 + (\delta - \delta_0)^2} \sin^2\left(\frac{\sqrt{\Omega_{eff}^2 + (\delta - \delta_0)^2}\,t}{2}\right) \tag{2.2.1}$$

This equation reads $\Omega_{eff} = \Omega_1 \Omega_2 / 2\Delta$ and $\omega_1 - \omega_2 = \delta$. $(\Omega, \omega)_{1,2} =$ are Rabi coupling and optical beam frequency for each beam respectively. Δ is the detuning to the excited state. Therefore, Ω_{eff} is the effective Rabi coupling. Expected resonances

occur when δ is equal to the respective energy difference δ_0 between the spin states $|m_F\rangle \leftrightarrow |m_{F\pm1}\rangle$.

Figure 5 shows the result of the experiment. In the figure, blue dots represent the population in the spin state $|-3/2\rangle$ for the resonance $|-3/2\rangle \leftrightarrow |-5/2\rangle$. Similarly for the resonance $|-7/2\rangle \leftrightarrow |-5/2\rangle$, population in the spin state $|-7/2\rangle$ is measured. For both the resonances the centre is found at $\{|-3/2\rangle \leftrightarrow |-5/2\rangle, |-7/2\rangle \leftrightarrow |-5/2\rangle\} = \{1.8 \pm 0.1, 2.3 \pm 0.1\}$ kHz. The figure on the bottom right shows the measurement of the resonance $|-7/2\rangle \leftrightarrow |-9/2\rangle$. The population in the initial spin state $|-7/2\rangle$ is measured. Hence, we see the depletion of the population. Furthermore, we observe that the resonance is not symmetric. The asymmetry arises because spin state $|-7/2\rangle$ starts to resonate with the spin state $|-5/2\rangle$ on the lower side of the frequency scan of this plot. However, the central peak of the oscillation is still symmetric for extracting information about the resonance center. After fitting this resonance, we find the center at 2.7 ± 0.1 kHz.

These overall shifts in the spin states come from the light shift created by the laser and the linear Zeeman shift created by the external magnetic field during spectroscopy. The linear Zeeman shift at this stage is 950 ± 50 Hz which comes from external magnetic field of 5 Gauss (Zeeman coupling constant of ~200 Hz/G). I did a theoretical estimation based on the equation 2.1.3 for the light shifts with the beam waist measurement of 320 ± 5 μm. The simulation involved the linear Zeeman shift due to the external field. The result predicts the three resonances $\{|-3/2\rangle \leftrightarrow |-5/2\rangle, |-7/2\rangle \leftrightarrow |-5/2\rangle, |-7/2\rangle \leftrightarrow |-9/2\rangle\}$ at a detuning of $\{1.78 \pm 0.05, 2.23 \pm 0.09, 2.84 \pm 0.12\}$ kHz. Within the uncertainty in the measurement of the beam waist, we can say that this prediction agrees with the observations. It is interesting to notice that since the light shifts are quadratic by nature, each spin state is shifted equal to $qm_F^2 + \beta m_F$ from the zero. Where q is the amplitude of the tensor light shift and β is the effective amplitude coming from the linear Zeeman shift plus the vector light shift. As a consequence, the Raman resonances between the neighboring spin states $|m_F\rangle \leftrightarrow |m_F \pm 1\rangle$ is shifted linearly $q(2m_F + 1) + \beta$.

Furthermore, we observe that the difference between the resonances $|-3/2\rangle \leftrightarrow |-5/2\rangle - |-7/2\rangle \leftrightarrow |-5/2\rangle, |-7/2\rangle \leftrightarrow |-5/2\rangle - |-7/2\rangle \leftrightarrow |-9/2\rangle$ is found to be $0.47 \pm 0.14, 0.44 \pm 0.14$ kHz. We can extrapolate this reasoning to obtain the resonances for the entire ground state manifold. Moreover, the resonances can be calibrated with the optical power of the laser. Figure 5 bottom right summarises the measured value of the resonances and extrapolated to the entire ground state manifold. In the section, I conclude that spin-dependent tensor light shifts are measured, and the

entire spectrum of resonances is obtained. We'll proceed to measure the scattering rate linked to the Moglabs laser.

2.2.3 Measurement of Scattering rate

As we will see later in this chapter, scattering associated with the spin-dependent light shift can be a limiting factor for coherent spin manipulation. Measuring the heating rate directly in the experiment helps us to characterize this scattering rate. In the experiment present in this sub-section, we directly measured the temperature raised in the Fermi gas by holding the Fermi gas in the beam responsible for inducing the light shifts on the atoms. The dipole trap depth is significantly larger than the energy acquired by the gas during the light pulse. Therefore, atoms do not leave the trap with all the energy acquired during the pulse maintained in the gas, and we can directly deduce the scattering rate from the heating rate.

For this, we prepare the Fermi gas with 10 spin states and re-compress the gas inside the dipole trap with a trap depth $U_{dip} \approx 65\mu K$. The trap depth $U_{dip} >> k_B T$ is sufficiently large as compared to the energy gained $k_B T$ by the atoms from the scattering processes. Hence, the atoms remain inside the trap during the scattering events. For this measurement, either *beam 1* or *beam 2* is pulsed with 6 mW power. The detuning of the beam to the excited state F=9/2 $^3P_1$ is kept $\Delta = -400$ MHz. After turning off the beam, the Fermi gas is released from the dipole trap. The temperature of the gas is measured after a time of flight. The pulse duration of the beam is varied to plot the curve shown in the figure 6. Black dots on the curve are the residual heating of the gas when there was no light pulsed and the time was varied. This residual heating comes from the acoustic vibrations of the dipole trap and needs to be considered for this study. The figure on the right shows the normalized heating rate to 1 mW of power in the beam. We observe the heating rate from the beam as $287 \pm 22 nK.s^{-1}.mW^{-1}$. The uncertainty in the measurement is fitting uncertainty from the covariance matrix only. Please note that this analysis does not take into account any experimental uncertainties. Furthermore, the beam waist at the location of the atom is $180 \pm 5\mu m$, this is because of the fact that this data was taken before the change of the beam waist as explained in the sub-section 2.5.2.

Let an atom absorbs a photon of momentum $\hbar \vec{k}_1$ from a coherent laser beam and then spontaneously emits a photon of momentum $\hbar \vec{k}_2$ in a random direction, then the change in momentum of the atom is given by $\delta \vec{p} = \hbar \vec{k}_2 - \hbar \vec{k}_1$. The square of the

change in momentum is $\delta\vec{p}^2 = (\hbar\vec{k}_2 - \hbar\vec{k}_1)^2 = \hbar^2(\vec{k}_2 - \vec{k}_1) \cdot (\vec{k}_2 - \vec{k}_1)$, which expands to $\delta\vec{p}^2 = \hbar^2(\vec{k}_2 \cdot \vec{k}_2 + \vec{k}_1 \cdot \vec{k}_1 - 2\vec{k}_1 \cdot \vec{k}_2)$. Taking the average of the square of the change in momentum, we have:

$$\langle \delta\vec{p}^2 \rangle = \hbar^2 \left(\langle \vec{k}_2 \cdot \vec{k}_2 \rangle + \langle \vec{k}_1 \cdot \vec{k}_1 \rangle - 2\langle \vec{k}_1 \cdot \vec{k}_2 \rangle \right) \tag{2.2.2}$$

Since the emitted photon is in a random direction and is independent of the absorbed photon, $\langle \vec{k}_1 \cdot \vec{k}_2 \rangle = 0$, and the magnitudes are $\langle \vec{k}_1^2 \rangle = \langle \vec{k}_2^2 \rangle = k_R^2$, where k_R is the recoil wave vector. Thus, $\langle \delta\vec{p}^2 \rangle = \hbar^2(k_R^2 + k_R^2) = 2(\hbar k_R)^2$. Furthermore, the change in the total energy of the gas due to this process is given by:

$$\frac{dE_{total}}{dt} = \gamma_{sc} \frac{\langle \delta p^2 \rangle}{2m} = 2\gamma_{sc} E_R \tag{2.2.3}$$

Where $E_R = \hbar^2 k_R^2 / 2m$ is the recoil energy of the 689 nm photon absorbed or emitted by the atom. A thermalized gas in 3 dimensions at a temperature T has the total energy $E_{total} = 3k_B T$, where k_B is the Boltzmann constant. Then, the scattering rate γ_{sc} is given by:

$$\gamma_{sc} = \frac{3}{2} \frac{k_B}{E_R} \frac{dT}{dt} \tag{2.2.4}$$

This scattering rate can be calculated by directly measuring the temperature increment as a function of time. From Figure 6, the scattering rate is calculated as $1.8 \pm 0.07 s^{-1}$ per mW of optical power in the beam. The theoretical calculations from the equation 2.1.2 give the scattering rate $< \gamma_{sc} >_{mF} = 0.54 s^{-1}$ per mW when averaged over all the spin states m_F. The theoretical prediction is approximately three times less than the experimental observations.

To interpret this abnormal heating rate, we have questioned the spectral purity of the Moglabs laser. The spectral impurities of the diode laser can lead to amplified spontaneous emission, which in turn causes excessive scattering. One way to solve this issue is to filter the laser output by a Fabry-Perot cavity. I tested a Fabry-Perot cavity in the optical path of *beam 1*. Measurement with the cavity showed a reduction in heating rate to $65 \pm 4 nK.s^{-1}$ per mW as shown in the figure right of 6. This heating rate corresponds to a scattering rate $0.43 \pm 0.06 s^{-1} mW^{-1}$, which agrees with the theoretical prediction. The measurement showed that the cavity improved the spectral quality of the diode laser, which resulted in the desired expectation of scattering
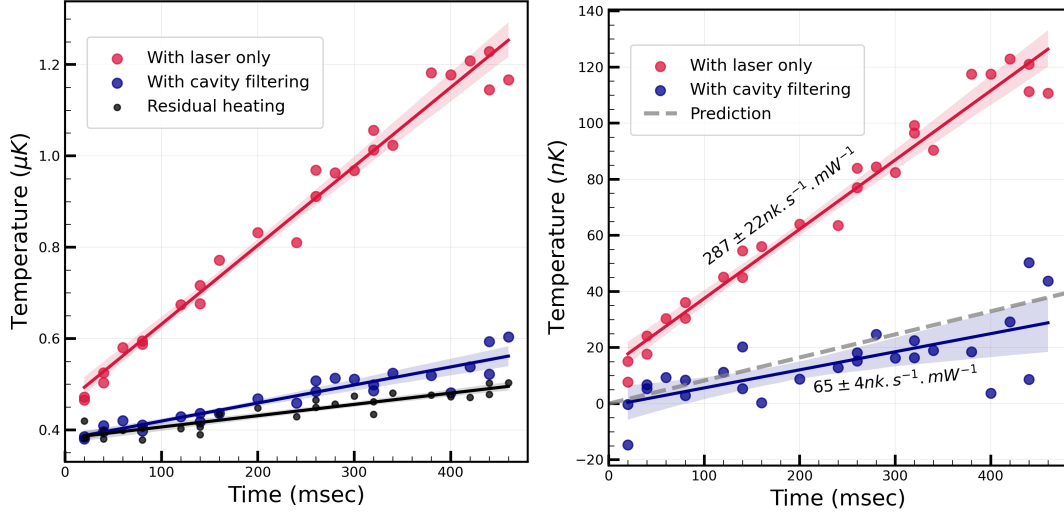
Figure 6: The figure shows the measurement of the heating rate from the beam used for spin-dependent light shits. The detuning to the excited state F = 9/2 $^3P_1$ is kept $\Delta = -400$ MHz for his measurement. Red dots show the heating rate directly from the beam. Blue dots show heating from the light filtered by the cavity. Black dots are residual heating. Left: Direct measurement of heating rate with 6 mW power in the beam while 2.5 mW power after the cavity filtering. Right: Normalized heating rate to 1 mW power in each case. The dashed grey line is a theoretical estimation of the heating rate according to the equation 2.1.2 at 1mW of beam power with 180 µm beam waist.

rate. However, improvements in vibrational instabilities are necessary to ensure the cavity's robustness for daily experiment operation. The construction of the cavity with improved vibrational stability and a robust lock is in progress. Therefore, we will not use this cavity during the period of this thesis.

We now have an in-depth understanding of the spin-dependent light shifts and their associated scattering rate. The ground state manifold is ready for spin modification. To do this, we will proceed to the following part.

2.3 CONTROLLED MANIPULATION OF NUCLEAR SPIN STATES

In this section, I will present a scheme for adiabatic passages between the spin-states $|m_F\rangle \leftrightarrow |m_F \pm 1\rangle$. Once we have resolved the ground state manifold $^1S_0$ quadratically in section 2.2.2, it is possible to select the two spin states and coherently manipulate them within the ground state manifold with low spontaneous emission. I will apply

this scheme experimentally to spin states $|-5/2\rangle \leftrightarrow |-7/2\rangle$. We obtained an approximate 80% on-way adiabatic passage efficiency, which is constrained by spontaneous emission. This one-way scheme is generalizable to the ten spin states in the ground state manifold $^1S_0$.

2.3.1 Outline of the scheme

As described in the Figure 4, our experimental setup consists of two beams. *beam 1* which is π polarized and *beam 2* which is circularly $\sigma^+ + \sigma^-$ polarized. We engineer our scheme through the process of two-photon adiabatic Raman passage. We can think of this process as one photon absorbed in *beam 1* and second photons emitted in *beam 2* or vice-versa. Thus, it is possible to couple the two spin states which differ by $|m_F\rangle \leftrightarrow |m_F + 1\rangle$. Two photon Raman process can come from $\pi + \sigma^+$ photons or $\pi + \sigma^-$. Since the light shift is quadratic, it is possible to cross a resonance through only one set of polarization at a time for a given detuning of $\omega_1 - \omega_2$ of the two beams. We have optimized our optical pumping sequence to prepare the Fermi gas in the negative spin states. For the negative spin states, Clebsch-Gordan coefficients for the σ^- transition are stronger than σ^+ transition, so it is desirable to take advantage of $\pi + \sigma^-$ transition. In this particular case, the Raman resonances are crossed for $\delta > 0$ for negative spin states and $\delta < 0$ for positive spin states, as shown in Figure 7.

2.3.2 Spectrum of Hamiltonian with two beams

Before moving on to the experimental results, I will discuss the Hamiltonian associated with two-photon couplings. I will highlight the dynamics of the eigenenergies of this Hamiltonian as a function of detuning δ. I will start by considering a case where each spin state in the ground state manifold of the ^{87}Sr is coupled through two beams that have the electric field amplitude (E_π, E_{σ^-}) with (π, σ^-) polarizations respectively. For a general point of view, recall the equation 2.1.3 that estimates couplings of the spin states $|m_F\rangle$ and $|m_F + q_1 - q_2\rangle$ with the arbitrary polarizations q_1 and q_2.

We can define the basis in the dressed picture such that the quadratic light shift is included in a time-independent part of the Hamiltonian. I will define each state basis as $|m_F + n\rangle \equiv |m_F + n, N_\pi - n, N_\sigma + n\rangle$, where (N_π, N_σ) are the number of photons in the *(beam 1, beam 2)* respectively and n is an integer. Furthermore, each spin state $|m_F\rangle$ is connected to $|m_F \pm 1\rangle$ spin states by the $\pi + \sigma^-$ two-photon Raman couplings, with the detuning is defined as $\delta(t) = \omega_1(t) - \omega_2(t)$. Each dressed state $|m_F + n\rangle$ has
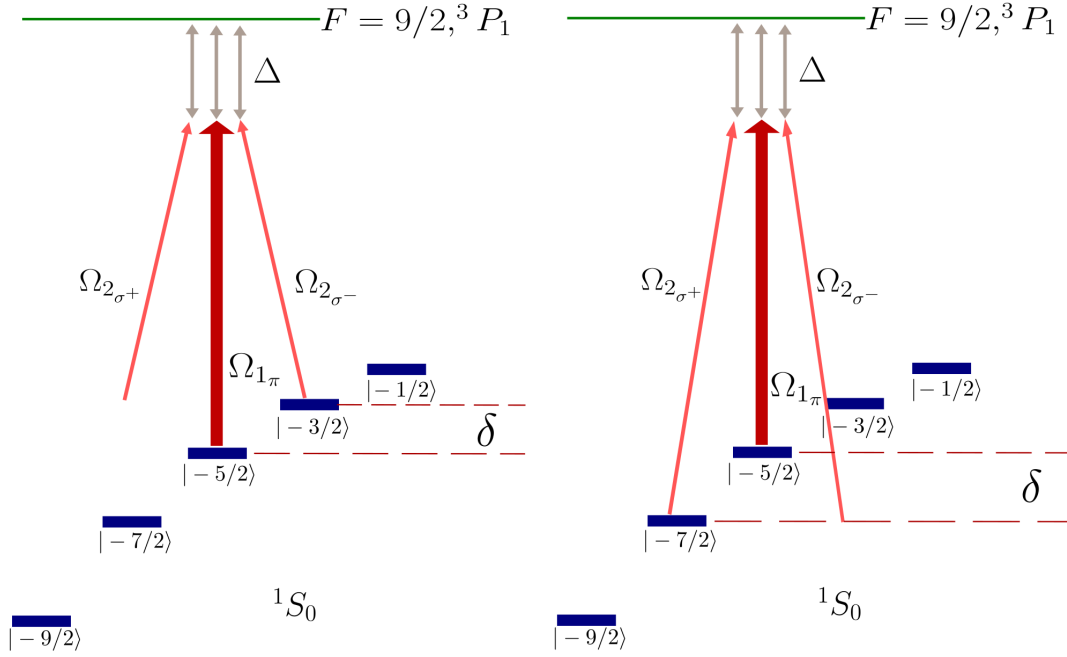
Figure 7: Above is an illustration explaining the scheme for selective two-photon couplings. For simplicity, only the negative spin states in the ground manifold are displayed. Detuning between the two beams defined as $\delta = \omega_1 - \omega_2$. (Ω_1, Ω_2) are the Rabi couplings from the *beam 1* and *beam 2* respectively. Left: The transition is resonance through $\pi + \sigma^-$ couplings. Right: The transition is resonance through $\pi + \sigma^+$ couplings. The direction of the arrows does not show any physical process. The figure is not to scale.

energy $n\delta(t)$, a time-dependent diagonal part of the Hamiltonian. The off-diagonal Rabi couplings under this Hamiltonian calculated from the second-order perturbation theory as,

$$\frac{\hbar \Omega_{m_{F1}}^{m_{F2}}}{2} = |E_\pi| \, |E_{\sigma_-}| \sum_{|m_{F'}\rangle} \frac{\langle m_{F2} \, |\epsilon_\pi^* \cdot \hat{d}| \, m_{F'} \rangle \langle m_{F'} \, |\epsilon_{\sigma_-} \cdot \hat{d}| \, m_{F1} \rangle}{\Delta_{m_{F'}}} \tag{2.3.1}$$

Where $|m_{F'}\rangle$ are all the excited states in the $^3P_1$ manifold. Typically $\omega_1 - \omega_2$ is of the order of kHz while the detuning to the excited state is of the order of 100's of MHz. Hence $\Delta_{m_{F'}}$ can be approximated as $\Delta_{m_{F'}} = \omega_e - \omega_1 \sim \omega_e - \omega_2$. The dipole matrix element part $\mu_{m_F, m_{F'}} = \langle m_{F'} \, |\epsilon_{\sigma_-} \cdot \hat{d}| \, m_F \rangle$ can be calculated from the Wigner-Eckart theorem and depends only on the properties of the atom. We can calculate the Rabi couplings for all ten spin states using the equation 2.3.1. The ten spin states effective

Hamiltonian with all the Rabi couplings and quadratic light shifts have a tridiagonal form, which is written as,

$$\hat{H}(\delta(t)) = \hat{H}_{ls} + \frac{\hbar}{2} \begin{pmatrix} -9\delta(t) & \Omega_{-9/2}^{-7/2} & 0 & \cdots & 0 & 0 & 0 \\ \Omega_{-9/2}^{-7/2*} & -7\delta(t) & \Omega_{-7/2}^{-5/2} & \cdots & 0 & 0 & 0 \\ 0 & \Omega_{-7/2}^{-5/2*} & -5\delta(t) & \ddots & 0 & 0 & 0 \\ \vdots & \vdots & \ddots & \ddots & \ddots & \vdots & \vdots \\ 0 & 0 & 0 & \ddots & 5\delta(t) & \Omega_{5/2}^{7/2} & 0 \\ 0 & 0 & 0 & \cdots & \Omega_{5/2}^{7/2*} & 7\delta(t) & \Omega_{7/2}^{9/2} \\ 0 & 0 & 0 & \cdots & 0 & \Omega_{7/2}^{9/2*} & 9\delta(t) \end{pmatrix}$$

$$(2.3.2)$$

This effective Hamiltonian consists of two parts, the first part $\hat{H}_{ls}$ that is time-independent gives the quadratic light shift the same as calculated in the sub-section 2.1.1, and the second part is time-dependent and is zero in the absence of *beam 2* with σ^- polarization. For the coupling of the spin states $|m_F\rangle \leftrightarrow |m_F \pm 1\rangle$ via two coherent fields with the polarization π and σ^-, this Hamiltonian describes the two-photon Raman processes. The eigenenergies spectrum of this Hamiltonian is made by diagonalizing this Hamiltonian. The spectrum consists of avoided energy crossing between the spin states. These avoid crossings are the signature for the possibility of manipulating the spin states. Figure 8 shows the eigenenergy spectrum of this Hamiltonian based on the experimental parameters.

In Figure 8, we observe avoided crossings between the eigenenergies of spin states $|m_F\rangle \leftrightarrow |m_F + 1\rangle$, which shows the possibilities of two-photon transitions. To perform two-photon transitions adiabatically, we use these avoided crossings [Zener and Fowler, 1932]. Effective Rabi coupling, which is the size of the avoided gap in figure 8, determines the strength of the transition. The effective two-photon Rabi coupling associated with these crossings is given by:

$$\Omega_{m_F, m_F+1}^{2\nu} \propto \sqrt{I_1 I_2} \qquad (2.3.3)$$
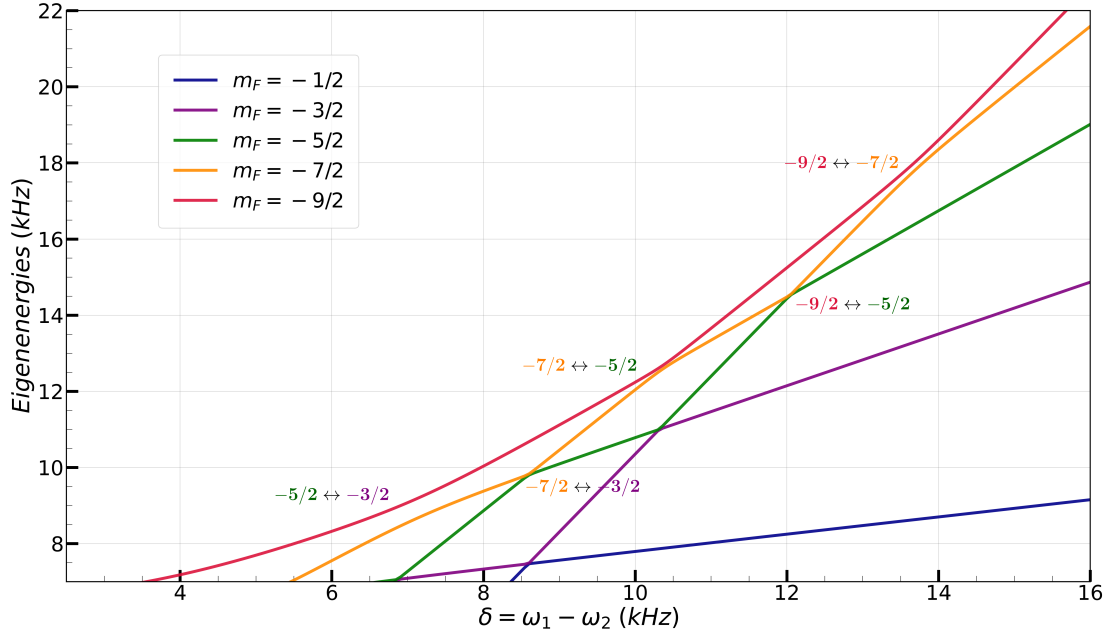
Figure 8: The figure shows the spectrum of the eigenenergies of the Hamiltonian concerning the detuning δ between the two beams. Here, the respective power in *beam 1* and *beam 2* is 5mW and 2.5 μW respectively with the beam waist of 180 ±5 μm. Detuning for both the beams is kept at $\Delta = -700$ MHz from the excited state $F = 9/2, ^3P_1$. For better visibility of the lines, only the negative spin states are plotted with their respective color code.

The two-photon Rabi coupling $\Omega^{2\nu}_{mF,mF+1}$ scales as the square root of the intensities of the two beams *beam 1* and *beam 2*. Since the tensor light shift is proportional to the intensity I_1 in the *beam 1*. The ratio of the two-photon Rabi coupling and the tensor light shift ΔE is:

$$\frac{\Omega^{2\nu}_{mF,mF+1}}{\Delta E} \propto \sqrt{\frac{I_2}{I_1}} \tag{2.3.4}$$

Additionally, in order to isolate the two-level system, the effective Rabi coupling must be less than the tensor light shift. This leads us to the following requirement:

$$\Omega^{2\nu}_{mF,mF+1} << \Delta E \quad \rightarrow \quad I_2 << I_1 \tag{2.3.5}$$

Furthermore, we also observe the crossings between the spin states $|m_F\rangle \leftrightarrow |m_F + 2\rangle$ involving four-photon transitions (may not be visible in the figure due to smaller strength as compared to avoided crossing associated with the two-photon transitions).

This four-photon process decreases the spin selectivity depending on how strong the effective four-photon Rabi coupling $\Omega^{4\nu}_{mF,mF+2}$ are associated with them. It is necessary to minimize these higher-order processes to maintain the selectivity of spin states. The effective Rabi couplings involving four-photon transitions are expressed in terms of the two-photon Rabi couplings:

$$\Omega^{4\nu}_{mF,mF+2} = \frac{\Omega^{2\nu}_{mF,mF+1} \cdot \Omega^{2\nu}_{mF+1,mF+2}}{2\Delta} \propto \frac{I_1 I_2}{I_1} \propto I_2 \qquad (2.3.6)$$

Where Δ is the difference between two-photon and four-photon resonances. In our experiment where $I_1 >> I_2$, These resonances depend only upon the quadratic light shift induced by the *beam 1*. Hence, the difference between them Δ scales as $\Delta \propto I_1$. Since the two photon Rabi couplings are proportional to $\sqrt{I_1 I_2}$ and four photon Rabi couplings scales as $\Omega^{4\nu}_{mF,mF+2} \propto I_2$. The ratio between the two is given by:

$$\frac{\Omega^{4\nu}_{mF,mF+2}}{\Omega^{2\nu}_{mF,mF+1}} = \sqrt{\frac{I_2}{I_1}} \qquad (2.3.7)$$

We can immediately notice the relative strength of the two Rabi coupling scales as the square root of the ratio of the intensities in the two beams. The lower the intensity in the *beam 2* compared to the intensity in *beam1*, the lower the four-photon Rabi coupling. However, to preserve the coherence of the two-photon Raman process, we cannot arbitrarily reduce the intensity of the *beam 2*. In Figure 8, I show the eigenenergies spectrum with the relative strength of the intensities of the two beams as $I_1/I_2 = 500$. The relative intensity is sufficient for the two-photon Rabi coupling to be large enough to realize the adiabatic passages while keeping the four-photon Rabi coupling low. The relative coupling strength between the two is $\Omega^{4\nu}_{mF,mF+2}/\Omega^{2\nu}_{mF,mF+1} = 5\%$. Hence, For the manipulation of the spins throughout this thesis, we will adapt the case where $I_2 << I_1$. Concluding our conversation for this subsection. Next, I'll discuss the scheme's experimental outcomes.

2.3.3 Raman adiabatic passages

Based on the discussion in the previous sub-section, it is now possible to drive adiabatic passages between desirable spin states by chirping the detuning δ between the two beams through a particular Raman resonance. It is desirable to have more power in the *beam 1* to have well-resolved Raman resonances compared to the effective Rabi

coupling between the initial and the target state. In contrast, decreasing the intensity of the *beam 2* sufficiently low decreases the probability of four-photon transition $|m_F\rangle \leftrightarrow |m_{F\pm2}\rangle$ drastically. However, lowering the intensity in *beam 2* also decreases the effective two-photon Rabi couplings that require a slower chirp rate. In addition, we need to be careful that this chirp rate remains sufficiently fast compared to the typical decoherence time of the system. The Landau-Zener probability of success for an adiabatic following is defined as []:

$$P_{LZ}(\Omega_{eff}, \dot{\delta}) = 1 - \exp\left(-2\pi\frac{\Omega_{eff}^2}{4\dot{\delta}}\right) \tag{2.3.8}$$

Where Ω_{eff} is the effective Rabi coupling, it can be either two-photon or four-photon. The $\dot{\delta}$ is the chirp rate. The probability approaches one under the condition $\dot{\delta} << \Omega_{eff}$. The robustness to transfer the population only through a desired resonance is provided by maintaining the correct adiabatic conditions such as initial frequency, final frequency, and the chirping rate associated with a particular resonance. If the chirp parameter is chosen carefully such that:

$$\Omega_{mF,mF+2}^{4\nu} << \dot{\delta} << \Omega_{mF,mF+1}^{2\nu} \tag{2.3.9}$$

We can be diabatic to a four-photon transition but adiabatic to a two-photon transition. Thus, it is possible to engineer two-photon adiabatic passages through a particular resonance even though we may cross some four-photon transitions while chirping the frequency of the beam. Additionally, we can adapt the chirp rate such that the ratio of four-photon coupling to two-photon coupling is minimal.

A spin-polarized Fermi gas is prepared in the spin state $|-7/2\rangle$ in order to realize adiabatic passages. As described in sub-section 2.2.2, the magnetic field is slowly aligned collinearly with the π polarization of the *beam 1*. Then the *beam 1* is turned on to maximum intensity $I_1 = 9.3W/cm^2$ in 2 ms. The frequency of the *beam 1* is kept at $\Delta = -700MHz$ from the $F = 9/2,^3 P_1$ hyperfine state. *Beam 1* lifts the degeneracy of the ground state manifold. To conduct this experiment, please note that the intensity of *beam 1* is not locked because the chirp time (10 ms) of the experiment is sufficiently short compared to the slow drifts of the intensity in the *beam 1*. Since the frequency of *beam 2* is chirped through the resonance, the adiabatic passage is robust enough to have a high probability of transfer even with slow intensity fluctuations in *beam 1*.
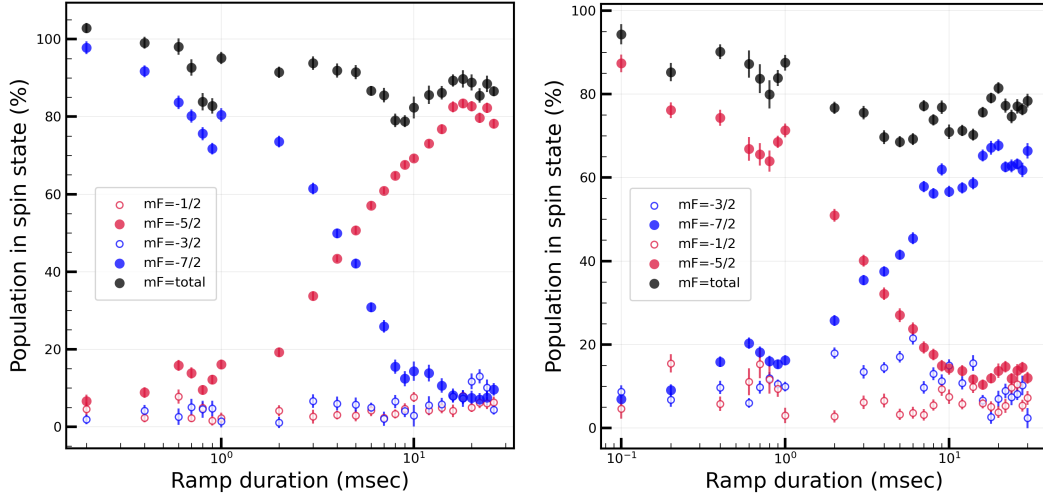
Figure 9: Figure shows the experimental results for the adiabatic sweeps. The detuning to the F= 9/2 $^3P_1$ excited state is $\Delta = -700$ MHz for both the beams. The intensity in the *beam 1* and *beam 2* is 9.3 W/cm^2 and 5.1 mW/cm^2 respectively. The measured population with associated error bars in each spin state scaled with the measurement efficiency of each spin state. The sum of the population in spin states $|-7/2\rangle$ and $|-5/2\rangle$ is represented by the black-filled circular points. Left: forward adiabatic passage from spin state $|-7/2\rangle$ to $|-5/2\rangle$ with detuning $\delta = \omega_1 - \omega_2$ ramp between the two beams from 5 kHz to 13 kHz. Right: Similarly, a backward adiabatic passage from spin state $|-5/2\rangle$ to $|-7/2\rangle$ with a detuning ramp 13 kHz to 5 kHz.

After the previous steps, *beam 2* turned on adiabatically to 5.1mW/cm^2 in 2.5 ms. The frequency of the *beam 2* ramped in such a way that detuning $\delta = \omega_1 - \omega_2$ is chirped from 5kHz to 13kHz for different time durations. In the end, both beams are turned off in the same manner they were turned on. The population of atoms in each spin state is measured by the spin-dependent momentum transfer protocol [Bataille et al., 2020]. Figure 9 shows the measurement of the spin populations with respective error bars as they evolved during the experiment. The figure is re-scaled for the 78 % efficiency of the population measurement. The figure shows the total number of atoms (∼ 15000) measured for each data point, represented by black dots. We observed that the number is not constant throughout the experiment.

At the beginning of the experiment, approximately 90 % of atoms are in the spin state $|-7/2\rangle$, while 10 % of atoms are in the spin state $|-5/2\rangle$. As the chirp time of the detuning becomes larger, the spin state $|-5/2\rangle$ starts to populate and reaches a plateau where approximately 80% atoms are transferred to the target spin state $|-5/2\rangle$. It is important to notice for further slow chirp rate, spin state $|-3/2\rangle$ starts to populate. At the optimum chirp rate around 20 ms 80 % atoms are transferred to $|-5/2\rangle$ and 10 % to

$|-3/2\rangle$ and the remaining are still in spin state $|-7/2\rangle$. The overall process efficiency is evaluated, with the passage repeated in reverse chirp direction, from 13kHz to 5kHz.The result shows a similar output as the forward passage. Around 20 ms of the chirp time we observe 60 % atoms in $|-7/2\rangle$ and 10 % atoms in $|-3/2\rangle$ and $|-5/2\rangle$ each. With the forth and back passage 65 % atoms have been recovered to initial state $|-7/2\rangle$. One-way adiabatic passage efficiency is 80 %. Even after crossing the multiple four-photon transition, it was possible to realize adiabatic passage between the spin states $|m_F\rangle \leftrightarrow |m_{F\pm1}\rangle$. The robustness of adiabatic passage allows us to manipulate spin states selectively with the help of the proper direction of frequency chirp and the choice of initial and target spin state.

2.4 SPIN TEXTURE WITH SITE SELECTIVE ADIABATIC PASSAGES

The spin-dependent light modulated spatially can have spatial selectivity on atoms. One way to do this is simply retroreflecting the light to form an optical lattice, where the number of dimensions we retroreflect the light gives the control over the number of dimensions in which we can spatially select the spin dependence. Patterns of atoms based on site-selective light shifts have been demonstrated [Griffin et al., 2006; Kolkowitz et al., 2016]. These experiments prepare a quantum state for many body physics [Mandel et al., 2003]. Furthermore, writing the spin textures with spatially resolved spin-dependent light shifts opens intriguing possibilities for studying various quantum phases such as antiferromagnetism [H. Sun et al., 2021].

689 nm 1D lattice

532 nm 2D lattice

$|m_F \pm 1\rangle$
$|m_F\rangle$
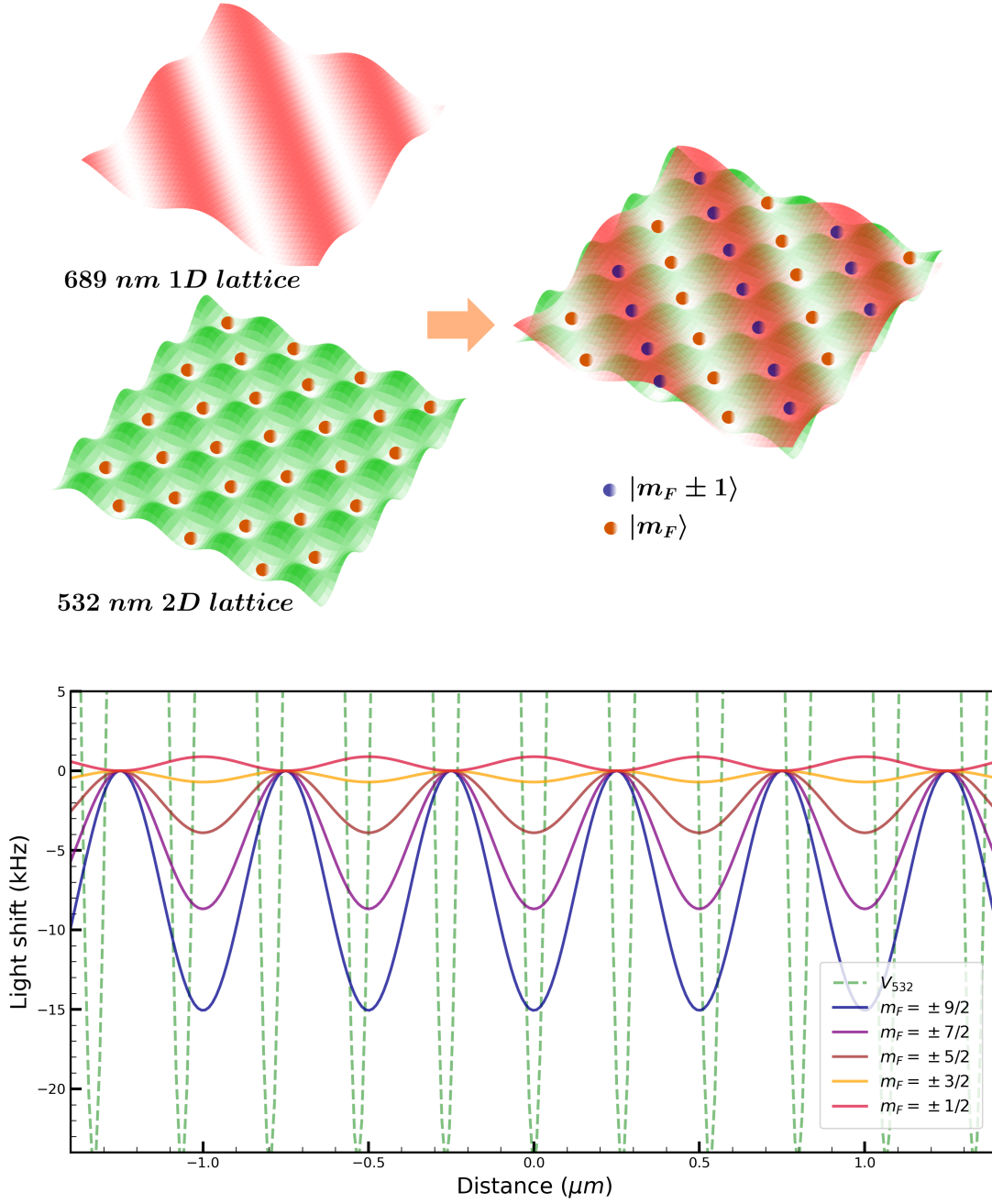
Figure 10: Illustration for spacial and spin-dependent tensor light shifts. Up: Spacial geometry of 532 nm 2D lattice combined with 689 nm 1D lattice along the diagonal of 532 nm lattice. Here, lattice spacing for the 689nm lattice kept $a_{689} = \sqrt{2}a_{532}$. Experimentally projection of the 689 nm lattice along the plane of the 532 nm lattice is with $a_{689} \approx 360$nm, which is 10% less than the lattice spacing along the diagonal of the 532 nm lattice. Down: Considering the 10% mismatch in the two lattice spacing spin-dependent light shift felt by each spin state along the diagonal of the 532 nm lattice. The Green dashed line represents the trapping potential from the 532 nm lattice, while the solid line represents the light shift felt by each spin state.

In this section, I aim to outline our scheme for realizing Raman adiabatic passages that are spatially dependent. Even though *beam 2* stays homogenous, adiabatic passageways can be engineered at the region of highest intensity alone because light shifts (Raman resonances) inside the optical lattice are proportional to the local intensity of *beam 1*. Therefore, our scheme to coherently flip the nuclear spin states enables the possibility of handwriting a predictable spin texture.

2.4.1 Scheme overview

To understand the scheme, I will first highlight some of the features of our 3D optical lattice. Several layers of quasi-2D lattices in the vertical direction along the gravity are formed by the combination of 532 nm and 1064 nm lattices. 1D lattice with several planes along the direction of gravity is formed by 1064 nm light. In each plane, a 2D lattice is formed by the 532 nm light. The *beam 1* and *beam 2* introduced earlier have the azimuthal angle of 45° with two 532 nm lattice beams, such that *beam 1* and *beam 2* are along the diagonal of the 2D lattice formed by the 532 nm light. *Beam 1* and *beam 2* has an altitude angle of 16° from the plane of the 2D lattice.

Furthermore, *Beam 1* is retroreflected to form a 1D 689 nm lattice along the plane of the 2D lattice with the effective lattice spacing $a_{689} \sim 360$ nm in this plane. The lattice spacing of the 2D lattice along the diagonal is approximately $\sqrt{2}a_{532} \sim 390$ nm. Both have a 10% differential lattice spacing. Since the Raman resonances are proportional to the local intensity of the 689 nm lattice, it is possible to realize the adiabatic Raman passages at the sites where the intensity of the *Beam 1* is above a threshold intensity, and with a homogeneous *Beam 2*. We need to consider the 10% difference in the two lattice sites, but the robustness of the adiabatic conditions will allow us to write spin textures with even this discrepancy.

Figure 10 up shows the combination of 532 nm and 689 nm lattice. Due to the periodicity of the 1D 689 nm lattice, only the atoms at the sites where the intensity is close to maximum experience the Raman adiabatic passages between the spin states $|m_F\rangle \leftrightarrow |m_F \pm 1\rangle$. Figure 10 up shows the intensity profile of the 689 nm lattice considering the 532 nm lattice. We see that the intensity of the 689 nm lattice is not always maximum at the location where the intensity of the 532 nm lattice is maximum. In fact, on every 11th lattice site, the intensity profile of the 689 nm lattice felt by the atoms frozen in the 532 nm lattice repeats.

We aim to realize the adiabatic passages at the site where the intensity is close to maximum. Thanks to the adiabatic criteria 2.3.8, by choosing an appropriate frequency

window with a time that is slow enough for the 532nm lattice site where the intensity of *beam 1* is above the threshold for Landau-Zener criteria to fulfill. This means only the atoms in every other site go through an adiabatic passage.

2.5 SPIN SELECTIVE COHERENT RABI OSCILLATIONS

Once we have isolated a system of two levels from the ground state manifold of several spin states, it is possible to drive coherent Rabi oscillations between the two isolated spin states. This also provides an opportunity to carry out a series of two-level unitary rotations within the ground state manifold with the condition:

$$
\frac{\Omega^{2\nu}_{mF,mF\pm1}}{TLS} = \frac{I_2}{I_1} << 1 \tag{2.5.1}
$$

Where $\Omega^{2\nu}_{mF,mF\pm1}$ is the two photon Rabi coupling and TSL is the tensor light shift. In this section, I will present the schemes by which we can couple the two isolated spin states and perform Rabi rotations between them. I'll start with the scheme for the two isolated spin states that differ by $\Delta mF = 1$. Then, I will discuss the coherence of the Rabi oscillations amongst these spin states. Finally, I will summarise the scheme where the Rabi oscillations are performed between the two spin states that differ by $\Delta mF = 2$.

2.5.1 $\pi - \sigma$ configuration
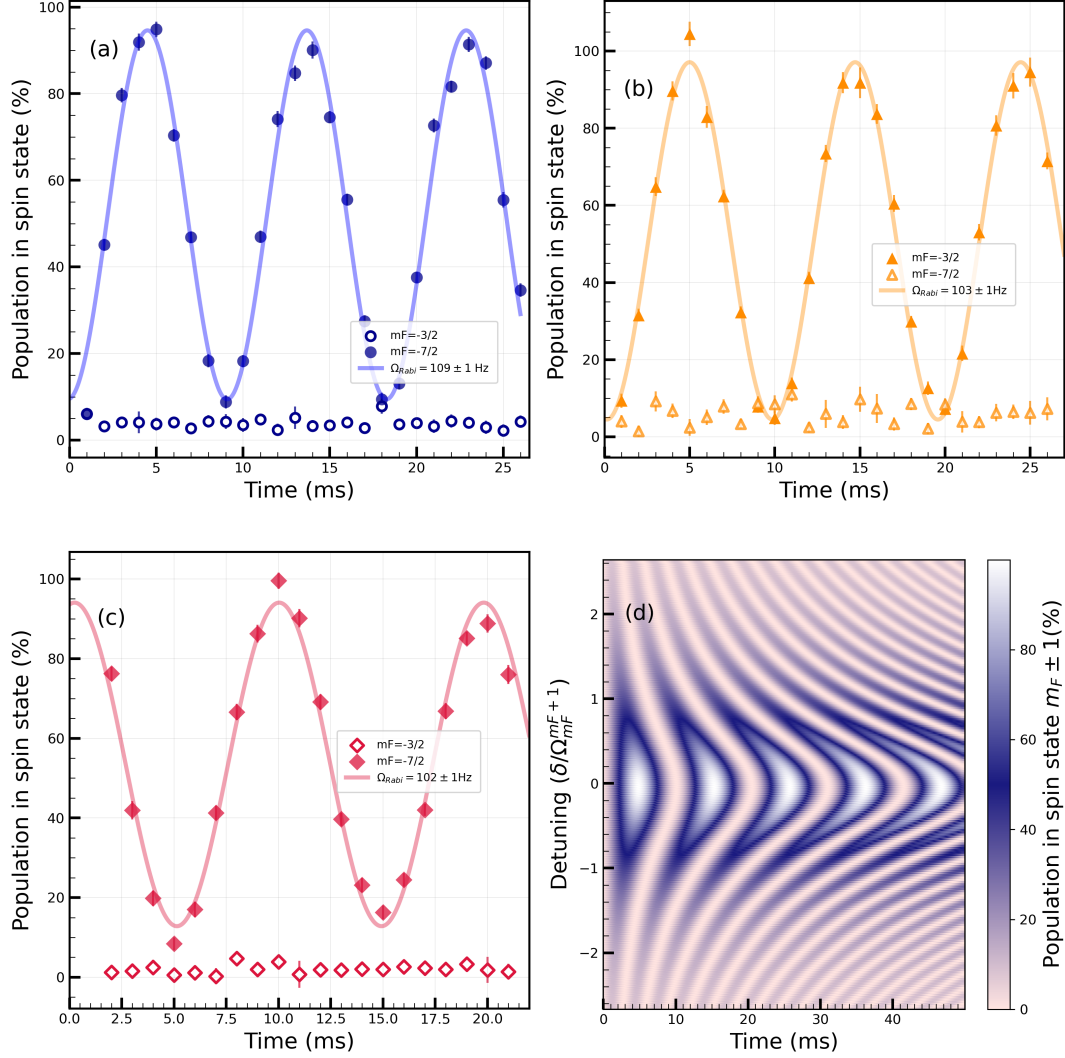
Figure 11: The figure shows the experimental observation of Rabi oscillations between the spin states $|m_F\rangle \leftrightarrow |m_{F\pm1}\rangle$. The power in *beam 1* is 4.5 mW while the power in *beam 2* is 0.8 μW respectively. Both beams have a waist of $325 \pm 5\mu m$ at the location of atoms. Both the beams have a detuning of -600 MHz from the excited hyperfine state $F = 9/2, ^3P_1$. The intensity of *beam 1* was locked during the experiment. {(a), (b), (c)} shows the Rabi oscillations between the spin states $|-5/2\rangle \leftrightarrow |-7/2\rangle$, $|-5/2\rangle \leftrightarrow |-3/2\rangle$ and $|-7/2\rangle \leftrightarrow |-9/2\rangle$ respectively. Measured spin states are {$|-7/2\rangle, |-3/2\rangle, |-7/2\rangle$} respectively. (d) shows the theoretical prediction of the Rabi oscillation map where the y-axis is detuning in terms of $\Omega_{m_F}^{m_F\pm1}$ with typical experimental parameters. The population in the target spin state has been plotted in the map.

As shown in section 2.2.2, each resonance is measured with the help of the Raman resonance spectroscopic scheme. We know the frequency of *beam 2* (or the detuning between the two beams) at which each resonance occurs after fitting equation 2.2.1 on the experimental data. We can select a particular resonance to drive Rabi oscillations. Then, the detuning between the two beams is set to match the chosen resonance. The time of the square pulse of the *beam 2* scanned to observe the Rabi oscillations between two resonant spin states $|m_F\rangle \leftrightarrow |m_F+1\rangle$. Since the coupling between the two resonant spin states is from $\pi + \sigma^-$ photon, I call this scheme $\pi + \sigma^-$ configuration. Note that the intensity of the *beam 1* is locked during this experiment. The experimental data in figure 11 shows the Rabi oscillaitons between the states $|-3/2\rangle \leftrightarrow |-5/2\rangle$, $|-5/2\rangle \leftrightarrow |-7/2\rangle$ and $|-7/2\rangle \leftrightarrow |-9/2\rangle$. Population in the initial or the target state is measured. It is difficult to measure the population in spin state $m_F = |-9/2\rangle$ for the resonance between $|-7/2\rangle \leftrightarrow |-9/2\rangle$ because of the weak coupling of this spin state to the excited state because of the weaker Clebsch–Gordan coefficient compared to the other spin states. For the resonance $|-7/2\rangle \leftrightarrow |-9/2\rangle$ population in the initial state $|-7/2\rangle$ is measured.

As I will show in the sub-section 2.5.2, the coherence time of observed Rabi oscillations is sufficiently long 295ms compared to a typical π pulse. Hence, we can extract the effective Rabi couplings directly fitting the data with the equation:

$$P(t)_{m_F \to m_F \pm 1} = \text{Sin}^2 \left(\frac{\Omega_{eff}}{2} t + \phi \right) \tag{2.5.2}$$

Where, $P(t)_{m_f \to m_F+1}$ is the measured population in the target spin state $|m_{F\pm1}\rangle$. Ω_{eff} is the effective Rabi couplings between the resonant spin states $|m_F\rangle \leftrightarrow |m_F \pm 1\rangle$. This expression relies on the fact that the resonances are well known from the sub-section 2.2.2. Therefore, the detuning δ is assumed to be zero for a particular resonance while fitting. Please note that only in Figure 11 (c), the population in the initital spin state is measured. Therefore, fitted is done with the equation $1 - P(t)_{m_F \to m_{F+1}}$. The effective fitted Rabi couplings for the spin states $\{\Omega_{-5/2}^{-7/2}, \Omega_{-3/2}^{-5/2}, \Omega_{-7/2}^{-9/2}\}$ are found to be approximately $\{109, 103, 102\}$Hz. Figure (d) shows the theoretical simulation with similar experimental parameters that shows the similar expected time scale for the Rabi oscillations between the spin states $|-5/2\rangle \leftrightarrow |-7/2\rangle$.

In Figure (a), the Rabi oscillations are between the spin states $|-5/2\rangle \leftrightarrow |-7/2\rangle$. For this data, our spin-dependent momentum transfer technique [Bataille et al., 2020] allowed us to measure the population between the spin states $|-3/2\rangle \leftrightarrow |-7/2\rangle$, which confirms the fact that no atoms are being transferred to the neighboring spin

state $|-3/2\rangle$. Similarly, in Figure (b), The Rabi oscillations are between the spin states $|-5/2\rangle \leftrightarrow |-3/2\rangle$. While we also measure the population in the spin state $|-7/2\rangle$ confirming that there are not atoms in this spin state. The ratio of the power $P_1/P_2 = 1/5500$ between the *beam 1* and *beam 2* is chosen in such a way that the two resonances are well separated. Overall, the effective Rabi frequency needs to be greater than the spontaneous emission rate, as well as greater than the fluctuations in tensor light shift. In addition, as we will see in the next sub-section inhomogeneity in tensor light shift also plays a crucial role. Here, we confirm that we can selectively drive the coherent Rabi oscillations in the ground state manifold $^1S_0$ under the scheme for being resonant with the spin state $|m_F\rangle \leftrightarrow |m_F \pm 1\rangle$.

2.5.2 Coherence of Rabi oscillations

In this sub-section, I will determine the coherence time of the Rabi oscillations observed in section 2.5.1. As I will demonstrate in the following chapter, the coherence between two spin states is crucial in various interferometric schemes. Moreover, I will compare two situations. In the first case, the beam waist is $180 \pm 5\mu m$, and in the latter case, I increased the beam waist to $320 \pm 5\mu m$. As a result, the quality and coherence time of the Rabi oscillations have improved in the latter scenario. Measuring the coherence time of Rabi oscillations for spin states $|mF\rangle \leftrightarrow |mF \pm 1\rangle$ is a straightforward task. For this, I scanned the time of the square pulse of *beam 2* long enough until I saw the contrast of the Rabi oscillations decaying. Figure 12 shows the experimental data fitted with the equation 2.5.3. Where P_{m_F} is the population in the state m_F, Ω is the Rabi frequency, and by definition t_0 is the coherence time of the oscillations.

$$P(t)_{m_F} = a_0 + a \sin(\Omega t + \phi) \exp(-t/t_0) \qquad (2.5.3)$$
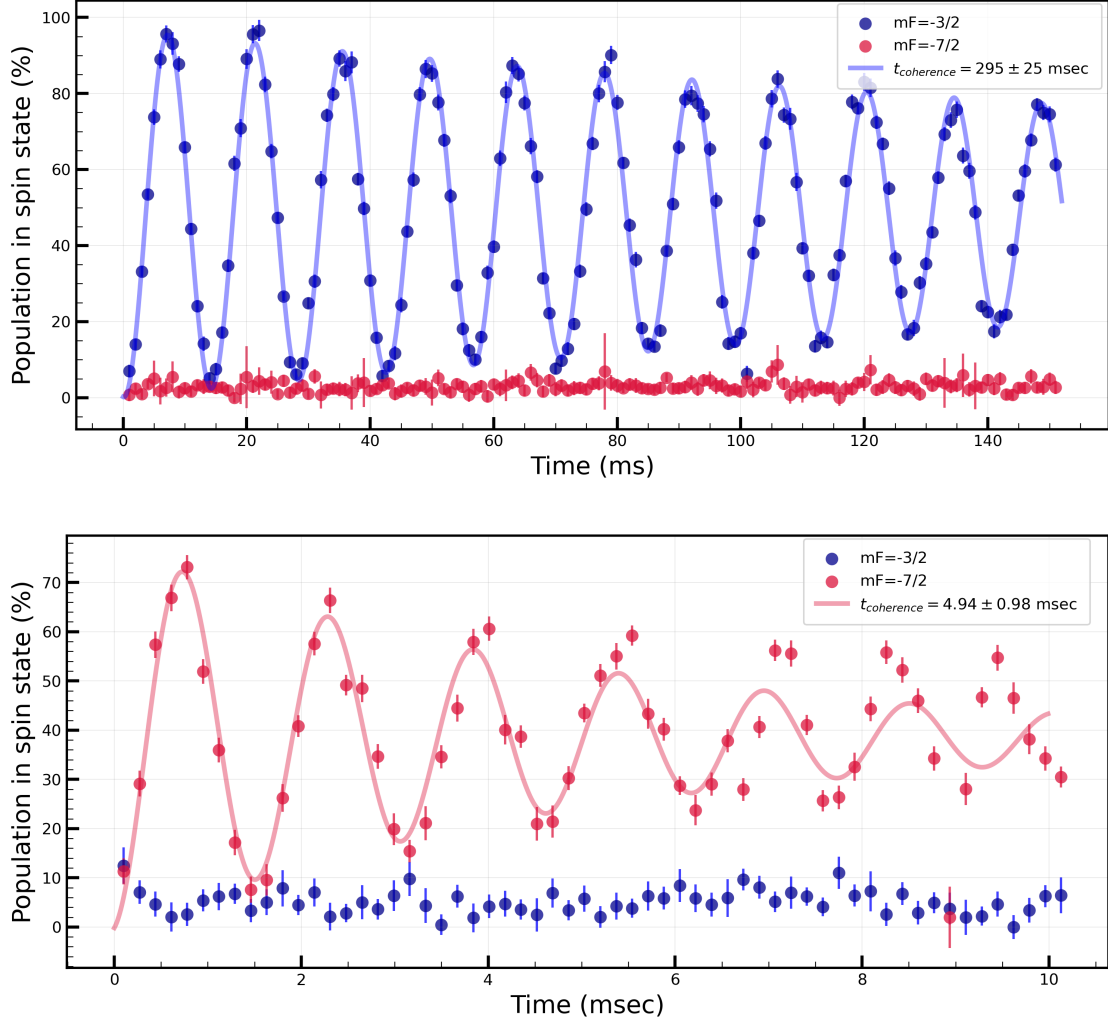
Figure 12: The figure shows the coherence time measurement of the Rabi oscillations. Both *Beam 1* and *beam 2* have a detuning of -600 MHz from the excited hyperfine state $F = 9/2, {}^3P_1$. In both the plots, blue dots represent spin state $|-3/2\rangle$, and the red dots represent spin state $|-7/2\rangle$. Up: Rabi oscillations between the spin states $|-5/2\rangle \leftrightarrow |-3/2\rangle$. The beam waist at the position of atoms is $320 \pm 5\mu m$. The optical power in the {*beam 1, beam 2*} is kept { ~3.5 mW, 0.8 μW }. Down: Rabi oscillations between the spin states $|-5/2\rangle \leftrightarrow |-7/2\rangle$. The beam waist at position of the atoms is $180 \pm 5\mu m$. The optical power in the {*beam 1, beam 2*} is kept { ~5 mW, 3 μW }.

Consider the situation where the cross-sectional profile of the intensity of the two beams *beam 1* and *beam 2* is Gaussian. The Rabi coupling Ω induced by the beam depends upon the intensity of the beam $\Omega \propto \sqrt{I}$ and the variation of the Rabi coupling along the cross-sectional plane of the beam is defined by the Gaussian profile $\Omega \propto \Omega^{max} \exp\left(-2x^2/w^2\right)$. where Ω^{max} is the maximum Rabi coupling felt by the atoms,

w is the beam waist at the location of the atoms and x is the position of the atomic cloud. Here, I consider the fact that the size of the atomic cloud is small compared to the beam waist. I am interested in knowing the variation of the Rabi couplings as the function of x along the cross-sectional profile of the beam. The first-order partial derivative of the Rabi coupling induced by the *beam 1* concerning the position of the atoms x is given by the equation:

$$\left| \frac{\partial \Omega_1}{\partial x} \right| \sim \frac{2x}{w^2} \Omega_1 \tag{2.5.4}$$

Therefore change in Rabi coupling due to *beam 1* only can be aprroximated as $\delta(\Omega_1) = \frac{2\,x\,\delta x}{w^2} \Omega_1$. Where δx is the size over which this change occur. The condition that must be satisfied for maintaining the homogeneous Rabi coupling over the size of the atom cloud Δx is given by:

$$\frac{\Omega_1 \Omega_2}{\Delta} >> \delta \left(\frac{\Omega_1^2}{\Delta} \right) \tag{2.5.5}$$

$$>> 2 \frac{\Omega_1}{\Delta} \delta(\Omega_1) \tag{2.5.6}$$

$$>> 2 \frac{\Omega_1}{\Delta} \frac{2\,x\,\delta x}{w^2} \Omega_1 \tag{2.5.7}$$

This leads us to the following condition:

$$\frac{\Omega_2}{\Omega_1} >> \frac{4x\delta x}{w^2} \tag{2.5.8}$$

In the above derivation Δ is the detuning to the excited state and $\frac{\Omega_1 \Omega_2}{\Delta}$ is the effective Rabi coupling. Furthermore, in our experimental scheme to isolate the system of two levels, we require $\Omega_1 >> \Omega_2$. Combining these two conditions, we can obtain the inequality:

$$1 >> \frac{\Omega_2}{\Omega_1} >> \frac{4.x.\delta x}{w^2} \tag{2.5.9}$$

For the typical experimental parameters $\Omega_1/\Omega_2 \sim 70$. The in situ size of the atomic cloud is approximately 2 μm. Initially, the beam waist at the location of the atomic cloud was 180 ± 5μm. After putting all these parameters in the equation 2.5.9, we find out that, to maintain the uniform Rabi coupling throughout the atomic cloud, the

position of the atomic cloud should be within the range of $x \ll (0.64 \pm 0.02)w$. Here, w is the waist of the beam. However, our current beam alignment procedure allows the accuracy of the order of w. That is not sufficient to fulfill this condition. One way to improve this accuracy is to increase the beam waist at the location of the atoms. I did the same by putting the telescope with approximately 1.8 linear magnification.

Figure 12 bottom shows the Rabi oscillations with beam waist $180 \pm 5\mu m$ at the atoms, while the top figure shows the Rabi oscillations when the beam waist increased to $320 \pm 5\mu m$. We observe that the period of effective Rabi oscillations in the two figures is different, mainly because of the different beam waist in the two cases. In the two cases for a given power, the intensity felt by the atoms is different. For a fixed detuning Δ to the excited hyperfine state effective Rabi coupling between the spin state $|m_F\rangle \leftrightarrow |m_{F\pm1}\rangle$ is given by the equation:

$$\Omega_{eff} \propto \sqrt{I_1 I_2} \propto \sqrt{\frac{P_1 P_2}{w^2 w^2}} \propto \frac{\sqrt{P_1 P_2}}{w^2} \tag{2.5.10}$$

Where Ω_{eff} is the effective Rabi coupling, $\{I_1, I_2\}$ are the intensities in the two beams respectively. The intensity of the beams depends further on the power (P) and the waist (w). Since the two beams have an identical waist at the position of atoms, we notice the dependence of the effective Rabi coupling on the power and beam waist on the right-hand side of the equation 2.5.10. The measured time period $T = 1/\Omega_{eff}$ for one oscillation in two cases is observed nearly as $T_{\{180,320\}\mu m} = \{1.56, 14.29\}ms$ with a ratio $T_{320}/T_{180} \sim 9$. I call T_{180} period of oscillation when the beam waist was 180 µm and similarly T_{320} period of oscillation when the beam waist was 320 µm. Calculation of $T = 1/\Omega_{eff}$ from the beam waist and power in the two beams gives the ratio T_{320}/T_{180} 8.5 ± 0.5. When taking the two data, I considered the difference in optical power in both beams and documented it carefully. The two results agree, considering uncertainties in beam waist and optical powers. Hence, the change in the period of Rabi oscillation is because the beam waist is different in the two cases.

2.5.3 $\sigma - \sigma$ configuration

In the previous sub-section 2.5.1 , we have seen the Rabi oscillations between the spin states $|m_F\rangle \leftrightarrow |m_F \pm 1\rangle$. In this sub-section, I will present a different scheme in which we drive Rabi oscillations between the spin states $|m_F\rangle \leftrightarrow |m_F \pm 2\rangle$. This scheme expands our ability to manipulate the spin states from $|mF\rangle \leftrightarrow |mF \pm 1\rangle$ to $|mF\rangle \leftrightarrow |mF \pm 2\rangle$ in the ground state $^1S_0$ manifold. I will call this scheme $\sigma - \sigma$

configuration because the two-photon process is the absorption of σ^+ photon in *beam 2* and the emission of σ^- photon inside the same beam and vice versa. The *beam 1* is used only for lifting the degeneracy of the ground state manifold. I will be discussing both the advantages and limitations of this scheme.

As described in the above sub-section 2.2.1, DDS controls the RF input of the two AOMs of the two beams. I modulated this RF output from the DDS that drives *beam 2* with Double-sideband suppressed-carrier (DSB-SC) amplitude modulation [Wikipedia contributors, 2025]. Output after this modulation creates the two sidebands without the carrier. It is a very standard technique used in radio communications. The idea is to tune the frequency difference of the two sidebands with the resonance of two states $|mF\rangle \leftrightarrow |mF \pm 2\rangle$. *beam 1* is detuned far away compared to the difference in the energy levels of the two states but within the limit of the bandwidth of the AOM that is driving this beam. Since *beam 1* intensity is locked, we need to be careful to detune it within the bandwidth of the lock, which is nearly 1kHz. In this scheme, *beam 1* lifts the degeneracy of the ground state quadratically as in the previous scheme. The two sidebands of *beam 2* can drive the two-photon process where one photon absorbed is σ_+ in one sideband and one photon emitted is σ_- in the other sideband and vice versa.
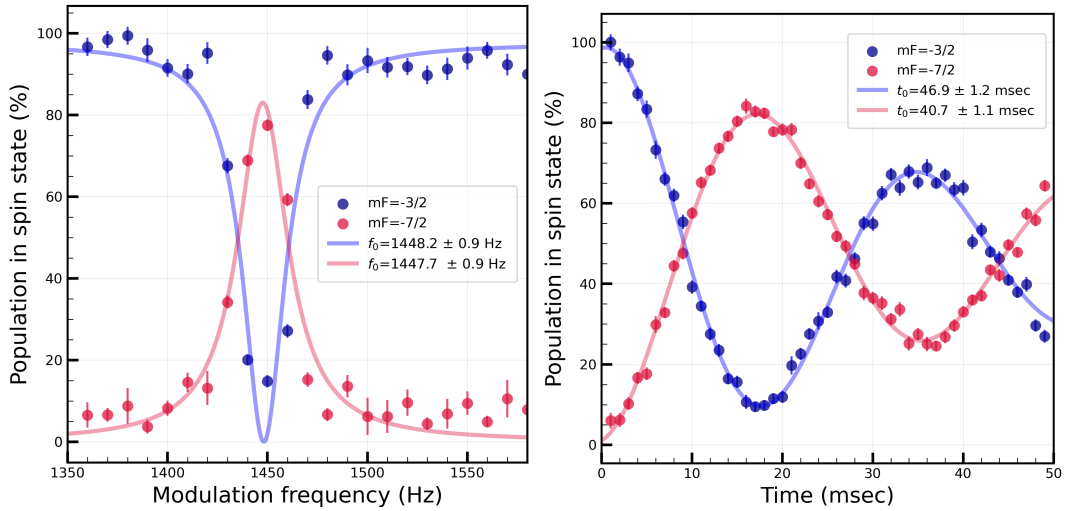
Figure 13: The figure shows the experimental observation of Rabi oscillations in the $\sigma - \sigma$ configuration. The optical power in the {*beam 1*, *beam 2*} is kept { 1.18 mW, 93 μW }. Both beams have a waist of 325 ± 5μm at the location of atoms. Both the beams have a detuning of -600 MHz from the excited hyperfine state $F = 9/2, ^3P_1$. Left: resonance between the spin state $|-3/2\rangle \leftrightarrow |-7/2\rangle$. Right: Rabi oscillations between the spin states $|-3/2\rangle \leftrightarrow |-7/2\rangle$. In both the figure red dots are the spin state $|-7/2\rangle$ and blue dots are spin state $|-3/2\rangle$.

The figure 13, left: shows the resonance between the spin states $|-3/2\rangle \leftrightarrow |-7/2\rangle$. Here, one Rabi oscillation period is larger than the inverse of the width of the resonance. Hence, we can directly fit the plot with a Lorentzian to extract the frequency at which resonance occurs. For the spin state $|-7/2\rangle$, the data is fitted with $P(f) = A/(1 + (f - f_0)/\Gamma)$. Similarly, for the spin state $|-3/2\rangle$, it is fitted with $1 - P(f)$. Where f_0 is the frequency at the resonance, Γ is the width of Lorentzian, and $P(f)$ is the population in the excited state. The fitting parameter gives resonance $f_0 = 1448.2 \pm 1$Hz for the spin state $|-3/2\rangle$, and $f_0 = 1447.2 \pm 1$Hz for the spin state $|-7/2\rangle$. The two resonances are in agreement with each other within the errors. In the figure 13, right: the Rabi oscillations between the same two spin states shown with the coherence time $\{t_{-3/2}, t_{-7/2}\} = \{40 \pm 2, 48 \pm 8\}$ms respectively. Simultaneous measurement of the population in two spin states shows that the population in two spin states varies complementary from each other. Furthermore, the decoherence in both spin states is the same within the fitting error. It is important to notice that the coherence time of the Rabi oscillations in this configuration is shorter than the $\pi - \sigma$ configuration shown in the next subsection 2.5.2. We explain this based on the fact that the polarization in the *beam 2* is not perfectly $\sigma^+ + \sigma^-$ and has a π component in it. The degeneracy lift (at power 1.18 mW) from the *beam 1* is weaker in this case as compared to the $\pi - \sigma$ scheme. Since in $\sigma - \sigma$ configuration only *beam 2* is responsible for the two-photon process, the decoherence effect is enhanced compared to the $\pi - \sigma$ configuration.

Our spin-dependent momentum transfer [Bataille et al., 2020] measurement allows us to measure the populations between spin states separated by $\Delta m_F = 2$. As an advantage while performing the $\sigma - \sigma$ scheme, population measurements for the initial and target spin states are done in a single shot. In this scheme, the two-photon process is by the two sidebands in *beam 2* alone. Due to this, we require approximately one order of magnitude more power in *beam 2* as compared to $\pi - \sigma$ configuration to have a sufficient strong drive. As a consequence of which, the power in *beam 1* reduces (the two beams comes from the same PBS). Hence, for a given output power coming out of the laser head, light shifts on the spin states $|m_F\rangle$ become smaller compared to the $\pi - \sigma$ configuration. Furthermore, it becomes more challenging to isolate a two-level system as per our scheme. Here, I have shown the results for the Rabi oscillations between the spin states $|-3/2\rangle \leftrightarrow |-7/2\rangle$. However, it is straightforward to drive the Rabi oscillations in other spin states. For example, between spin states $|-5/2\rangle \leftrightarrow |-9/2\rangle$.

3 | INTERFEROMETERY WITH QUDIT ENCODED IN NUCLEAR SPINS OF ^{87}Sr

amsey interferometer, originally developed by Norman F. Ramsey in 1949, has become a cornerstone in the field of precision measurement, metrology and quantum computation. This method uses two separated oscillatory fields to precisely measure the energy difference and the coherence between the two quantum states [Ramsey, 1949]. This method can also be applied to internal atomic states as quantum states. With atomic states of ultracold atoms, thermal noise is minimized, leading to longer coherence times and more precise measurements. These precise measurements are applied to study fundamental physics, such as to measure gravitational constant [J. B. Fixler et al., 2007; Lamporesi et al., 2008] and fine structure constant [Cadoret et al., 2008]. A Ramsey interferometer used to build atomic clocks to precisely measure atomic transition frequencies by utilizing phase-dependent interference patterns. Such atomic clocks when utilizing squeezed vacuum states can enhance the sensitivity in the phase of the Ramsey interferometer beyond quantum projection noise, achieving precision at or beyond the standard quantum limit [Kruse et al., 2016; Madjarov et al., 2020; Wineland et al., 1994]. In general, a Ramsey interferometer is a crucial tool for probing quantum states in quantum simulation [Cetina et al., 2016; T. Li et al., 2016] and quantum computing [Lee et al., 2005]. Therefore, it is crucial to explore the scope and applications of Ramsey interferometers employing atomic states.

In this chapter, I will summarize our study using the Ramsey interferometer within two isolated nuclear spins of a large spin ground state manifold of ^{87}Sr. This Ramsey interferometer allows us to measure the energy difference between two isolated nuclear spin states. The Ramsey interferometer encoded in nuclear qubits also provides a precise method to probe qubit gate operations on them. These measurements are crucial because they provide the basis for manipulating qubit states. These measurements are vital in the areas dealing with quantum computation, quantum metrology, and quantum simulation. Next, I will demonstrate how I improved the quality of phase estimation in our experimental data by reducing phase drifts in our interferometer.

Furthermore, the generalization of the two nuclear spin Ramsey interferometers to larger spin interferometers significantly enhances the capacity to perform complex quantum computations, as it increases the dimensionality of the Hilbert space [Godfrin et al., 2018a]. In the next sections, I will explore the broader implications and applications of large spin interferometers. One of the key applications I will discuss is their use as quantum sensors, specifically for making independent measurements of vector and tensor light shifts. Additionally, I will explore the application of large spin interferometers in simultaneously measuring two atomic variables, demonstrating how this technique can be used to measure two non-commuting observables. Discussion of the measurement limit and an extensive study of various noise sources of large spin interferometers will conclude this chapter, showcasing their versatility and power.

3.1 RAMSEY INTERFEROMETER WITHIN NUCLEAR SPINS $|m_F\rangle \leftrightarrow |m_F \pm 1\rangle$ OF ^{87}Sr

Nuclear spins are used for various metrological sensing applications [Jackson et al., 2021; Jarmola et al., 2021; Waldherr et al., 2012]. Nuclear spins in alkaline-earth atoms serve as natural carriers of quantum information and quantum metrology due to their extended coherence times and the ability to control them coherently using magnetic and optical fields. Nuclear spins in platforms such as NV-centres and dopants in silicon are shown to be excellent carriers of quantum information due to their long coherence times [Morishita et al., 2020] [Soltamov et al., 2019]. The ground state of ^{87}Sr is a closed shell with zero electron angular momentum. The nuclear spins within the ground state manifold of ^{87}Sr have weak magnetic moments such that they are highly isolated from the environment. As a result, they are perfect for studying applications that require long coherence. Control of qubits encoded in the nuclear spins of ^{87}Sr has been demonstrated using magneto-optical fields [Barnes, Battaglino, Benjamin J. Bloom, et al., 2022b]. Here, I will present the Ramsey interferometer embedded in the two isolated nuclear spins $|m_F\rangle \leftrightarrow |m_F \pm 1\rangle$ within the ground state manifold. I will begin with an overview of the scheme and then discuss the experimental details.

3.1.1 General idea

As I have demonstrated in the earlier chapter 2, the resonance between the spin states $|m_F\rangle \leftrightarrow |m_F \pm 1\rangle$ can be identified with the help of Raman resonance spectroscopy.

Once we have identified the desired resonances, Rabi oscillations can be driven between the chosen spin states $|m_F\rangle \leftrightarrow |m_F \pm 1\rangle$ or $|m_F\rangle \leftrightarrow |m_F \pm 2\rangle$ based on the $\pi - \sigma$ or $\sigma - \sigma$ scheme. However, for the interferometers I will introduce in this chapter, I will stick to the $\pi - \sigma$ scheme. In this section, I will present two types of Ramsey interferometers between the nuclear spin states $|m_F\rangle \leftrightarrow |m_F \pm 1\rangle$. The first interferometer in which both $\pi/2$ pulses are applied off-resonant with the non zero detuning $\delta = \omega_1 - \omega_2$. The detuning is changed after each experimental cycle to detect the Ramsey spectrum. The second interferometer in which the two $\pi/2$ pulse are applied on resonance. The phase accumulated between the two $\pi/2$ pulses is defined by a phase gate between the two $\pi/2$ pulses. The result is obtained by changing the detuning $\delta = \omega_1 - \omega_2$ or the time duration of the phase gate at each experimental cycle.

3.1.2 Ramsey interferometer with non–resonant $\pi/2$ pulses

A spin-polarized Fermi gas is prepared in the spin state $|-5/2\rangle$. The magnetic field is aligned parallel to the electric field vector of the *beam 1* similar to the Raman resonance spectroscopy scheme introduced in the earlier chapter 2. The magnetic field is parallel to the direction of the electric field vector of the *beam 1* for all the interferometers introduced in this chapter. For further interferometers in this chapter, I shall skip defining the orientation of the magnetic field. Then the intensity of the *beam 1* is ramped to its maximum value $1.9 \ W/cm^2$ in 3.5 ms. At this moment the intensity of *beam 1* is locked at approximately 95 % of the maximum value. As shown in the figure 14 the typical response time of the lock is approximately 2 ms, 4 ms time is given to the lock to settle to a desired intensity. Once the intensity of *beam 1* is locked, the ground state manifold is splitted quadratically with minimum fluctuations. We are now ready to do the interferometery.
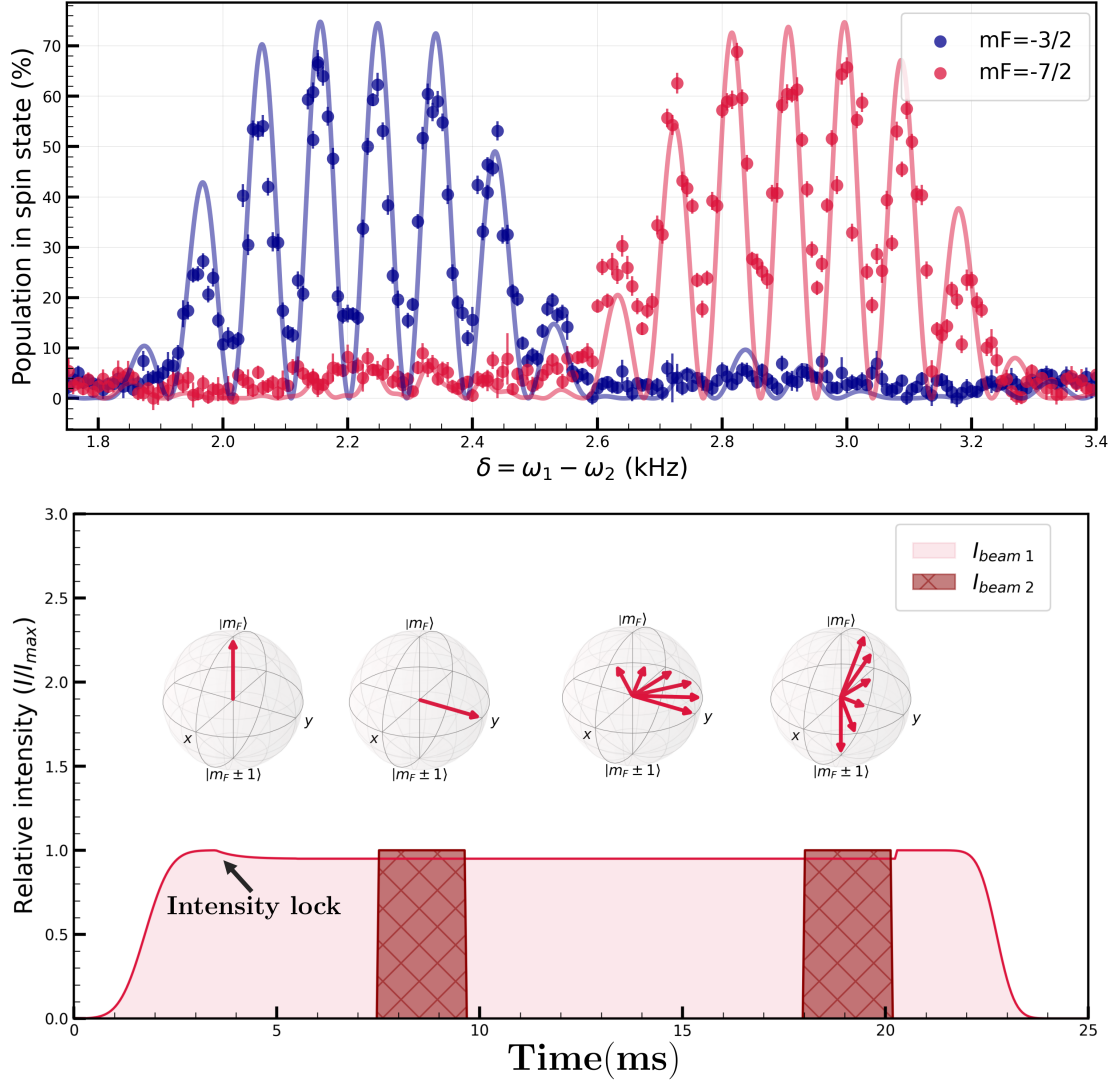
Figure 14: The figure shows two simultaneous Ramsey interferometers for the spin states $|-3/2\rangle, |-5/2\rangle, |-7/2\rangle$ with an actual sequence applied for the experiment. Here, the initial spin state is $|-5/2\rangle$. The intensity of the beams {*beam 1*, *beam 2*} is approximately equal to $\{1.9\,W/cm^2, 0.6\,mW/cm^2\}$ during the Ramsey sequence. Both the beams have a detuning of -600 MHz from the excited hyperfine state $F = 9/2, ^3P_1$. The intensity of *beam 1* was locked during the experiment. The figure on the top shows the measured target spin states. Red dots represent the population in the spin state $|-3/2\rangle$, and the dark blue dots represent the population in the spin state $|-7/2\rangle$. The solid lines are the evolution of the state with the equation 3.1.3. The figure on the bottom shows the intensity profile of both beams during the whole experiment scaled to their respective maximum intensity. The solid-filled region shows the intensity profile for the *beam 1*, and the hatched region shows the intensity profile for the *beam 2*. The Bloch sphere represents the quantum state of the spin states during the Ramsey sequence. In the Bloch sphere, state $|m_F\rangle$ represents the spin state $|-5/2\rangle$, and the state $|m_F \pm 1\rangle$ represents the spin states $|-3/2\rangle$ or $|-7/2\rangle$.

After turning on the *beam 1* for 7.5 ms, the first $\pi/2$ pulse is applied by turning on *beam 2* for 2.17 ms with a square pulse of intensity $0.6mW/cm^2$. The first $\pi/2$ pulse creates the superpostion between the spin states $|-5/2\rangle \leftrightarrow |-3/2\rangle$ or $|-5/2\rangle \leftrightarrow |-7/2\rangle$ depending upon the detuning $\delta = \omega_1 - \omega_2$ between the two beams (the $\pi/2$ is off resonant but the detuning is within the energy difference of the two spin state). Here, the detuning between the two beams is set by the detuning between the driving Rf of the two DDSs that control the AOMs of the two beams. I have shown in the previous chapter that with appropriate relative intensities I_1/I_2 in the two beams *{beam 1, beam 2}*, we can isolate a system of two spin states. Hence, for a given detuning δ, we can isolate either of the systems of two spin states that are $|-5/2\rangle \leftrightarrow |-3/2\rangle$ or $|-5/2\rangle \leftrightarrow |-7/2\rangle$. After the first $\pi/2$ pulse, *beam 2* is turned off for 8.3 ms. During the dark time of 8.3 ms, the superposition of the two spin state $|m_F\rangle \leftrightarrow |m_F \pm 1\rangle$ precesses along the equator on the Bloch sphere with the frequency set by the quantity η that is given by the light shift between the two spin states and the detuning between the two beam $\eta = \Delta E/\hbar + (\omega_1 - \omega_2)$. After the dark time, a second $\pi/2$ pulse is applied for 2.17 ms by turning on the *beam 2* again with a square pulse of $0.6mW/cm^2$. Lastly, the intensity of the *beam 1* is ramped from $1.9W/cm^2$ to approximately zero in 5 ms. As a consequence of the whole sequence, we have applied a Ramsey sequence of two $\pi/2$ pulses for 2.17 ms separated by the dark zone for 8.3 ms. During each experimental cycle, the detuning δ just before the pulse of the first $\pi/2$ pulse is varied in such a way that we cross the two resonances $|-5/2\rangle \leftrightarrow |-3/2\rangle$ or $|-5/2\rangle \leftrightarrow |-7/2\rangle$.

Figure 14 shows the experimental result of the sequence described in the above paragraph. The figure on the bottom represents the sequence of the intensity of the two beams applied during the sequence. The intensity of the *beam 1* is locked at 95% of the maximum intensity during the Ramsey sequence. The hatched region shows the two square pulses applied by turning on the *beam 2*. Bloch spheres illustrate the evolution of the two-spin state system at several stages of the Ramsey sequence. At each stage population of the two spin states involved in the interferometer can be seen as either $\{|m_F + 1\rangle, |m_F\rangle\} = \{|-3/2\rangle, -5/2\rangle\}$ or $\{|m_F - 1\rangle, |m_F\rangle\} = \{|-7/2\rangle, -5/2\rangle\}$. The figure on the top shows the population in the spin states $|-3/2\rangle$ and $|-7/2\rangle$. These spin states are the target states for two Ramsey interferometers with the same initial spin state $|-5/2\rangle$. Blue dots represent the Ramsey interferometer between the spin states $|-5/2\rangle \leftrightarrow |-3/2\rangle$, and red dots represent the Ramsey interferometer between the spin states $|-5/2\rangle \leftrightarrow |-7/2\rangle$. The $\pi/2$ pulses for the sequence are approximately 2.2 ms. Hence, we observe that the envelope of the fringes has FWHM roughly equal to the $1/T_{\pi/2} \approx 460$ Hz. Furthermore, the dark time between the two $\pi/2$ pulses is 8.3 ms. The inverse of the dark time $1/T_{dark}$ sets the interfringe width of approximately

$\approx$ 100 Hz. As a result, we see $\approx$ 4.5 fringes inside the FWHM of the envelope. The experimental output agrees with the expected number of fringes inside the envelope.

Now, I'll proceed to compare the experimental findings with the theoretical framework. Consider the first Hamiltonian $\hat{\mathcal{H}}_\mu$:

$$\hat{\mathcal{H}}_\mu = \begin{pmatrix} E_{-3/2} - \hbar\delta & \hbar\Omega_{-5/2}^{-3/2} & 0 \\ \hbar\Omega_{-5/2}^{-3/2*} & E_{-5/2} & \hbar\Omega_{-7/2}^{-5/2} \\ 0 & \hbar\Omega_{-7/2}^{-5/2*} & E_{-7/2} + \hbar\delta \end{pmatrix} \tag{3.1.1}$$

within the manifold of the three spin states $|-3/2\rangle, |-5/2\rangle, |-7/2\rangle$. The Hamiltonian 3.1.1 governs the evolution of the quantum state when both beams are activated. The diagonal part of the Hamiltonian describes the light shifts between the spin states while also considering detuning δ between the two beams, and the off-diagonal part gives the Rabi couplings between the two neighboring spin states. The second Hamiltonian $\hat{\mathcal{H}}_\nu$:

$$\hat{\mathcal{H}}_\nu = \begin{pmatrix} E_{-3/2} - \hbar\delta & 0 & 0 \\ 0 & E_{-5/2} & 0 \\ 0 & 0 & E_{-7/2} + \hbar\delta \end{pmatrix} \tag{3.1.2}$$

describes the situation when only *beam 1* is activated. The unitary operators $\hat{U}$ corresponding to these Hamiltonians is defined by $\hat{U} = exp(-i\hat{\mathcal{H}}t/\hbar)$, where $\hat{\mathcal{H}}$ can be either of these Hamiltonians. Within the Hilbert space of three spin states, the initial spin state evolves according to the series of unitary operators which are described by the equation:

$$|\psi\rangle = \hat{U}_\mu(T_{\pi/2})\,\hat{U}_\nu(\tau)\,\hat{U}_\mu(T_{\pi/2})|-5/2\rangle$$
$$\text{where,}\quad \hat{U}_{j\in\{\mu,\nu\}} = exp\left(-i\hat{\mathcal{H}}_j t/\hbar\right) \tag{3.1.3}$$

The first operator creates the superposition between the spin states $|m_F\rangle \leftrightarrow |m_F \pm 1\rangle$ when the initial spin state is $|m_F\rangle$. The second operator is for the free evolution during the time τ when the *beam 2* is deactivated. The atoms are dressed during this time, and there are no two-photon transitions except from the *beam 1* itself. Lastly, there is

the third operator for the second $\pi/2$ pulse. This pulse brings the atoms to the target state if the time τ is zero. Time integration of the evolution equation 3.1.3 determines the evolution of the initial spin state.

The solution of the evolution equation with the experimental timings of $\pi/2$ pulse duration and the dark time is plotted on the top of the figure 14 as the solid lines. The number of fringes of the theoretical model coincides with the experimental results. For the Ramsey interferometer between the spin states $|-5/2\rangle \leftrightarrow |-7/2\rangle$ and $|-5/2\rangle \leftrightarrow |-3/2\rangle$, the central fringe is the bright fringe for both the theoretical model and the experimental results. For these spin states, the resonance is found by fitting the envelope with a Gaussian and pointing the center at the detuning of 2.92 ± 0.02 kHz. Similarly for the spin states $|-5/2\rangle \leftrightarrow |-3/2\rangle$ at 2.25 ± 0.02 kHz.

Here, I presented that we drive a Ramsey interferometer for the chosen nuclear spin states within the ground state manifold of the ^{87}Sr. In the context of $\pi - \sigma$ configuration, two spin states within the ground state manifold can be deterministically selected for Ramsey interferometry (effective Rabi frequency $<<$ Tensor light shift). From the experimental data we can simultaneously determine the resonance and the Rabi couplings between the two spin states. The proper choice of the Rabi pulse time and the resonance helps to isolate the two-level system for the interferometry, which avoids the leakage of the interferometer population in the neighboring spin states. In later section on high-dimensional interferometry, we shall see how critical it is to select these parameters to avoid interference between the two Ramsey interferometers. We will now continue our discussion with the Ramsey interferometer with the resonant $\pi/2$ pulses.

3.1.3 Ramsey interferometer with resonant $\pi/2$ pulses

In the data I just presented, the contrast of the interferometer reaches its peak at resonance, where the system is most sensitive to the detecting phase of the interferometer. By applying a resonant $\pi/2$ pulse, we can selectively isolate and control a specific pair of spin states within the ground state manifold. Additionally, when the detuning δ is varied between the two $\pi/2$ pulses, it only affects the phase of the interferometer without touching its contrast, allowing us to adjust the phase on resonance with the selected spin states. This decoupling offers more flexibility and precision in experiments, enabling the measurement of physical quantities sensitive to the interferometer's phase. In our case, this type of interferometer is sensitive to the light shift for the selected spin states.

For this interferometer, a spin-polarized Fermi gas is prepared in the spin state $|-5/2\rangle$. *Beam 1* is turned on and locked the same way as described in the earlier subsection. The first $\pi/2$ pulse is applied by turning on *beam 2* for 3.16 ms with a square pulse of intensity 0.7 mW/cm^2. At the resonance, the first $\pi/2$ pulse creates the superposition between the spin states $|-5/2\rangle \leftrightarrow |-7/2\rangle$ with equal population. After the first $\pi/2$ pulse, *beam 2* is turned off immediately. Next, the phase gate is applied (by switching the frequency of the DDS) during the dark time when the *beam 2* is off. It should be noted that during the phase gate *beam 1* remains active, creating light shifts on the atoms. Hence, the dark time of the interferometer is not truly dark as there is still the light-matter interaction. But for simplicity, I shall call this time the dark time. Because the *beam 1* is on during the phase gate, the overall detuning during the phase gate is given by $\eta = \Delta E/\hbar + (\omega_1 - \omega_2)$, ΔE being the spin-dependent light shift. For the experimental data that I will present, I kept the frequency difference between the two beams $\omega_1 - \omega_2 = 0$. Hence, the overall detuning for this interferometer becomes $\eta = \Delta E$. The phase evolution of the spin states during the phase gate is given by $\phi = \eta t$. As shown in the figure 15, the superposition of the two spin state $|m_F\rangle \leftrightarrow |m_F \pm 1\rangle$ precess in the plane along the equator on the Bloch sphere during the phase gate. After the phase gate, a second $\pi/2$ pulse is applied for 3.16 ms by turning on the *beam 2* again with a square pulse of 0.7 mW/cm^2. Lastly, the intensity of the *beam 1* is ramped from 2 W/cm^2 to zero in 5 ms. As a consequence of the whole sequence, we have applied a Ramsey sequence of two $\pi/2$ pulses for 3.16 ms separated by a phase gate. It's worth mentioning that before and after the phase gate, due to technical limitations, there is a dead time of 300 μs and 100 μs when only *beam 1* remains on. During these times, the interferometer phase evolves according to the detuning set during the last operation.
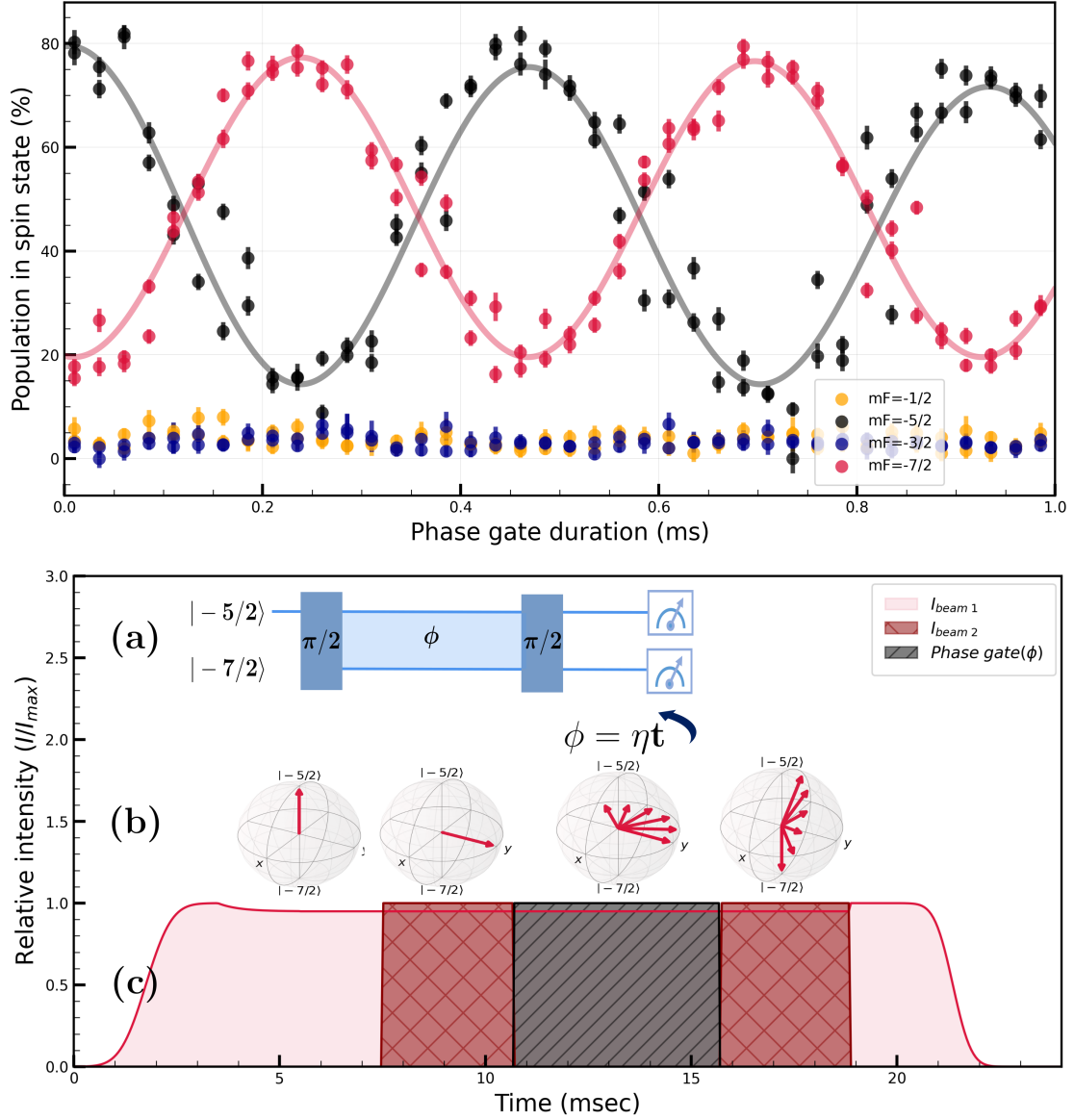
Figure 15: The figure shows the Ramsey interferometer for the spin states $|-5/2\rangle \leftrightarrow |-7/2\rangle$. Here, the initial spin state is $|-5/2\rangle$. The intensity of the beams {*beam 1*, *beam 2*} is approximately equal to {2 W/cm^2, 0.7 mW/cm^2} during the Ramsey sequence. Both the beams have a detuning of -600 MHz from the excited hyperfine state $F = 9/2,^3 P_1$. The intensity of *beam 1* was locked during the experiment. Up: Both initial and target spin states are measured. Red dots represent the population in the spin state $|-7/2\rangle$, and the black dots represent the population in the spin state $|-5/2\rangle$. Down (a): represents the effective qubit operation during the Ramsey sequence. Down (b): The Bloch sphere represents the quantum state of the spin states during the Ramsey sequence. Phase accomulated during the phase gate is given by $\phi = \eta\tau$. Down (c): The intensity profile of both beams during the whole experiment scaled to their respective maximum intensity. The solid-filled region shows the intensity profile for the *beam 1*, and the red Hatched region shows the intensity profile for the *beam 2*. The black Hatched region shows the duration of the phase gate applied. The x-axis during the phase gate does not represent the actual duration and is re-scaled for better visibility. The figure represents the actual sequence applied for the experiment.

The circuit diagram, evolution of the state at each stage of the interferometer, and intensity profiles of the two beams are all shown in the bottom figure 15 combined. Here, the phase accumulation due to the phase gate becomes $\phi = \eta\tau$. The precession time τ during the phase gate is varied from 10 μs to 1.01 ms and the experimental results are plotted in the figure top 15. The data is taken with two data points for each value of time. Since our spin-dependent momentum transfer protocol [Bataille et al., 2020] measures the population of spin states that differ by $\Delta m_F = 2$, the complete dataset was taken in the two experimental run. The data for the spin states $|-7/2\rangle$ and $|-3/2\rangle$ was taken in the first run and the data for the spin states state $|-5/2\rangle$ and $|-1/2\rangle$ was taken in the second run. Figure up 15 shows the results of the experimental data. We observe that there is no population leakage in the nearby spin state such as $|-3/2\rangle$, and we see oscillation in the population between the desirable spin states.

Moving on, I will compare the experimental results with theory. The evolution of the state during the interferometer is given by the equation:

$$|\psi(t)\rangle = \hat{U}_\mu(T_{\pi/2})\,\hat{U}_\nu(\tau)\,\hat{U}_\mu(T_{\pi/2})|-5/2\rangle$$
$$\text{where,} \quad \hat{U}_{j\in\{\mu,\nu\}} = exp(-i\hat{\mathcal{H}}_j t/\hbar) \tag{3.1.4}$$

Where the Hamiltonians are described by the equations 3.1.1 and 3.1.2 at resonance to the addressed spin states. The experimental data in figure 15 is fitted with the function $P_{m_F} = A\sin^2(\frac{\omega_{m_F}}{2}\tau + \phi) + \phi_0$ for each spin states. In this function, τ is the phase gate time and other symbols have their usual meaning. The fitting of the function in the respective spin state population gives the frequency of the fringe of the Ramsey interferometer, which is equal to the energy difference between the two spin states involved in the Ramsey interferometer. This energy difference is the combination of the linear Zeeman shift from the external magnetic field and the light shift caused by the *beam 1*. The energy difference is found to be $\Delta E_{-5/2}^{-7/2}/\hbar = \{2.15 \pm 0.02, 2.18 \pm 0.02\}$ kHz when fitted on the population in spin state $|-5/2\rangle$ and $|-7/2\rangle$ respectively. Both the fitting results agree with each other within the fitting error bars. Additionally, the light shift is close to the theoretical prediction 2.29 ± 0.02 kHz made for the zero detuning δ at the same intensity in the *beam 1*. Here, the difference of 0.1 kHz is only because of the day-to-day fluctuations of the intensities of the *beam 1* at the location of the atoms. These fluctuations come from the drift in the aiming of the beam, the efficiency of the fiber coupling, and the locking intensity.

One advantage of the Ramsey interferometer over the Raman spectroscopy scheme introduced in the former chapter 2 is that if the phase of the fitting function is calibrated, we only require one data point of the interferometer to estimate the energy splitting (light shift + Zeeman shift) ΔE. Therefore, for maximum sensitivity of the interferometer towards the energy splitting, we rely on identifying the resonances through the Ramsey interferometer at non-zero detuning or the Raman resonance. Moving on, I have shown the application of this interferometer as a sensor for light shifts depending upon the chosen spin states within the constraint $|m_F\rangle \leftrightarrow |m_F \pm 1\rangle$. However, the Ramsey interferometer does not differentiate between the tensor light shift, and the combination of vector light shift and the linear Zeeman shift caused by an external magnetic field. I shall demonstrate later in this chapter that the two can be detected and separated in a single shot if we run an interferometer by extending the Hilbert space to four spin states within the ground state manifold.

We now shift our focus to measuring the coherence of the qubit within the nuclear spins. Coherence time is an essential quantity in quantum systems. It describes the duration, a qubit can maintain its quantum state. To measure this coherence time, I take the opportunity to use the interferometer described in this section.

3.2 COHERENCE ASSOCIATED WITH THE QUBIT ENCODED IN NUCLEAR SPINS OF ^{87}Sr

Advances in quantum computing and metrology using neutral atoms depend upon the ability to encode qubits for longer periods. This period is usually characterized by the qubit coherence time. The qubit's coherence time of a device determines its capacity to perform multiple quantum gate operations. Neutral atoms with closed electronic shells favor the long coherences due to purely nuclear spin. When comparing the nuclear spin degrees of freedom to electronic spin degrees of freedom, consistent results have shown longer qubit coherence, with timescales reaching seconds [Hensen et al., 2020; Maurer et al., 2012; Park et al., 2017]. A few examples with long-lived nuclear spins qubits are demonstrated with Yb atoms [Huie et al., 2023; Lis et al., 2023; Norcia et al., 2023]. [Hölzl et al., 2024] demonstrated a 2.5 ms qubit lifetime at room temperature with Sr circular Rydberg atoms. Recently, qubits encoded in the nuclear spin states of ^{87}Sr approaching a coherence of about a minute is demonstrated [Barnes, Battaglino, Benjamin J Bloom, et al., 2022a]. In this section, I will characterize

the coherence time of the qubit encoded in the nuclear spins within the ground state manifold of ^{87}Sr in our experiment.
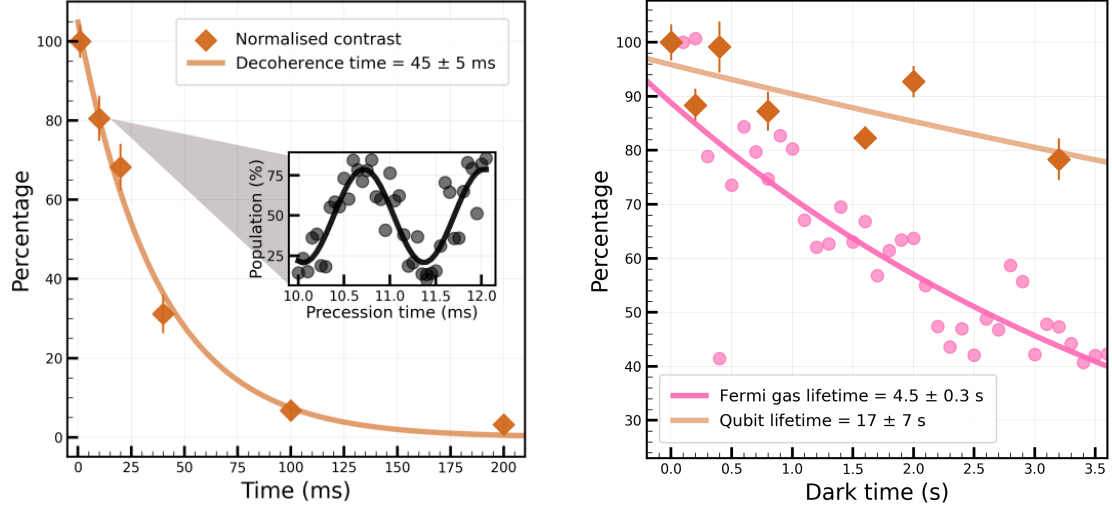

Figure 16: Measurement of the coherence time of the qubit prepared in the spin states $|-5/2\rangle \leftrightarrow |-7/2\rangle$. All the quantities are normalized to the first data point and presented in percentages. Diamond points in brown color represent the contrast of the interferometer with respective fitting error bars. Figure on the left shows the qubit coherence time inside the *beam 1*. The time is measured from the end of the first $\pi/2$ pulse to the beginning of the second $\pi/2$ pulse. The inset figure shows an example data set used to calculate one data point for the contrast. The figure on the right shows the contrast of the qubit in the dark. Notice that *beam 1* is turned off during the dark time. The coherence time is compared with the Fermi gas lifetime, represented by the pink dots.

I used a Ramsey sequence to measure the qubit's coherence time introduced in the preceding section. Initially, I prepared a qubit between the spin states $|-5/2\rangle \leftrightarrow |-7/2\rangle$ with a respective $\pi/2$ pulse duration of 3.46 ms. To probe this qubit using a Ramsey sequence, a symmetric $\pi/2$ pulse is applied. The effective detuning η between the two $\pi/2$ pulses is kept such that the duration of one interferometer's fringe is of the order of a millisecond. I investigated the following two cases. In case one, *beam 1* remains active between two $\pi/2$ pulses, and the qubit state precesses in the presence of the tensor light shift and an external magnetic field. The time between the two $\pi/2$ pulses is then varied within a window of 2 ms to collect approximately 1.5 fringes. In case two, following the initial $\pi/2$ pulse, the intensity of *beam 1* is decreased to zero over 2 ms and then increased symmetrically to the maximum value before the second $\pi/2$ pulse. When the intensity of the *beam 1* is zero, true dark time is varied to within a 2 ms interval to record approximately 1.5 fringes. In both

scenarios, I collected various datasets of 1.5 fringes at different times. For each dataset, the contrast of the fringe is calculated. I calculated the contrast of fringe by plotting the histogram, which is the relative population in the spin state versus the number of experimental cycles. To estimate the error bars on the contrast, I used bootstrapping [Bradley Efron and Tibshirani, 1993]. This involved resampling the data 1000 times with replacement, recalculating the contrast for each resample, and then computing the standard deviation of these contrasts to serve as the error estimate.

Figure 16 displays the decaying amplitude of the Ramsey interferometer. Each dataset is fit using the function $A = 100 \exp(-t/t_0)$. Where A is the contrast of the fringe (in percentage) and t_0 represents the $1/e$ time. The figure on the left illustrates the decaying contrast of the Ramsey interferometer for case one in the presence of tensor light shift. We observe a 45 ± 5 ms $1/e$ time in the left figure. The figure on the right shows the contrast of the Ramsey interferometer in case two when the *beam 1* is not active. Please note that in the second case, it takes 4 ms to turn off and on *beam 1* again. Hence, qubit spends 4 ms precession time in the presence of *beam 1* on top of the respective $\pi/2$ pulse time. The $1/e$ time is observed as 17 ± 7 s. This time is also compared with the $1/e$ time of the polarized Fermi gas that is 4.5 ± 0.3 s. We noticed that the dark coherence time of the qubit is longer compared to the lifetime of the Fermi gas.

We observed that the primary cause of qubit decoherence is the presence of tensor light shift which can be explained by spontaneous emission from *beam 1*. I demonstrate that removing the tensor light shift increases the coherence of the qubit by at least two orders of magnitude 10^2. As a result, qubit coherence can be retained for seconds in the presence of the external magnetic field. Generally in the second case, qubit coherence time can be primarily limited by inhomogeneities in the external magnetic field and intrinsic atomic properties such as collisional decoherence. ^{87}Sr is weakly sensitive to external magnetic field fluctuations due to the purely nuclear spin in the ground state. As a result, collisional decoherence is supressed. This makes nuclear spin qubits in the dark a good platform to probe collision-dependent decoherence, as we shall see in the following chapter. In addition to the qubit decoherence, we lose control over the interferometer phase in the presence of the tensor light shifts for the timescale of 10s of ms. In the second case, we lose the phase control at the timescale of seconds. I will discuss the two cases in the following section.

With the coherence time of the qubit measured, we now turn our attention to addressing the phase noise in the interferometer, which is essential for preserving the

precision of the measurement. In the following section, we will explore methods to characterize phase noise and attenuate it.

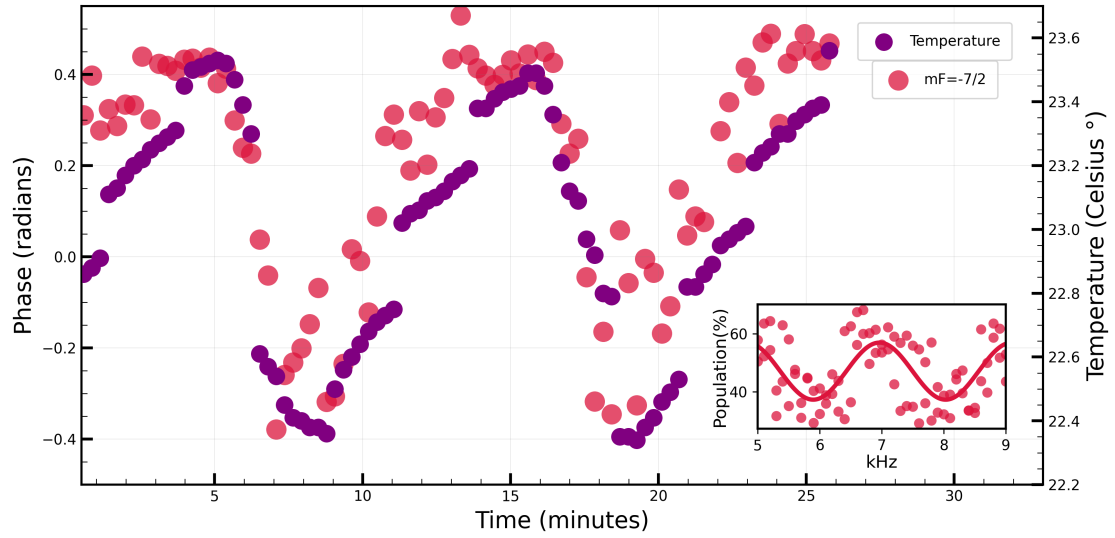## 3.3 ATTENUATION OF THE PHASE NOISE OF THE INTERFEROM-ETER

Figure 17: Dynamics of phase drift in radians for the population in the spin state $|-7/2\rangle$, which corresponds to the left y-axis. The dynamics of room temperature are plotted alongside the right y-axis. The red dots indicate the population in the spin state $|-7/2\rangle$, while the purple dots represent the room temperature. The inset figure depicts the spin state population $|-7/2\rangle$ of an interferometer between the spin states $|-5/2\rangle \leftrightarrow |-7/2\rangle$. The population in the spin state $|-7/2\rangle$ are observed for an interferometer phase tuned in the middle point of the fringe slope, 6.5 kHz.

In this section, I will identify the technical sources for enhanced phase noise and characterize it. This will improve the quality of our experimental results.

To investigate the phase noise of our interferometric schemes, I conducted an interferometer experiment between the spin states $|-5/2\rangle \leftrightarrow |-7/2\rangle$ with a total interferometer time of approximately 16 ms. The time is determined from the beginning of the first $\pi/2$ pulse to the end of the second $\pi/2$ pulse. The phase gate for this interferometer was applied for the duration of 0.5 ms (i.e. the time between the $\pi/2$ two pulses). The detuning δ between the two beams during the phase gate is varied from 5 kHz to 9 kHz. The inset in figure 17 shows the population in the spin state

$|-7/2\rangle$ for the interferometer. For measuring the phase noise at a fixed phase gate frequency, the phase of the interferometer is fixed approximately on the middle of the slope of one of the fringes in the inset plot. I chose 6.5 KHz for this data set. The population in the spin state $|-7/2\rangle$ is then monitored after each 17-second experimental cycle to observe dynamics at this fixed phase. During each experimental cycle, the room temperature is recorded by a temperature gauge. The primary figure 17 depicts the simultaneous dynamics of phase and room temperature. To observe a sufficient number of drift cycles, the data is recorded for approximately 25 minutes.

The inset figure 17 is fitted with the function $P_{-7/2} = A\sin(\phi(\omega))$ to extract the contrast A and the phase $\phi(\omega)$ of the interferometer at each ω. Therefore, we know the mean phase $\phi(6.5\text{kHz})$ at $\omega = 2\pi\,6.5$ kHz. The following experiment measures the dynamics of the phase. The phase variation after each experimental cycle is obtained by fitting the function $\phi(t) = \arcsin(P_{-7/2}(t)/A) - \phi(6.5\text{kHz})$ to the experimental data. The main figure 17 shows the dynamics of $\phi(t)$ in radians along the left y-axis, while the ambient temperature in $^\circ$C of the room is represented along the right y-axis. Please note that for better data readability, I have applied a transformation $\phi(t) = -\phi(t)$ that does not perturb the phase dynamics. We observed that the room temperature and phase of the interferometer follow dynamics with similar period. To measure the correlation between the two quantities, I take the help of the Pearson correlation coefficient. If X is the room temperature and Y is the phase of the interferometer. Then, the Pearson correlation coefficient between the two quantities is given by $\rho_{X,Y} = \text{cov}(X,Y)/\sigma_X\sigma_Y$ [Pearson, 1896]. The coefficient $\rho_{X,Y}$ lies in the interval $[-1, 1]$, where 0 indicates no linear relationship and |1| indicates a perfect linear relationship between X and Y. In our case, the $\rho_{\phi,Temp}$ is found to be 0.81 ± 0.04, which indicates high linear relationship between the two quantities.

We now look for the most probable cause of this phase variation. The total shift on the atoms is caused by the combination of the Zeeman shift and light shift. The current in the coils that generate the magnetic field has the stability of 10 ppm throughout a shift of 1 $^\circ$C temperature. 10 ppm is equivalent to 10 mHz fluctuation for a typical 1 kHz Zeeman shift. The 10 mHz fluctuation integrated over the phase gate time 0.5 ms appears as 3.2×10^{-5} rad phase noise, which is negligible as compared to the phase drift in the figure 17. We describe the air conditioner of the room as the source of the enhanced phase variation. The air from the air conditioner blown by the fan affects the polarization maintained in the fiber that delivers light in *beam 1* and *beam 2* to the experimental cell. The gradual drifts in polarization translate to a slow drift of the vector light shift induced on the atoms, resulting in the drift of the phase in the interferometer.
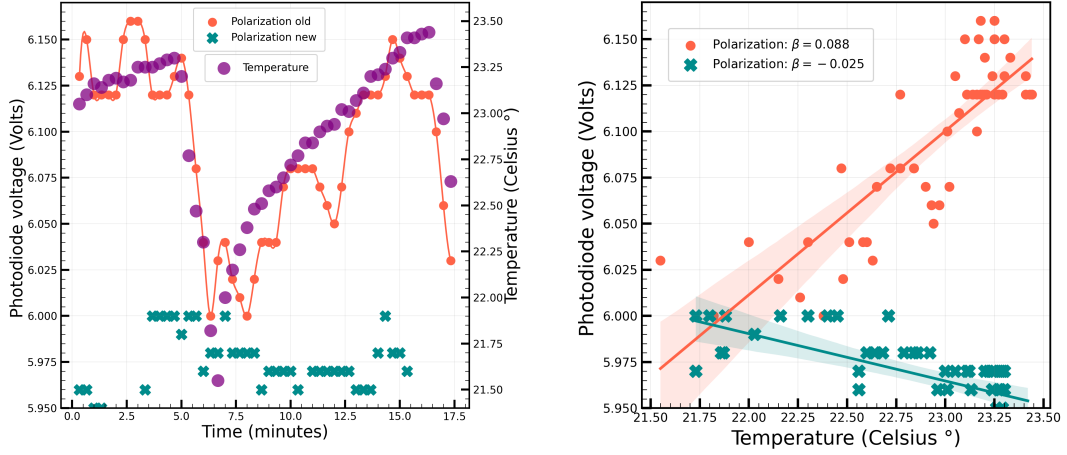
Figure 18: Correlation between the polarization maintained inside the fiber used for guiding the *beam 1*, *beam 2* to the experimental cell and the room temperature. The figure on the left shows the correlation between fiber polarization and room temperature. Purple dots represent the measured temperature, the tomato dots represent the measured photodiode voltage before the improvement of the polarization maintenance, and the cyan cross represents the polarization maintenance after the improvement. The figure on the right shows the correlation plot from which the Pearson correlation coefficient is extracted. Furthermore, regression analysis indicates the sensitivity of polarization to room temperature.

Figure 18 left shows the correlation between the measurement of the polarization in the fiber and the ambient temperature. To measure the polarization drift, the light passing through the experimental cell is filtered by a polarizing beam splitter (PBS) alligned to 50-50 split in transmission and reflection for maximum senstivity, and the transmitted intensity (*beam 1*) is then measured using a photodiode. The photodiode voltage is plotted on the left y-axis. Furthermore, the temperature is recorded with the help of the picolog software, which measures the voltage from the temperature gauge. The temperature is represented on the right y-axis. Each data point is collected every 20 seconds to examine the slow drift of polarization. The correlation between polarization and temperature is assessed by calculating the Pearson correlation coefficient. We found the Pearson coefficient as $\rho = 0.85 \pm 0.03$. This suggests that the polarization inside the fiber is strongly correlated with the room temperature.

A technique to characterize further is to see how sensitive the polarization drift is to ambient temperature. This can be studied by plotting photodiode voltage versus room temperature. Figure 18 right shows the variation of the photodiode voltage with

the room temperature. The linear regression analysis $Y = X\beta + \varepsilon$ gives the slope β of the data. The slope β is evaluated as 0.088 ± 0.008 for $\rho = 0.85 \pm 0.03$. I wrapped the fiber in an insulating foam tube to protect it from temperature fluctuations. Following this modification, we discovered that the sensitivity β falls to -0.025 ± 0.004 with a Pearson correlation coefficient $\rho = -0.60 \pm 0.09$. Note that all the errors in the estimation of ρ and β are computed by bootstrap resampling [B. Efron, 1979]. Based on the investigation, we see that the polarization drift sensitivity to ambient temperature is reduced by a factor of roughly 3.5. This improvement marks a significant step in enhancing the stability of our system. Moving forward, we will now explore high-dimensional interferometry, focusing on the use of a qudit encoded in the nuclear spins of ^{87}Sr to explore its applications.

3.4 HIGH DIMENSIONAL INTERFEROMETRY WITH A QUDIT ENCODED IN NUCLEAR SPINS OF ^{87}Sr

Coherent quantum control across a large Hilbert space is necessary for a scalable quantum device. One way to build a large-scale quantum device is to increase the number of two-state quantum devices that encode the information as a qubit (d=2). In contrast, an alternate path for scaling is to make use of d-state devices that encode the information in the form of a qudit (d>2) [Bullock et al., 2005]. By utilizing d-state devices, the Hilbert space expands significantly. The enriched Hilbert space allows for more robust quantum algorithms [Kiktenko et al., 2015], improved error correction techniques [Muralidharan et al., 2017], and the potential for more efficient quantum simulations [Kaltenbaek et al., 2010; Neeley et al., 2009] and computations [Babazadeh et al., 2017; Cozzolino et al., 2019; Lanyon et al., 2009]. The number of qubits required to store the same amount of information as a qudit of d-dimension is by $n = \log_2 d$. ^{87}Sr with its 10 nuclear spin states in the ground state manifold has the potential to encode qudit up to (d=10). Such a qudit carries the same information as approximately 3.3 qubits. Along with the increase in the information capacity, High dimensional states have higher noise resilience [Cozzolino et al., 2019].

Typically, a Ramsey interferometer is utilized for measuring both the qubit state and its coherence. A generalized version of a Ramsey interferometer can be implemented in a d-dimensional Hilbert space. Such an interferometer has more potential applications due to the access of multiple phases. For instance, a generalized version of the Ramsey interferometer with nuclear spin qudit in molecules performing various

quantum gate operations and measuring the three-state coherence of the qudit has been demonstrated [Godfrin et al., 2018b]. In this section, I will demonstrate a qudit encoded in nuclear spins of ^{87}Sr with d=4 dimension. To illustrate the potential application of the qudit, I will introduce two applications using large spin interferometry. First, a quantum sensor that measures tensor light shift, as well as the sum of the vector light shift and Zeeman shift. Next, simultaneous measurement of two atomic variables.

3.4.1 Double Ramsey interferometer as a quantum sensor for light shifts

In this section, I will introduce a large spin interferometer designed specifically for measuring the light shift within the ground state manifold. Earlier in this chapter, I discussed the use of a Ramsey interferometer as a sensor for detecting light shifts. Following on the foundation, I will now present an interferometer capable of measuring two energy differences within the ground state manifold simultaneously. The simultaneous measurement of two energy difference decouples tensor light shift from the combination of vector light shifts and the linear Zeeman shift. To maintain the continuity with previous discussions, I will refer to this interferometer as the double Ramsey interferometer. This terminology is fitting, as it accurately reflects the operation of two parallel Ramsey interferometers encoded in nuclear spins of ^{87}Sr.

Experimental scheme overview

For this interferometric scheme, a spin-polarized gas is prepared in the spin state $|-5/2\rangle$ for this interferometer sequence. At the beginning of the experiment, after tuning on the *beam 1*, its intensity is locked as described in the earlier experiments. As shown in the figure 19, a $\pi/2$ pulse is applied by turning on the *beam 2* for 3.26 ms with a square pulse between the spin states $|-5/2\rangle \leftrightarrow |-7/2\rangle$. After the first $\pi/2$ pulse, the atoms are in a superposition of the spin state $|-5/2\rangle \leftrightarrow |-7/2\rangle$ with approximately 50 % population per spin state. A second $\pi/2$ pulse is applied for 3.49 ms between the spin states $|-5/2\rangle \leftrightarrow |-3/2\rangle$. There is a 100 µs gap between the first and the second $\pi/2$ pulse for the same reason as other interferometers introduced earlier. Immediately after the second $\pi/2$ pulse, the third $\pi/2$ pulse is applied for 3.49 ms between the spin states $|-7/2\rangle \leftrightarrow |-9/2\rangle$. Overall sequence of three $\pi/2$ pulses creates the superposition of atoms within the manifold of spin states $\{|-3/2\rangle, |-5/2\rangle, |-7/2\rangle, |-9/2\rangle\}$ with approximately equal population in each spin states that is 25 % of the initial population. A phase gate is applied immediately after the third

$\pi/2$ pulse. The phase of the phase gate between the two neighboring spin states is given by $\Delta\phi_{mF}^{mF\pm1} = (\Delta E_{mF}^{mF\pm1}/h + \Delta\omega_{rf})t$ with $\Delta\omega_{rf} = \omega_1 - \omega_2$. After a gap of 100 µs, the fourth $\pi/2$ pulse is applied for 3.49 ms to close the interferometer between the spin states $|-3/2\rangle \leftrightarrow |-5/2\rangle$. Immediately after the fourth $\pi/2$ pulse, the fifth $\pi/2$ pulse is applied for 3.49 ms to close the interferometer between the spin states $|-7/2\rangle \leftrightarrow |-9/2\rangle$. The overall scheme is essentially a combination of two Ramsey interferometers, where one is sensitive to the energy difference between the spin state $|-7/2\rangle \leftrightarrow |-9/2\rangle$ and the other is sensitive to the energy difference between the spin states $|-3/2\rangle \leftrightarrow |-5/2\rangle$.

Quantum sensor for simultaneous measurement of tensor light shift and combined vector light shift with linear Zeeman shift

The double interferometer, which is encoded in the four nuclear spins, allows for the measurement of two distinct fields. In this section, I will present a detailed analysis on the experimental data of a double Ramsey interferometer and how we can process this data to measure two fields.

To collect the experimental data, the time of the phase gate is varied from 10 µs to 930 µs with a sampling of 20 µs. Each data point is one experimental run of the whole sequence. The experiment is run for each data point randomly. The experimental results are depicted in the figure 19. The top of the figure shows the applied experimental sequence of the double Ramsey interferometer. The solid-filled region in the red shows the intensity profile of the *beam 1*. The intensity of the *beam 1* is locked in the same way described in the section for the two-pulse interferometer. The hatched region in red shows the intensity profile of the *beam 2* for the five square pulses applied with their respective duration. The group of three Bloch spheres shows the evolution of the state during the whole sequence. Each Bloch sphere shows the evolution of the quantum state within the $mF \leftrightarrow mF \pm 1$ manifold. Here, I truncated the four spin states manifold $\{|-3/2\rangle, |-5/2\rangle, |-7/2\rangle, |-9/2\rangle\}$ into the set of three two spin states manifolds $\{|-3/2\rangle, |-5/2\rangle\}; \{|-5/2\rangle, |-7/2\rangle\}; \{|-7/2\rangle, |-9/2\rangle\}$ that is represented on the three different bloch sphere. I made this approximation for the sake of visualization. Furthermore, for simplicity i shall call the $\pi/2$ pulse between the spin states $|-5/2\rangle \leftrightarrow |-7/2\rangle$ as κ, $\pi/2$ pulse between the spin states $|-3/2\rangle \leftrightarrow |-5/2\rangle$ as α and $\pi/2$ pulse between the spin states $|-7/2\rangle \leftrightarrow |-9/2\rangle$ as β. The sequence showing the order of $\pi/2$ pulses for the interferometer shown in figure 19 is then $\kappa\alpha\beta\alpha\beta$. Effectively, κ divides the sample into two halves. Each half will be injected independently into a Ramsey interferometer, controlled by two pulses $\alpha\alpha$ or $\beta\beta$ for the different

pairs of spin states. The two interferometers are realized in parallel, the pulses being interlaced.

The figure on the bottom represents the experimental data for the applied sequence $\kappa\alpha\beta\alpha\beta$. In the left figure, the measurement of the population in the spin state $|-3/2\rangle$ (blue) and the population in the spin state $|-7/2\rangle$ (red) is shown. The figure on the right shows the population in the spin state $|-5/2\rangle$ (black) and the population in the spin state $|-1/2\rangle$ (orange). Since the spin state $|-1/2\rangle$ is not part of the interferometer, we observe a flat number of atoms within the experimental noise for the population in this spin state. Looking at the combination of the two figures, we observe that the phase difference of the population in the spin state $|-3/2\rangle$ and $|-5/2\rangle$ is π. Here, we don't measure the population in the spin state $|-9/2\rangle$, which is the complementary population for the spin state $|-7/2\rangle$. The population between the spin states $|-3/2\rangle$ and $|-5/2\rangle$ oscillates with an expected peak to peak amplitude of approximately 35%. We can see in the figure 16, the amplitude of the interferometer with respect to the time spent in the *beam 1*. Since this interferometer requires five $\pi/2$ pulses, the amplitude further drops down to 35% as compared to the ideal percentage of 50%. The population in the spin state $|-7/2\rangle$ has an amplitude of approximately 30 %. The further slight decrement in the amplitude is probably due to the off-resonance of the detuning δ from the energy difference of the two spin states $|-7/2\rangle \leftrightarrow |-9/2\rangle$ (this suggest an imperfect $\pi/2$ pulse). The difference between the frequencies of the two beams $\Delta\omega_{rf}$ is kept zero for this experiment by keeping $\omega_1=\omega_2=110$ MHz (The frequency of the two AOM's). Then the phase of the phase gate for the two simultaneous interferometers is given by $\Delta\phi_{mF}^{mF\pm1} = (\Delta E_{mF}^{mF\pm1}/\hbar)t$. The relative phase $\Delta\phi_{-3/2}^{-5/2}$ of the first interferometer between the spin states $|-3/2\rangle \leftrightarrow |-5/2\rangle$ measures the light shift $\Delta E_{-3/2}^{-5/2} = \hbar.\Delta\phi_{-3/2}^{-5/2}/t$ between the two respective spin states. Similarly the interferometer between the spin states $|-7/2\rangle \leftrightarrow |-9/2\rangle$ measures the light shift $\Delta E_{-7/2}^{-9/2} = \hbar.\Delta\phi_{-7/2}^{-9/2}/t$ with a relative phase $\Delta\phi_{-7/2}^{-9/2}$ between the two spin states.

Moving on, I will compare our experimental data with the theoretical model. The evolution of the state during the double Ramsey interferometer sequence can be described by the equation:

$$|\psi(t)\rangle = \hat{U}_\mu(T_{-7/2}^{-9/2})\,\hat{U}_\mu(T_{-3/2}^{-5/2})\,\hat{U}_\nu(\tau)\,\hat{U}_\mu(T_{-7/2}^{-9/2})\,\hat{U}_\mu(T_{-3/2}^{-5/2})\,\hat{U}_\mu(T_{-5/2}^{-7/2})|-5/2\rangle$$

$$\text{where,}\quad \hat{U}_{j\in\{\mu,\nu\}} = \exp\left(-i\hat{\mathcal{H}}_j t/\hbar\right)$$

$$(3.4.1)$$

In this equation, operator $\hat{U}_\mu(T^{mF}_{mF+1})$ represents the $\pi/2$ pulse between the spin state $|mF\rangle \leftrightarrow |mF+1\rangle$, T^{mF}_{mF+1} being the $\pi/2$ pulse time. Assuming that we can isolate a manifold of four-spin states within the ten-spin state manifold, the Hamiltonians 3.4.2, 3.4.3 fully describe the dynamics of the state. Where $\hat{\mathcal{H}}_\mu$ is the Hamiltonian when both the beams are active and $\hat{\mathcal{H}}_\nu$ is the Hamiltonian when only *beam 1* is active with zero detuning δ.

$$\hat{\mathcal{H}}_\mu = \begin{pmatrix} E_{-3/2} - \hbar\delta & \hbar\Omega^{-3/2}_{-5/2} & 0 & 0 \\ \hbar\Omega^{-3/2*}_{-5/2} & E_{-5/2} & \hbar\Omega^{-5/2}_{-7/2} & 0 \\ 0 & \hbar\Omega^{-5/2*}_{-7/2} & E_{-7/2} + \hbar\delta & \hbar\Omega^{-7/2}_{-9/2} \\ 0 & 0 & \hbar\Omega^{-7/2*}_{-9/2} & E_{-9/2} + 2\hbar\delta \end{pmatrix} \quad (3.4.2)$$

$$\hat{\mathcal{H}}_\nu = \begin{pmatrix} E_{-3/2} & 0 & 0 & 0 \\ 0 & E_{-5/2} & 0 & 0 \\ 0 & 0 & E_{-7/2} & 0 \\ 0 & 0 & 0 & E_{-9/2} \end{pmatrix} \quad (3.4.3)$$

As described earlier, during the phase gate, the operator $\hat{U}_\nu(\tau)$ describes the phase evolution during the time τ. I emphasize that during the phase gate, all spin states evolve at the rate of their respective energy levels. Since the interferometer is closed between the spin states $|-3/2\rangle \leftrightarrow |-5/2\rangle$ and $|-7/2\rangle \leftrightarrow |-9/2\rangle$, we only measure the phase difference accumulated between the spin states that has closing $\pi/2$ pulse.
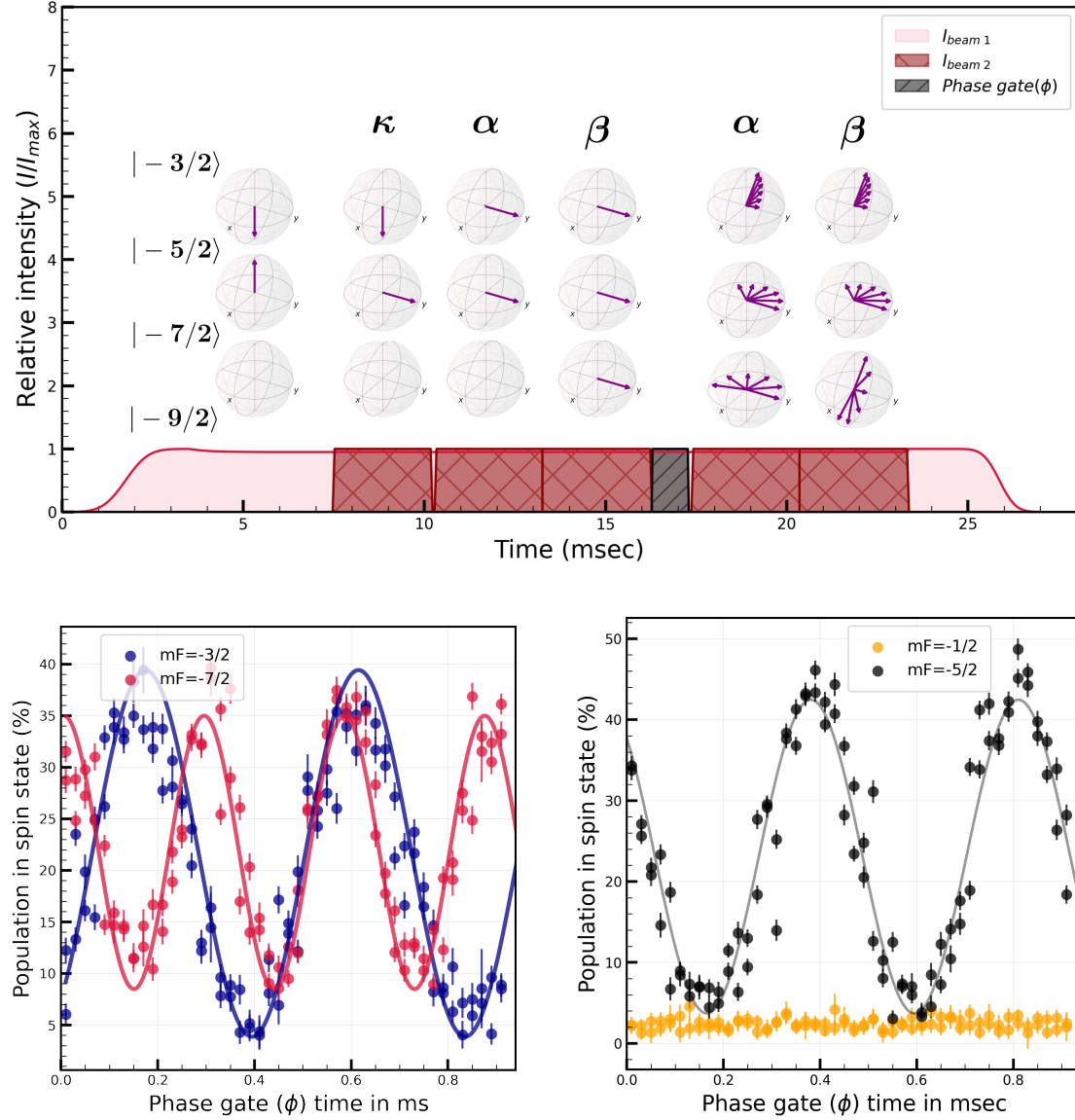
Figure 19: The figure shows the interferometer within the spin states manifold $\{|-3/2\rangle, |-5/2\rangle, |-7/2\rangle, |-9/2\rangle\}$ with καβαβ configuration. For the sequence, the initial spin state is $|-5/2\rangle$. The intensity of the beams {*beam 1*, *beam 2*} is approximately equal to $\{3\ W/cm^2, 0.5\ mW/cm^2\}$ during the sequence. Both the beams have a detuning of -600 MHz from the excited hyperfine state $F = 9/2, ^3P_1$. The intensity of *beam 1* was locked during the experiment at 95 % of maximum intensity. Figure up: shows the intensity profile of both beams during the sequence. The red solid-filled region shows the intensity profile for *beam 1*, and the red hatched region shows the intensity profile for the *beam 2*. The black hatched region shows the region for the phase gate. Notice that the phase gate time is not constant during the experiment. A set of Bloch spheres represents the quantum state for the manifold of four spin states. Figure bottom left: shows the population in the spin states $|-3/2\rangle$ and $|-7/2\rangle$. Blue dots represent the population in the spin state $|-3/2\rangle$, and the red dots represent the population in the spin state $|-7/2\rangle$. Figure bottom right: shows the population in the spin states $|-5/2\rangle$ and $|-1/2\rangle$. Black dots represent the population in the spin state $|-5/2\rangle$, and the orange dots represent the population in the spin state $|-1/2\rangle$.

I discussed in the previous chapter 2 that the energy shift in the ground state manifold consists of light shift that has three components that are quadratic, linear and no dependence on the respective spin states $|mF\rangle$ plus the linear Zeeman shift that has linear dependence on $|mF\rangle$. The light shift plus the Zeeman shift on a spin state $|mF\rangle$ has the form $\Delta E_{m_F} = \alpha^{(q)}m_F^2 + \alpha^{(l)}m_F + \alpha^{(c)}$. Where $\{\alpha^{(q)}, \alpha^{(l)}, \alpha^{(c)}\}$ are the tensor, the vector plus the Zeeman shift and the scalar components of the light shift. It is straightforward to show that the difference of the light shift between the two spin states $|mF+1\rangle - |mF\rangle$ is given by $\Delta E_{m_F+1} - \Delta E_{m_F} = \alpha^{(q)}(2m_F + 1) + \alpha^{(l)}$. Then the difference of light shift between the spin states $|-3/2\rangle - |-5/2\rangle$ is $\Delta E_{-3/2}^{-5/2} = \Delta E_{-3/2} - \Delta E_{-5/2} = -4\alpha^{(q)} + \alpha^{(l)}$ and between the spin states and $|-7/2\rangle - |-9/2\rangle$ is $\Delta E_{-7/2}^{-9/2} = \Delta E_{-7/2} - \Delta E_{-9/2} = -8\alpha^{(q)} + \alpha^{(l)}$. Access to the two simultaneous phases in a double Ramsey interferometer directly gives the values of $\Delta E_{-3/2}^{-5/2}$ and $\Delta E_{-7/2}^{-9/2}$ from which $\alpha^{(q)}$ and $\alpha^{(q)}$ can be simultaneously extracted.

The populations in the figure 19 bottom are fitted with the function $P_{m_F} = A\sin^2(\Omega t/2 + \phi_0) + A_0$ to extract Ω (recall $\Delta\phi_{m_F}^{m_F\pm1} = \Delta E_{m_F}^{m_F\pm1}t/\hbar = \Omega t$). In this equation, A is the amplitude of the fit, A_0 is the offset, Ω is the frequency, and ϕ_0 is the initial phase. The fitting on the bottom left plot gives $\{\Delta E_{-3/2}^{-5/2}, \Delta E_{-7/2}^{-9/2}\}/h = \{2.21 \pm 0.02, 3.43 \pm 0.03\}$ kHz. The fitting on the bottom right plot gives $\Delta E_{-3/2}^{-5/2}/h = 2.31 \pm 0.02$ kHz. For these fittings, I used a reduced chi-square test to assess the goodness of fit of the model to experimental data. It is calculated using the formula $\chi_{red}^2 = \frac{1}{\nu}\sum_{i=1}^{N}\frac{(y_i-f_i)^2}{\sigma_i^2}$. In this formula, y_i represents the experimental data points, f_i represents the model predictions, σ_i represents the uncertainties in the experimental data, and ν denotes the degrees of freedom. Here, ν is the number of data points minus the number of fitted parameters. By examining the value of χ_{red}^2, I determine the quality of the fit such that the model adequately represents the observed data. For the fitting on the spin states $\{|-3/2\rangle, |-5/2\rangle, |-7/2\rangle\}$ reduced chi-squared test gives $\{0.6, 1, 0.5\}$. A χ_{red}^2 value close to 1 confirmes the model and the noise level σ_i. Finally, the two results are resented as the system of linear equations 3.4.8, and the optimal set of coefficients that best fit the data was found using the least square method [Björck, 1996].

$$
\begin{aligned}
\Delta E_{-3/2}^{-5/2} = 2.21 \pm 0.02 \text{ kHz} &= 4\alpha^{(q)} - \alpha^{(l)} \\
\Delta E_{-7/2}^{-9/2} = 3.43 \pm 0.03 \text{ kHz} &= 8\alpha^{(q)} - \alpha^{(l)}
\end{aligned}
\tag{3.4.4}
$$

The solution gives tensor light shift $\alpha^{(q)} = 0.30 \pm 0.01$ kHz and the linear energy splitting $\alpha^{(l)} = -0.99 \pm 0.05$ kHz. The linear energy splitting is the combination of

the vector light shift induced by the *beam 1* and the linear Zeeman shift caused by magnetic field intensity during the time when the *beam 1* is on. The measurement of the magnetic field alone through a resonance spectroscopy during the double Ramsey interferometer sequence gives -0.95 ± 0.05 kHz. We observed that within the error of our measurement the vector light shift created by the *beam 1* is negligible. The polarization of the *beam 1* is maintained such that it only creates the tensor light shifts.
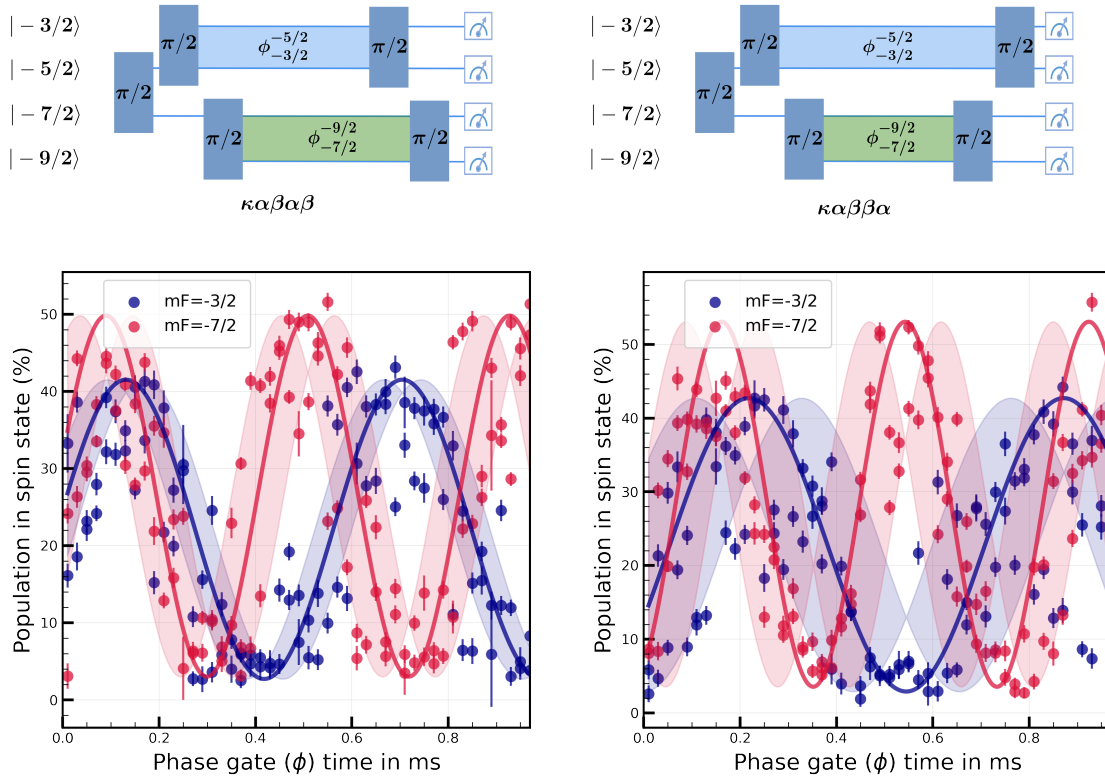

Figure 20: The figure compares the two cases of double Ramsey interferometer $\kappa\alpha\beta\alpha\beta$ and $\kappa\alpha\beta\beta\alpha$. For the sequence, the initial spin state is $|-5/2\rangle$. The intensity of the beams {*beam 1*, *beam 2*} is approximately equal to {3 W/cm^2, 0.9 mW/cm^2} during the sequence. Both the beams have a detuning of -600 MHz from the excited hyperfine state $F = 9/2, ^3P_1$. The intensity of *beam 1* was locked during the experiment at 95 % of maximum intensity. Figures 1: an illustration of the sequence applied during the two cases. The red rectangle connected by the two black solid lines represents $\pi/2$ pulses. The phase difference accumulated is shown only for the states that have to close the $\pi/2$ pulse. Figures below : show the population in the spin states $|-3/2\rangle$ and $|-7/2\rangle$. Blue dots represent the population in the spin state $|-3/2\rangle$, and the red dots represent the population in the spin state $|-7/2\rangle$. The dataset is collected before improving the interferometer's phase noise.

To explore further, I will discuss the symmetry of $\pi/2$ pulses in a double Ramsey interferometer, meaning when the closing pulses of a double Ramsey interferometer are interchanged. Figure 20 compares the two cases of the double Ramsey interferometer sequence $\kappa\alpha\beta\alpha\beta$ and $\kappa\alpha\beta\beta\alpha$, respectively. The data was recorded before the improvement of the phase noise of the interferometer discussed in Section 3.3. The reduced chi-square test gives at least $\chi^{(2)} > 3$ for the fitting on all the populations in the dataset. Hence, direct fitting cannot be used to extract the fitting parameters. It requires a more sophisticated fitting routine to extract the value of Ω.

The process of fitting is as follows, The data points $\{(x_i, y_i)\}_{i=1}^N$ with associated measurement errors in the y-direction are given by the fitting of the images from the experimental sequence, The errors in y-direction represents the total measurement errors. I aim to fit these data points to a sinusoidal model of the form $P_{mF} = a\sin^2(\Omega x + \phi) + a_0$ where Ω, ϕ, a, and a_0 are the parameters to be estimated. First, I perform a curve fit using the standard non-linear least squares method, which minimizes the sum of squared residuals in the y-direction. Let these initial fit parameters be denoted by $\{\bar{\omega}, \bar{\phi}, \bar{a}, \bar{a}_0\}$. Then the residuals in the y-direction are computed as: $r_{y_i} = y_i - \bar{y}_i = y_i - a\sin^2(\frac{\bar{\omega}}{2}x + \phi) + a_0)$. As $\chi^{(2)} > 3$, these y-errors cannot be interpreted as due to the measurement uncertainty. Instead, I assume that they are the consequence of phase noise (effectively x-errors).

To estimate the x-errors Δx_i corresponding to these y-residuals which I interpret as the phase noise of the interferometer, I calculate the gradient of the model with respect to x at each data point given by the equation:

$$\left(\frac{dy}{dx}\right)_i = \frac{\partial}{\partial x}\left(\bar{a}\sin^2\left(\frac{\bar{\omega}}{2}x + \bar{\phi}\right) + \bar{a}_0\right)_{x=x_i} \tag{3.4.5}$$

Given that $\Delta y_i = r_{y_i}$, the corresponding x-errors Δx_i are estimated using error propagation:

$$\Delta x_i \approx \frac{\Delta y_i}{\left(\frac{dy}{dx}\right)_i} = \frac{r_{y_i}}{\left(\frac{dy}{dx}\right)_i} \tag{3.4.6}$$

Here, I assume that the measurement noise on the one data point is small compared to the amplitude of the fringe of the interferometer. The standard deviation of these x-errors provides an estimate of the overall phase noise of the interferometer $\sigma_{\Delta x} = \sqrt{\frac{1}{N-1}\sum_{i=1}^N (\Delta x_i - \overline{\Delta x})^2}$. With the estimated phase noise $\sigma_{\Delta x}$, I apply a

fitting routine called Optimal Distance Regression [Boggs and Rogers, 1990], which minimizes the orthogonal distance between the data points and the model curve, accounting for errors in both the x and y directions. Finally, the ODR process optimizes the parameters $\{\Omega, \phi, a, a_0\}$ by minimizing the following function:

$$\text{ODR Objective:} \quad \min_{\Omega, \phi, a, a_0} \sum_{i=1}^{N} \left(\frac{(y_i - \bar{y}_i)^2}{\sigma_{y_i}^2} + \frac{(x_i - \bar{x}_i)^2}{\sigma_{\Delta x}^2} \right) \tag{3.4.7}$$

where σ_{y_i} and $\sigma_{\Delta x}$ are the standard deviations of the y and x errors respectively. The final parameters $\{Omega, \phi, a, a_0\}$ are extracted from this optimization process, representing the best-fit parameters that account for both x and y uncertainties in the data. Finally, we re-calculate the y-residuals from the ODR fit and re-estimate the x-errors using error propagation, as described earlier. The standard deviation in x-error is the final estimate of the phase noise of the interferometer.

We observe that the population of spin state $|-3/2\rangle$ in the $\kappa\alpha\beta\alpha\beta$ configuration starts with an initial phase $\phi_0 = 0.89 \pm 0.08$ rad at t = 0, while in configuration $\kappa\alpha\beta\beta\alpha$ it starts with an initial phase $\phi_0 = 0.32 \pm 0.08$ rad. When the configuration is changed from $\kappa\alpha\beta\beta\alpha$ to $\kappa\alpha\beta\beta\alpha$, there is an extra phase accumulated for the population in the spin state $|-3/2\rangle$ due to the fact the closing $\pi/2$ pulse for the spin states $|-7/2\rangle \leftrightarrow |-9/2\rangle$ is applied before the spin states $|-3/2\rangle \leftrightarrow |-5/2\rangle$. The phase accumulated during this pulse is given by $\delta\phi = 2\pi\omega t/2$, where t= $T_{-7/2}^{-9/2}(\pi/2)$. Since we know frequency ω for the spin state $|-3/2\rangle$, we can deduce this phase accumulation as -0.54 rad. Therefore, the initial phase in $\kappa\alpha\beta\beta\alpha$ configuration is the sum of the initial phase in $\kappa\alpha\beta\alpha\beta$ configuration plus the extra phase accumulated during $T_{-7/2}^{-9/2}(\pi/2)$. A conclusion is drawn from this analysis that the symmetry of the closing $\pi/2$ pulses does not affect the quality of the light shift measurement but does influence the initial phase of the interferometer. A similar argument holds for the population in the other spin state $|-7/2\rangle$.
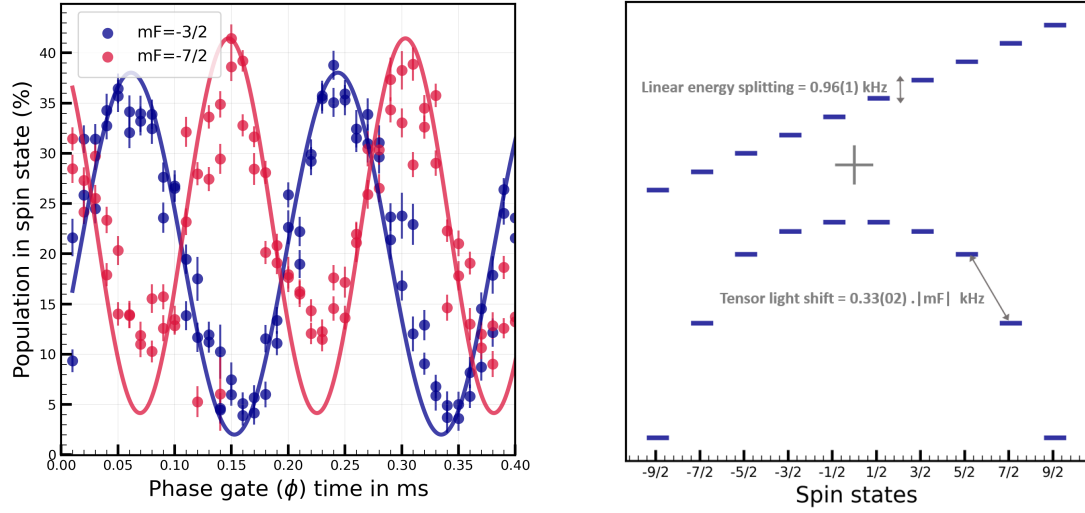
Figure 21: Double Ramsey interferometer within the spin states manifold $\{|-3/2\rangle, |-5/2\rangle, |-7/2\rangle, |-9/2\rangle\}$ with $\kappa\alpha\beta\alpha\beta$ configuration. For the sequence, the initial spin state is $|-5/2\rangle$. The intensity of the beams {*beam 1, beam 2*} is approximately equal to $\{3 \text{ W/cm}^2, 0.5 \text{ mW/cm}^2\}$ during the sequence. Both the beams have a detuning of -600 MHz from the excited hyperfine state $F = 9/2, ^3P_1$. The intensity of *beam 1* was locked during the experiment at 95 % of maximum intensity. $\Delta\omega_{rf}$ is kept 3 kHz for this experiment. Figure left: shows the population in the spin states $|-3/2\rangle$ and $|-7/2\rangle$. Blue dots represent the population in the spin state $|-3/2\rangle$, and the red dots represent the population in the spin state $|-7/2\rangle$. Figure right: shows the tensor light shift and the linear energy splitting within the ground state manifold.

Let's further investigate this interferometer by putting $\Delta\omega_{rf} \neq 0$. The sampling of the data is 10 µs. Figure 21 shows the double Ramsey interferometer with $\Delta\omega_{rf} = 3$ kHz. Now, the phase evolution of both populations $|-3/2\rangle$ and $|-7/2\rangle$ is sensitive to the light shifts plus the difference between the frequencies $\Delta\omega_{rf}$ of the two beams. We observe in figure 21 that the frequencies of the two population dynamics have changed compared to the previous case in figure 19. As expected the frequencies are less distinctive with each other. These frequencies after fitting the both populations are $\{\Delta E_{-3/2}^{-5/2}, \Delta E_{-7/2}^{-9/2}\} = \{5.27 \pm 0.03, 6.58 \pm 0.08\}$ kHz with reduced $\chi^{(2)}$ as $\{0.58, 0.98\}$. The solution involving light shifts and Zeeman shift using these frequencies is given by:

$$\Delta\omega_{-3/2}^{-5/2} - \Delta\omega_{rf} = \Delta E_{-3/2}^{-5/2} = 2.27 \pm 0.03 \text{ kHz} = 4\alpha^{(q)} - \alpha^{(l)}$$
$$\Delta\omega_{-7/2}^{-9/2} - \Delta\omega_{rf} = \Delta E_{-7/2}^{-9/2} = 3.58 \pm 0.08 \text{ kHz} = 8\alpha^{(q)} - \alpha^{(l)}$$

$$(3.4.8)$$

The least squares solution gives tensor light shift $\alpha^{(q)} = 0.33 \pm 0.02$ kHz and the linear energy splitting $\alpha^{(1)} = -0.96 \pm 0.10$ kHz. The result is consistent with the previously obtained result 2. In all, I have demonstrated that we can use the large spin interferometric scheme to measure the tensor light shifts and linear energy splitting. We have understood fully how the phase of the double interferometer evolves with the detuning between the two beams. I now move on to the next section where I shall demonstrate one more application of large spin interferometers.

3.4.2 Simultaneous measurement of two atomic variables through a high dimensional interferometery

High-dimensional interferometers further expand possibilities for quantum sensing by providing access to more than two phases simultaneously. Recently, authors introduced a method to simultaneously measure three orthogonal spin directions in a spinor Bose-Einstein condensate of ^{87}Rb by coupling the system to auxiliary hyperfine states and applying unitary transformations [Kunkel et al., 2019]. This approach allows them to access the spatial spin structure. Such schemes enable direct observation of quantum correlations without state tomography.

Similar to this concept, we propose a scheme to measure two atomic observables, whether commuting or noncommuting, using an interferometer encoded in a qudit (four spin states) of nuclear spins in the ground state manifold of ^{87}Sr. By employing a series of controlled unitary operations, our method enables the simultaneous measurement of these observables. Consequently, this scheme is useful for probing quantum correlations in ultracold atomic systems. For instance, if the populations in the several spin states are measured simultaneously, it can provide the correlations between the measured observables on top of their average value. We start by learning about the theoretical description of the scheme before going to the experimental methodology and discussing the potential applications.

Simultaneously measuring two orthogonal collective spin projections

Consider an arbitrary qubit of one atom in the Hilbert space $\{|0\rangle, |1\rangle\}$ given by $|\psi\rangle = \alpha|0\rangle + \beta exp(i\phi_1)|1\rangle$, where α and β are the probability amplitude for their respective state and ϕ_1 is the phase difference between the two states. For simplicity of my discussion, I will assume $\alpha, \beta = \frac{1}{\sqrt{2}}$ such that the state is given by $|\psi\rangle = \frac{1}{\sqrt{2}}(|0\rangle + exp(i\phi_1)|1\rangle)$. It is then straightforward to show that the measurement of spin operators $\hat{S}_x, \hat{S}_y, \hat{S}_z$ on ψ has expectation values given by $\langle\hat{S}_x\rangle = \frac{1}{2}cos(\phi_1)$,

$\langle \hat{S}_y \rangle = \frac{1}{2}\sin(\phi_1)$ and $\langle \hat{S}_z \rangle = 0$ with $\hbar = 1$. Here, the operators are defined by $\hat{S}_i = \frac{\hbar}{2}\sigma_{i\in(x,y,z)}$ where σ_i are the Pauli spin matrices for two-dimensional Hilbert space associated with the qubit state. The discussion in this sub-section aims to measure the expectation values of at least two of these operators simultaneously. For this, I start by considering a one-atom operator given by:

$$\hat{S}_\phi = \hat{R}_z^\dagger(\phi) \, \hat{R}_y^\dagger(\pi/2) \, \hat{S}_z \, \hat{R}_y(\pi/2) \, \hat{R}_z(\phi) \tag{3.4.9}$$

measuring $\hat{S}_\phi$ is analogous to measuring $\hat{S}_z$ in the basis of qubit state after a sequence of unitary rotation operators such as $\hat{R}_z(\phi)$, which is the rotation ϕ along the z-axis and $\hat{R}_y(\pi/2)$, which is the rotation $\pi/2$ along the y-axis on the state $|\psi\rangle$. The expectation value of $\hat{S}_\phi$ on the state $|\psi\rangle$ is given by $\langle \hat{S}_\phi \rangle = -\frac{1}{2}\cos(\phi + \phi_1)$, which can be written in terms of $\langle \hat{S}_x \rangle$ and $\langle \hat{S}_y \rangle$ as follows:

$$\langle \hat{S}_\phi \rangle = \langle \hat{S}_y \rangle \sin(\phi) - \langle \hat{S}_x \rangle \cos(\phi) \tag{3.4.10}$$

Therefore, it measures the linear combination of the spin operators $\hat{S}_x$ and $\hat{S}_y$. It is to be noted that the phase ϕ is the phase accumulation during this unitary rotation operation while the phase ϕ_1 is the phase difference between the two states initially. Moving on, I will now describe our measurement scheme based on this operator $\hat{S}_\phi$.

Consider all the atoms initially prepared in the spin state $|-5/2\rangle$ state, with a total population of N atoms. We apply a first $\pi/2$ pulse to create a qubit state between the spin states $|-5/2\rangle$ and $|-7/2\rangle$. Here, I assume that $\pi/2$ pulses are perfect, and on average, they distribute the population equally between the addressed spin states. As a general case, one can show that after a $\pi/2$ pulse, the population in each spin state is given by $P_{mF} = N\cos^2(\theta/2)$ and $P_{mF\pm 1} = N\sin^2(\theta/2)$ if we start in the spin state $|mF\rangle$. For a given θ, the sum of the populations is always equal to N. Let's consider the state between the spin states $|-5/2\rangle$ and $|-7/2\rangle$ as two-spinor state $|\psi\rangle = \frac{1}{\sqrt{2}}(|-5/2\rangle + \exp(i\phi_1)|-7/2\rangle)$ whose corresponding orthogonal spin projections $\hat{S}_x, \hat{S}_y$ and $\hat{S}_z$ have to be determined.

The measurement scheme proceeds as follows, the population of the spin state $|-5/2\rangle$ is mapped onto the spin state $|-3/2\rangle$ through a second $\pi/2$ pulse which is defined by a unitary operator $\hat{R}_1(\pi/2)$, similarly population of the spin state $|-7/2\rangle$ is mapped onto the spin state $|-9/2\rangle$ by third $\pi/2$ pulse which is defined by a unitary operator $\hat{R}_2(\pi/2)$. As a result, given the state $|\psi\rangle$ we initially prepared, each spin state

has N/4 atoms on average. In this Hilbert space $\{|-3/2\rangle, |-5/2\rangle, |-7/2\rangle, |-9/2\rangle\}$, the operator $\hat{R}_1(\pi/2)$ and $\hat{R}_2(\pi/2)$ are given by the matrices:

$$\hat{R}_1\left(\frac{\pi}{2}\right) = \begin{bmatrix} \frac{1}{\sqrt{2}} & -\frac{1}{\sqrt{2}} & 0 & 0 \\ \frac{1}{\sqrt{2}} & \frac{1}{\sqrt{2}} & 0 & 0 \\ 0 & 0 & 1 & 0 \\ 0 & 0 & 0 & 1 \end{bmatrix} \tag{3.4.11}$$

and

$$\hat{R}_2\left(\frac{\pi}{2}\right) = \begin{bmatrix} 1 & 0 & 0 & 0 \\ 0 & 1 & 0 & 0 \\ 0 & 0 & \frac{1}{\sqrt{2}} & -\frac{1}{\sqrt{2}} \\ 0 & 0 & \frac{1}{\sqrt{2}} & \frac{1}{\sqrt{2}} \end{bmatrix} \tag{3.4.12}$$

It is to be noted that after the third $\pi/2$ pulse, the spin states $|-3/2\rangle$ and $|-9/2\rangle$ are not exposed to any operations throughout the scheme. Therefore, measuring the population difference of the spin state $|-3/2\rangle$ and $|-9/2\rangle$ is on average equivalent to measuring the population difference of the spin state $|-5/2\rangle$ and $|-7/2\rangle$ which is equal to measuring the expectation value of operator $\langle\hat{S}_z\rangle$ on the qubit state $|\psi\rangle$ meaning:

$$\langle\psi|P_{-3/2} - P_{-9/2}|\psi\rangle = \frac{1}{2}\langle\psi|\hat{S}_z^{(-5/2,-7/2)}|\psi\rangle \tag{3.4.13}$$

where P_{mF} is the probability of being in the spin state $|mF\rangle$. This implies that, we can measure the average value of a many body spin operator $\hat{O}_z$ associated with the qubit state $|-5/2\rangle \leftrightarrow |-7/2\rangle$ by measuring the population in spin states $|-3/2\rangle \leftrightarrow |-9/2\rangle$. The many body (total) spin operator for N number of atoms $\hat{O}_z$ is given by:

$$\hat{O}_z = \sum_{i=1}^{N} \hat{S}_{z,i}^{(-5/2,-7/2)} = \frac{N}{2}\hat{S}_z^{(-5/2,-7/2)} \tag{3.4.14}$$

Here, we assume that the atoms are uncorrelated and alike, and the quantum state of the entire system can be described as a direct product of the individual quantum states of each atom. Therefore, measuring $\hat{O}_z$ effectively means measuring $\hat{S}_{z,i}$ on the i'th atom without applying any transformation on all the other atoms except the identity transformation. The expectation value of the total spin operator $\hat{O}_z$ is given by:

$$\langle \hat{O}_z \rangle = \frac{N}{2} \langle \hat{S}_z^{(-5/2,-7/2)} \rangle = (N_{-3/2} - N_{-9/2}) \tag{3.4.15}$$

where N_{mF} is the number of atoms (expectation value) in the spin state $|mF\rangle$. The prefactor is $N/2$ because there are total $N/2$ atoms in the spin state $|-3/2\rangle$ and $|-9/2\rangle$. By measuring the population in these states we can determine the expectation value of $\hat{S}_z$ operator associated with the intended qubit state $|\psi\rangle$.

After the third $\pi/2$ pulse, a unitary operation given by $\hat{R}_z(\phi)$ is applied. Finally, to close the measurement sequence, a fourth $\pi/2$ pulse is applied between the spin states $|-5/2\rangle \leftrightarrow |-7/2\rangle$ which is given by a unitary operation $\hat{R}_y(\pi/2)$. It is to be noted since the closing $\pi/2$ pulse is between the spin states $|-5/2\rangle \leftrightarrow |-7/2\rangle$ only, we measure only the phase difference accumulated between these two spin states. The matrices $\hat{R}_z(\phi)$ and $\hat{R}_y(\pi/2)$ are given by:

$$\hat{R}_z(\phi) = \begin{bmatrix} 1 & 0 & 0 & 0 \\ 0 & \exp\left(-i\frac{\phi}{2}\right) & 0 & 0 \\ 0 & 0 & \exp\left(i\frac{\phi}{2}\right) & 0 \\ 0 & 0 & 0 & 1 \end{bmatrix} \tag{3.4.16}$$

and

$$\hat{R}_y\left(\frac{\pi}{2}\right) = \begin{bmatrix} 1 & 0 & 0 & 0 \\ 0 & \frac{1}{\sqrt{2}} & -\frac{1}{\sqrt{2}} & 0 \\ 0 & \frac{1}{\sqrt{2}} & \frac{1}{\sqrt{2}} & 0 \\ 0 & 0 & 0 & 1 \end{bmatrix} \tag{3.4.17}$$

The populations in the $|-5/2\rangle$ and $|-7/2\rangle$ are measured after the fourth $\pi/2$ pulse. This measurement is defined on the basis of a many body operator $\hat{O}_\phi$ given by:

$$\hat{O}_\phi = \sum_{i=1}^{N} \hat{J}_{\phi,i}^{(-5/2,-7/2)} = \frac{N}{2}\hat{J}_\phi^{(-5/2,-7/2)} \tag{3.4.18}$$

where the one atom operator $\hat{J}_\phi$ is given by:

$$\hat{J}_\phi^{(-5/2,-7/2)} = \hat{R}_1^\dagger(\pi/2)\,\hat{R}_2^\dagger(\pi/2)\,\hat{S}_\phi^{(-5/2,-7/2)}\,\hat{R}_2(\pi/2)\,\hat{R}_1(\pi/2) \tag{3.4.19}$$

This operator effectively measures the operator $\hat{S}_\phi$ after the unitary transformations $\hat{R}_1(\pi/2)$ and $\hat{R}_2(\pi/2)$. The expectation value of the operator $\hat{O}_\phi$ on the qubit state is given by $\langle\hat{O}_\phi\rangle = -\frac{N}{8}(\cos(\phi + \phi_1))$ which can be further written in terms of expectation value of operator $\hat{S}_\phi$ as follows:

$$\langle\hat{O}_\phi\rangle = \frac{N}{2}\langle\hat{S}_\phi^{(-5/2,-7/2)}\rangle = (N_{-5/2} - N_{-7/2}) \tag{3.4.20}$$

Which implies measuring the N body operator $\hat{O}_\phi$ measures the linear combination of expectation values of operators $\langle\hat{S}_x\rangle$ and $\langle\hat{S}_y\rangle$. Furthermore, we can show that the variance on the measurement of the operator $\hat{O}_\phi$ is given by:

$$Var(\hat{O}_{\phi,z}) = \frac{N}{4} + Var(\hat{S}_{\phi,z}^{-5/2,-7/2}) \tag{3.4.21}$$

Here, $N/4$ comes from the fact that there are total $N/2$ atoms in the spin states $|-5/2\rangle$ and $|-7/2\rangle$. In our measurement scheme, we measure simultaneously the expectation values of $\langle\hat{O}_\phi\rangle$ and $\langle\hat{O}_z\rangle$ because of the access to the population in the spin states that differ by $\Delta mF = 2$. The populations can either be $|-3/2\rangle \leftrightarrow |-7/2\rangle$ or $|-5/2\rangle \leftrightarrow |-9/2\rangle$. We can demonstrate that the two operators do indeed commute with each other:

$$[\hat{O}_\phi, \hat{O}_z] = 0 \tag{3.4.22}$$

This explains access to measuring the spin operators $\langle\hat{S}_\phi\rangle$ and $\langle\hat{S}_z\rangle$ associated with the probed qubit state simultaneously. However, as a consequence, the variance in the

measurement of $Var(\hat{O}_\phi)$ is always higher than the variance in measuring $Var(\hat{S}_\phi)$ given by 3.4.21. In conclusion, we can measure the average value of observable $\langle\hat{O}_\phi\rangle$ and $\langle\hat{O}_z\rangle$ simultaneously with increased variance compared to measuring the average value of observables $\hat{S}_x$, $\hat{S}_y$ and $\hat{S}_z$ independently. This concludes our description of the measurement scheme. Now, we will proceed to the experimental results.

Experimental outcomes

We prepare a spin-polarized gas in the spin state $|-5/2\rangle$. At the beginning of the experiment, after tuning on the *beam 1*, its intensity is locked as described in the earlier experiments. A $\pi/2$ pulse is applied by turning on the *beam 2* for 3.28 ms with a square pulse between the spin states $|-5/2\rangle \leftrightarrow |-7/2\rangle$. Following the first $\pi/2$ pulse, the atoms are in a superposition of the spin states $|-5/2\rangle \leftrightarrow |-7/2\rangle$, with roughly 50 % population per spin state. This concludes the preparation of the initial state $|\psi\rangle$, on which we will now apply the two-observable measurement scheme. A second $\pi/2$ pulse is applied for 3.56 ms between the spin states $|-5/2\rangle \leftrightarrow |-3/2\rangle$. The first and second $\pi/2$ pulses are separated by a 100 μs gap, as with other interferometers previously mentioned. Immediately after the second $\pi/2$ pulse, the third $\pi/2$ pulse is applied for 3.62 ms between the spin states $|-7/2\rangle \leftrightarrow |-9/2\rangle$. Overall sequence of three $\pi/2$ pulses creates the superposition of atoms within the manifold of spin states $\{|-3/2\rangle, |-5/2\rangle, |-7/2\rangle, |-9/2\rangle\}$ with approximately equal population per spin state that is 25 % of the initial population. A phase gate for 500 μs is applied immediately after the third $\pi/2$ pulse. After a gap of 100 μs, the fourth $\pi/2$ pulse is applied for 3.28 ms to close the interferometer between the spin states $|-5/2\rangle \leftrightarrow |-7/2\rangle$.

The first $\pi/2$ pulse creates the qubit between the spin states $|-5/2\rangle \leftrightarrow |-7/2\rangle$. The expectation value of spin projectors $\hat{S}_z$ and $\hat{S}_\phi$ need to be estimated. The unitary evolution of the quantum state with experimental parameters is given by the equation 3.4.23, where the Hamiltonians $\hat{\mathcal{H}}_j$ are described here 3.4.3 and 3.4.2.

$$|\psi(t)\rangle = \hat{U}_\mu(T_{-5/2}^{-7/2})\ \hat{U}_\nu(\tau)\ \hat{U}_\mu(T_{-7/2}^{-9/2})\ \hat{U}_\mu(T_{-3/2}^{-5/2})\ \hat{U}_\mu(T_{-5/2}^{-7/2})|-5/2\rangle$$
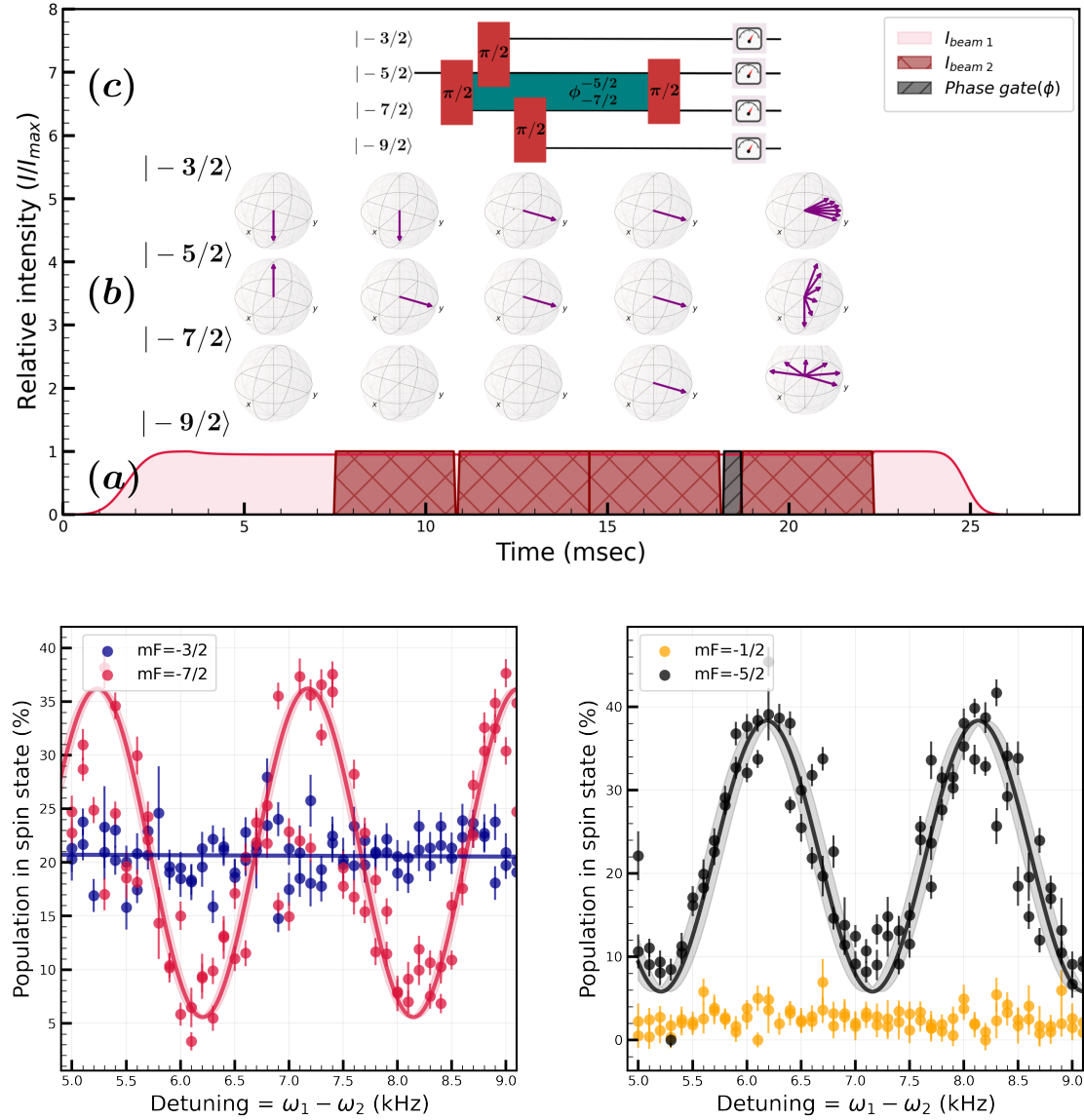$$\text{where,}\quad \hat{U}_{j\in\{\mu,\nu\}} = \exp\left(-i\hat{\mathcal{H}}_j t/\hbar\right) \tag{3.4.23}$$

Figure 22: The figure shows the four pulse interferometer within the spin states manifold $\{|-3/2\rangle, |-5/2\rangle, |-7/2\rangle, |-9/2\rangle\}$. For the sequence, the initial spin state is $|-5/2\rangle$. The intensity of the beams $\{beam\ 1, beam\ 2\}$ is approximately equal to $\{3\ \text{W/cm}^2\}, 0.5\ \text{mW/cm}^2\}\}$ during the sequence. Both the beams have a detuning of -600 MHz from the excited hyperfine state $F = 9/2, ^3P_1$. The intensity of *beam 1* was locked during the experiment at 95 % of maximum intensity. Figure up (a): shows the intensity profile of both beams during the sequence. The red solid-filled region shows the intensity profile for *beam 1*, and the red hatched region shows the intensity profile for the *beam 2*. The black hatched region shows the region for the phase gate. Figure up (b): shows a set of Bloch spheres represents the quantum state for the manifold of four spin states. Figure up (c): shows a circuit representing the $\pi/2$ pulses sequence. Figure bottom left: shows the population in the spin states $|-3/2\rangle$ and $|-7/2\rangle$. Blue dots represent the population in the spin state $|-3/2\rangle$, and the red dots represent the population in the spin state $|-7/2\rangle$. Figure bottom right: shows the population in the spin states $|-5/2\rangle$ and $|-1/2\rangle$. Black dots represent the population in the spin state $|-5/2\rangle$, and the orange dots represent the population in the spin state $|-1/2\rangle$.

Figure 22 shows the experimental data for the interferometric scheme. Figure on top explains the experimental sequence of the interferometery. Figure (a) shows the intensity profile for *beam 1* and *beam 2* during the experiment and the phase gate profile. Figure (b) shows the evolution of the quantum state after each $\pi/2$ pulse of the sequence with the help of a set of three Bloch spheres. Figure (c) represents the equivalent circuit for the applied sequence. Here, the phase accumulated is from the beginning of the first $\pi/2$ pulse to the end of the last $\pi/2$ pulse. The figure at the bottom shows the experimental data collected from the experiment. The color scheme for the different spin states is consistent with the one used throughout the chapter. We notice that in the bottom left plot, the population in the spin state $|-7/2\rangle$ oscillates, while the population in the spin state $|-3/2\rangle$ remains constant, considering measurement noise of the interferometer. In the figure bottom right, the population in the spin state $|-5/2\rangle$ oscillates and the population in the spin state $|-1/2\rangle$ is zero within the measurement noise.

Using the fitting function $P_{mf} = a\sin^2(2\pi\omega + \phi) + a_0$, the ODR (Orthogonal Distance Regression) fitting routine mentioned in the previous section is applied to the experimental data in the spin states $|-5/2\rangle$ and $|-7/2\rangle$ and the optimized parameters $\{\omega, \phi, a, a_0\}$ are extracted. On these populations, the respective phase noise is represented by the error bands. The population in the spin state $|-3/2\rangle$ is fitted with line $P_{-3/2} = mx + c$, where m is the slope of the line and c is the offset. The experimental data's vertical error bars on both of these curves shows the measurement noise.

The population difference between the spin state $|-3/2\rangle$ and $|-9/2\rangle$ gives the average value of the operator $\hat{O}_z$. Here, the population in the spin state $|-9/2\rangle$ is not measured but expected to be equal to the average population in the spin state $|-3/2\rangle$ assuming the first $\pi/2$ pulse is perfect. To measure the fluctuations in the measurement of the operator $\hat{O}_z$ both population needs to be measured simultaneously. The population difference between the spin states $|-5/2\rangle$ and $|-7/2\rangle$ gives the expectation value of the operator $\hat{O}_\phi$. In our current scheme, these populations are measured one after the other run of the experiment. Hence, we can only measures the average value of $\hat{O}_\phi$.
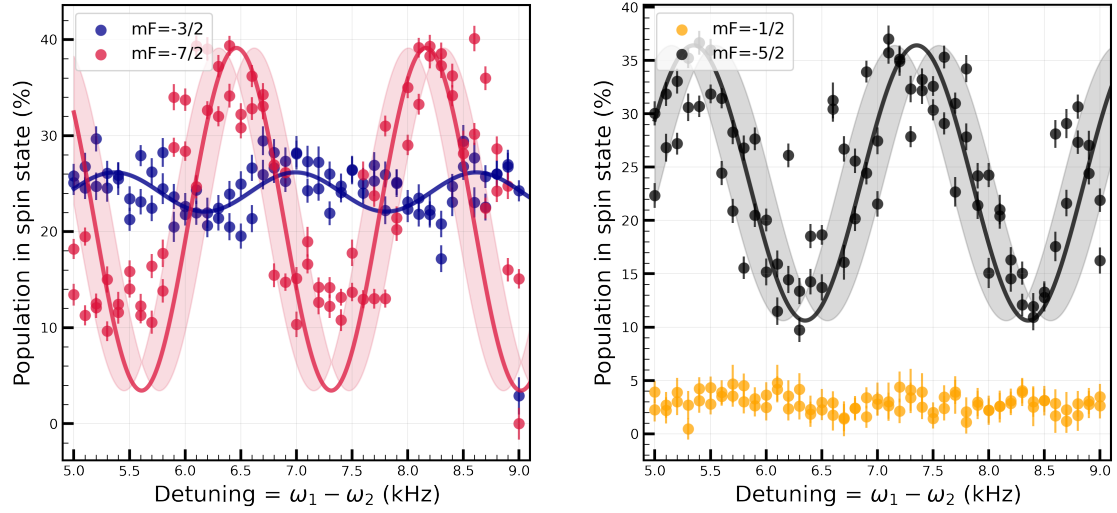
Figure 23: The figure shows the four pulse interferometer within the same manifold as shown in previous figure. The intensity of the beams {*beam 1*, *beam 2*} is approximately equal to {2 W/cm^2, 1.5 mW/cm^2} during the sequence, which leads to higher intensity ratio $\frac{I_2}{I_1}$. Figure left: shows the population in the spin states $|-3/2\rangle$ and $|-7/2\rangle$. Figure right: shows the population in the spin states $|-5/2\rangle$ and $|-1/2\rangle$.

Figure 23 shows the experimental output of another set of data where the ratio of the Rabi couplings Ω_2/Ω_1 is sufficiently larger such that we cannot isolate the two spin state system. The data is taken before the improvement in the phase noise. In this case, the $\pi/2$ pulses are not perfect, leading to the leakage of the population from one spin state to the neighboring spin state. As a consequence, we see the reduction in the contrast in the population of spin state $|-5/2\rangle$ by nearly 20% compared to the figure 22. Furthermore, we observe the oscillations in the population in the spin state $|-3/2\rangle$ because of the leakage of the population from the neighboring spin state $|-5/2\rangle$ to the spin state $|-3/2\rangle$. The 20% reduction in contrast in the spin state $|-5/2\rangle$ may appears as an oscillation in the spin state $|-3/2\rangle$. However, the oscillation in spin state $|-5/2\rangle$ can be removed by the post data analysis (in order to extract $\hat{O}_z$), giving the same quality of results in figure 22 but with reduced contrast.

In this section, we have now covered the theoretical description and the experimental results. I have shown that the average of the two observables $\langle\hat{O}_\phi\rangle$ and $\langle\hat{O}_z\rangle$ can be deduced from the figure 22 left. It would be much better to measure the variance in the observable $\langle\hat{O}_\phi\rangle$, we must measure the population in the spin states $|-5/2\rangle \leftrightarrow |-7/2\rangle$ simultaneously. One way to accomplish this is by defining a qubit state between the spin states $|-3/2\rangle \leftrightarrow |-7/2\rangle$ in the $\sigma - \sigma$ configuration. Then,

with the help of two $\pi - \sigma$ pulses mapping the population within the Hilbert space $\{|-3/2\rangle, |-5/2\rangle, |-7/2\rangle, |-9/2\rangle\}$. The initial qubit state is now defined by the spin states with $\Delta mF = 2$. As a result, we could now measure both populations simultaneously using the current measurement protocol.

3.5 MEASUREMENT PRECISION ON THE INTERFEROMETER

Consider the figure right 24, which represents the population of the atoms in the spin states $|-3/2\rangle$ after a series of three $\pi/2$ pulses with the initial spin state $|-5/2\rangle$. This situation is same as doing an interferometry within four spin states without closing $\pi/2$ pulses. The average of relative uncertainties on the measurement of one data point is given by $\Delta P = \frac{1}{n} \sum_{i=1}^{n} \frac{\sigma_i}{P_i}$ where P_i is the population of the i'th point and σ_i is the standard deviation associated with it. In this figure, one data point is extracted from one picture and fitted by a sum of three Gaussians to extract the populations. The population representing the spin state $|-3/2\rangle$ is the diffracted population in one of the Gaussian, see [Bataille et al., 2020]. The measurement gives the average relative uncertainty as 0.01. In this subsection, I will highlight potential sources, both fundamental and technical, to assess the measurement noise in the experiment.
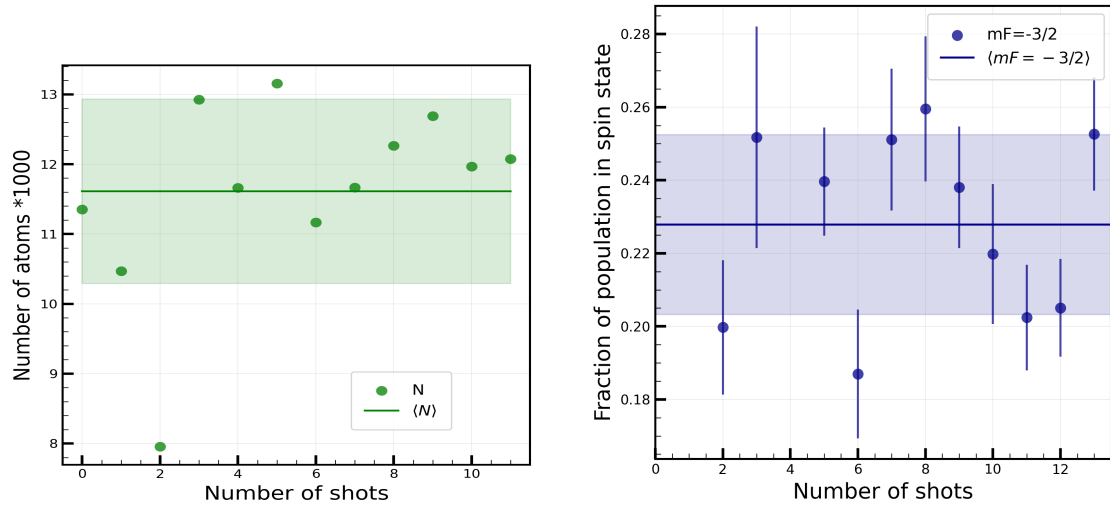

Figure 24: Figure left: fluctuations in the total number of atoms in the polarised Fermi gas at the end of each experimental cycle. Figure right: Measurement noise for the population in the spin state $|-3/2\rangle$ after the series of three $\pi/2$ pulses as $|-5/2\rangle \leftrightarrow |-7/2\rangle$, $|-3/2\rangle \leftrightarrow |-5/2\rangle$ and $|-7/2\rangle \leftrightarrow |-9/2\rangle$. The error bar represents the measurement error per shot. In both the figure, the solid line is the mean value of the population and the color band represents the standard deviation on it.

Atomic shot noise

We start the interferometric experiment with N independent atoms. In our scheme, after performing the first three $\pi/2$ pulses the atoms are in superposition of four spin states. Let the probability of measuring the atoms in the spin state i be given by P_i. Then, the average number of atoms $\langle N_i \rangle$ in the i'th spin state is given by NP_i (if our experimental sequence is perfectly reproducible) with the variance $\sigma^2_{N_i} = Np_i(1-p_i)$, which quantifies the fluctuations in the measured atom number due to quantum projection noise (QPN). The QPN contribution to the noise per spin state is given by:

$$N_{QPN} = \sqrt{\frac{p_i(1-p_i)}{N}} \tag{3.5.1}$$

We typically started with the initial number of atoms N=12000 in a polarized Fermi gas for the data shown for the high dimensional interferometer in this chapter, see figure left 24. Assuming perfect $\pi/2$ pulses implies an equal distribution of atoms $N/4 = 3000$ in each spin state. Then the QPN contribution on the fraction of atoms in one state is approximately 0.0043.

Photon shot noise

In our experiment, each pixel of the camera receives approximately 40000 photons during the exposure time. The camera has maximum detection limit approximately 50,000 photons per pixel. Therefore the relative Photon shot noise, which follows a Poisson distribution is given by:

$$\frac{\sigma_{photon}}{N} = \frac{\sqrt{N}}{N} = \frac{200}{40000} = 0.005 \tag{3.5.2}$$

The uncertainty in optical density (OD) in absorption imaging is affected by photon shot noise. The uncertainty in optical density (OD) is calculated by taking two images: one with atoms and one without (background). We can define OD as the logarithmic ratio of light intensity without atoms to the intensity with atoms. Since both images have around 40000 photons each, the uncertainty in the OD comes from the photon shot noise in both images. The total OD uncertainty is the quadratic sum of the relative fluctuations in both images and becomes 0.0071.

However, we experimentally observed the OD standard deviation 1.5 times larger than the theoretically calculated value of 0.0071. This observation indicates that photon shot noise contributes to the overall noise in optical detection (OD), and other factors like camera setup imperfections and diffraction fringes also have an impact. Nonetheless, the overall uncertainty in OD remains relatively close to the photon shot noise limit but is not fully constrained by it.

Camera read noise

The read noise for the PCO Panda camera is 2.3 electrons. The signal consists of 40000 photons per pixel, taking into account the calibration of quantum efficiency. Then the read noise can be calculated by the ratio $\frac{2.3}{40000} = 0.0000575$. The relative contribution of the read noise to the total measurement noise is extremely small compared to other noises. In practical terms, the read noise is insignificant compared to the magnitude of the photon signal and does not contribute significantly to the measurement noise on our experimental data.

In conclusion, our uncertainty in estimating the diffracted fraction of the population in one particular shot is 0.010, which is approximately 2.3 times bigger than the expected atomic shot noise of 0.0043. The contribution to the overall uncertainty comes from the photon shot noise 0.007 and technical noise. We are experiencing a technical limitation where the observed photon shot noise is 1.5 times larger than expected. This discrepancy may result from occasional diffraction fringes in the images or camera setup imperfections. We should be able to approach the standard quantum limit in the future by improving the camera setup defects and occasional image fringes. Finally, the camera's read noise is negligible and does not significantly impact the measurement noise.

4 | PROBING SU(N) SYMMETRIC INTERACTIONS IN A ULTRACOLD FERMI GAS OF ^{87}Sr

nternal symmetries are fundamental in physics and often correspond to conserved quantities through principles like Noether's theorem. Noether's theorem states that any continuous symmetry of a physical system's action results in a conserved quantity. For example, rotational symmetry leads to the conservation of angular momentum. In quantum systems, symmetries can be extended to internal degrees of freedom, such as spin, described by special unitary groups representing spin rotations.

For instance, Electrons in general exhibit SU(2) symmetry due to their intrinsic spin-1/2 nature, with two possible spin states. SU(3) symmetry of hadrons led to the Quark model which describes the origin of the forces that confine the quarks inside baryons and mesons through the exchange of SU(3) gauge bosons known as gluons [Bernabeu, 2020]. Graphene exhibits SU(4) symmetry due to its four-fold degeneracy arising from spin and valley pseudospin degrees of freedom. This symmetry is crucial for understanding its electronic properties and phenomena like the quantum Hall effect [Castro Neto et al., 2009]. As the symmetry grows from SU(2) to SU(N), more phenomena become accessible.

The generalization of SU(2) to SU(N) results in a larger spin symmetry, indicating that all spin states are treated equally under this symmetry. In the presence of SU(N) symmetry, spin-exchange interactions that typically drive spin dynamics are suppressed, resulting in static spin states. This suppression provides a platform for exploring quantum magnetism, as systems with SU(N) symmetry can exhibit exotic magnetic phases, offering insights into many-body quantum behavior and strongly correlated systems. This generalization of the symmetry can be investigated using a perturbative approach through a parameter 1/N where N is the large spin degeneracy N=2F+1 [Affleck and Marston, 1988]. For instance, 1/N expansion of the Kondo lattice problem exhibits how local spin fluctuations are enhanced by large spin degeneracy [Coleman, 1983]. Furthermore, SU(N) symmetry offers a great opportunity to deal with the problems like unconventional quantum magnetism and high TC superconductivity [Marston and Affleck, 1989]. However, in this context, the SU(N) symmetry

is often considered a purely mathematical construct. In contrast, the SU(N) symmetry is naturally present within the nuclear spin degrees of freedom of fermionic AEA. Therefore, it offers an excellent experimental foundation for exploring the basics of particle physics and numerous intriguing issues in condensed matter physics within the laboratory.

For instance, in the ground state $^1S_0$ of ^{87}Sr, electronic degrees of freedom does not have the spin and orbital angular momentum (J=0). The nuclear spin (I=9/2) is thus decoupled from the electronic spin because the hyperfine interactions are absent. The electronic-nuclear spin decoupling imposes the condition that the scattering lengths involving $^1S_0$ state should be independent of the nuclear spins. Under these conditions, the interactions are expected to exhibit SU(N) spin symmetry, where N = 2F+1. In the case of Fermionic ^{87}Sr N=10. For the $^1S_0$ state, it has been theoretically estimated that the relative variation of the scattering length for the various nuclear spin components should be of the order of $\delta a_s/a_s \sim 10^{-9}$ [A. V. Gorshkov et al., 2010]. Spectroscopy using a clock transition $^1S_0 \leftrightarrow ^3P_0$ has been used to investigate SU(N) symmetry of ^{87}Sr. The result observed a SU(N) symmetry breaking to be below 3% [Zhang et al., 2014].

In this chapter, I will present a brief discussion of short-range interactions in ultracold atoms. I conclude that at low temperatures, mean-field interactions dominate the scattering processes. Thus, we investigate the energy shift resulting from these interactions. I will demonstrate our scheme to probe SU(N) symmetry within the ground state $^1S_0$ of ^{87}Sr with the help of a Ramsey interferometer encoded in the nuclear spins. First, I will present our preliminary result of an SU(N) symmetry test in the ground state of $^1S_0$. This experiment involves testing the bulk gas confined in an optical dipole trap. The observed result shows that SU(N) symmetry breaking is below 10^{-2} level. Secondly, to improve our measurement precision, we will increase the density of the gas by applying additional potential in addition to the optical dipole trap. In this result, we only observe SU(N) symmetry breaking to be below 10^{-2} level. However, I set the future guidelines to increase the precision to 10^{-3} level.

4.1 INTERACTIONS IN ULTRACOLD ATOMS WITH INTERNAL DEGREES OF FREEDOM

Consider a gas with n number of interacting particles at a finite temperature. If the temperature is low, collisions are dominated by s-wave scattering. Higher angular

momentum modes, such as p-wave or d-wave, involve centrifugal barriers that require more energy to activate and are therefore suppressed at low temperatures. The s-wave scattering cross-section is given by $\sigma = 4\pi a_s^2$, and the scattering rate is:

$$\Gamma_{\text{scatt}} = n\sigma v = n \cdot 4\pi a_s^2 \cdot v \tag{4.1.1}$$

Where v is the relative velocity between particles, a_s is the s-wave scattering length, and n is the particle density. The Γ_{scatt} define the frequency of the collisions. In addition, in the Fermionic system, the Pauli exclusion principle necessitates antisymmetrization of the total wavefunction. For two identical fermions, the total wavefunction must be antisymmetric under particle exchange:

$$\Psi(\mathbf{r}_1, \mathbf{r}_2) = -\Psi(\mathbf{r}_2, \mathbf{r}_1) \tag{4.1.2}$$

this symmetry implies that for s-wave interactions (symmetric), only antisymmetric spin wavefunctions need to be taken into account (S_{total} = even). Here, S_{total} is the total spin of the interacting particles. Therefore, Fermions in identical internal states do not display interactions because it is impossible to anti-symmetrize the wave function in s-wave scattering. On the other hand, the mean-field interaction energy per particle is given by:

$$E_{\text{mf}} = \frac{4\pi\hbar^2 a_s}{m} n \tag{4.1.3}$$

Where m is the mass of the particle. To define a rate associated with the mean-field interaction, we divide the interaction energy by reduced Planck's constant $\hbar$, yielding the mean-field interaction rate:

$$\Gamma_{\text{mf}} = \frac{E_{\text{mf}}}{\hbar} = \frac{4\pi\hbar a_s}{m} n \tag{4.1.4}$$

This rate defines the characteristic frequency of the interaction due to the collective effect of all particles in the gas. In ultracold gases, Γ_{mf} governs the overall interaction strength in the system, while Γ_{scatt} represents the microscopic collision rate between individual atoms. The ratio of the two rates is given by:

$$\frac{\Gamma_{\text{scatt}}}{\Gamma_{\text{mf}}} = \frac{a_s \cdot \sqrt{3mk_BT}}{\hbar} \tag{4.1.5}$$

where T is the temperature of the gas. I have used relative velocity of atoms as the rms thermal velocity $\sqrt{\frac{3k_BT}{m}}$ at temperature T. For ^{87}Sr the two rates becomes equal at about 111 µK. While at 100 nK which is the usual case in our experiment, The ratio is about 0.03. Therefore, the scattering is suppresssed at this temperature. Hence, we can neglect the scattering at this temperature. I shall continue further discussion on mean field interactions.

Pioneering work by [Huang and C. N. Yang, 1957] shows that complicated interatomic potentials are well approximated by the pseudopotential, which is given by: $V(\mathbf{r}) = \frac{4\pi\hbar^2 a_s}{m}\delta(\mathbf{r})\partial_r(r)$, where $\mathbf{r}$ is the relative separation between the colliding particles. This pseudopotential is applicable to Bosons and spin-1/2 Fermions only. The generalisation of this pseudopotential to spin-F Fermions is done by [Yip and T.-L. Ho, 1999]:

$$\hat{V}(\hat{\mathbf{r}}) = \sum_{\text{even } j=0}^{2F-1} \frac{4\pi\hbar^2 a_s^j}{m}\delta(\hat{\mathbf{r}})\frac{\partial}{\partial r}(r)\,\mathcal{P}_j \tag{4.1.6}$$

where $\mathcal{P}_j$ represents the projector onto states with total spin of a pair of Fermions equal to j = 0, 2,..., 2F-1 because 2F-1 scattering lengths are necessary to characterize the interaction between spin-F fermions. The mean field interaction energy per particle associated with this spin dependent potential can be derived from this spin-dependent potential as:

$$E_{\text{mf}} \propto \sum_{\text{even } j=0}^{2F-1} \frac{4\pi\hbar^2 a_s^j}{m}\int dx\,dy\,dz\,n(x,y,z)^2\,\mathcal{P}_j \tag{4.1.7}$$

If the particles in the spin state $|mF\rangle$ and $|mF'\rangle$ interact through a potential defined by 4.1.6. The spin changing interactions are possible because of the spin dependency of this potential:

$$\langle m_F + \delta, m_{F'} - \delta|\hat{V}(\hat{\mathbf{r}})|m_F, m_{F'}\rangle \neq 0 \tag{4.1.8}$$

Where δ is to make sure that the total spin is conserved during the process. In contrast, if the scattering lengths a_s are spin-independent, the spin exchange interactions vanish. The condition leads to SU(N) symmetry for N possible spin states.

Therefore, the mean-field interaction energy 4.1.7 does not acquire the energy shift for interaction between the different spin channels. We observe that using the generalized pseudopotential simplifies the description of spin-dependent interactions, and the result emerges as the macroscopic observable in terms of energy shift. The linear dependence of the energy shift on $n(x, y, z)$ reflects the collective contributions from collisions within the gas, with each spin channel contributing according to its respective scattering length. This linear energy shift can be probed as a phase shift in a Ramsey interferometer in our scheme. In addition, spin exchange interactions appears as the decaying contrast in the interferometer. Therefore, we can measure both effects (spin exchange and shifts) through contrast and phase in the Ramsey interferometer.

Our experimental scheme for probing the interaction between the nuclear spins in the ground state manifold $^1S_0$ of ^{87}Sr depends upon the interaction of the qubit state between the two spin state $|m_F\rangle \leftrightarrow |m_F + 1\rangle$ with the third spin state $|mF'\rangle$ that we call as impurity state. Qubit interact with the impure spin state and the differential scattering length $\delta a = a_{mF,mF'} - a_{mF \pm 1,mF'}$ translates to the phase of the Ramsey interferometer. Here, $|mF'\rangle$ is the impurity. Asymmetry in the scattering lengths within the nuclear spin states appears as the phase shift $\Delta\phi$ in the interferometer as $\Delta\phi = (\Delta E_{mf}^{mF,mF'} - \Delta E_{mf}^{mF+1,mF'})t/\hbar$ where t is the interaction time of the qubit with the impurity. Note that the $\Delta\phi$ is the phase shift between the fringes of the Ramsey interferometer when the impurity is present or not.

4.2 PROBING SU(N) SYMMETRIC COLLISIONS WITHIN THE NUCLEAR SPINS OF ^{87}Sr

We measure the differential scattering length to probe the SU(N) symmetry in the ground state manifold of ^{87}Sr in the following two cases. The first measurement involves determining the differential scattering length in the bulk Fermi gas within the optical dipole trap (ODT) alone. In the second case, we increased the density of the Fermi gas by activating further confinement using a laser beam used to load the Fermi gas into the 1D optical lattice along gravity.

4.2.1 Measurement in the bulk gas confined in optical dipole trap

Initially, we prepare a polarized Fermi gas in the spin state $|-5/2\rangle$. A $\pi/2$ pulse of 2.37 ms creates a superposition between the spin state $|-5/2\rangle \leftrightarrow |-3/2\rangle$ by distributing approximately half of the initial number of atoms in each spin state. Afterward, the intensity of *beam 1* is ramped down to zero in 2 ms. At this moment, the qubit state precesses to accumulate phase only in the presence of the external magnetic field. To probe this qubit, the intensity of the *beam 1* is ramped up in 2 ms, and a $\pi/2$ pulse of 2.37 ms is applied. The number of atoms in the spin state $|-5/2\rangle$ is measured. The detuning between the two beams is maintained so that the fringe period of the interferometer is approximately 1 ms. I recorded two sets of data, each containing 80 data points with two fringes per dataset. I took various sets of these datasets for different dark periods ranging from 10 ms to 2 s. The interferometer data is collected for two cases. Case one involves probing the bare qubit state $|-5/2\rangle \leftrightarrow |-3/2\rangle$, while case two deals with probing the qubit in the presence of impurity, i.e., the spin state $|-9/2\rangle$. For all datasets, the Ramsey interferometer has a fringe of about 1 ms. Our best measurement of the fringe occurs at 2 s of dark time, allowing us to probe the phase accumulated for 2000 fringes.

4.2.2 Average phase shift due to the mean field interactions

In this sub-section, I aim to calculate the phase shift $\Delta\phi$ in the Ramsey interferometer initiated by the mean-field interactions. In principle, if the ground state manifold has SU(N) symmetry, the phase difference should be zero. To calculate the phase difference, I start by defining an average phase $\bar{\phi}_{mF,mF'}$ as a result of the mean-field interactions between the two spin states $|mF\rangle$ and $|mF'\rangle$ (the phase is the mean-field energy multiplied by the interferometer time and averaged over the atomic cloud). In this phase, $|mF\rangle$ is one of the spin states involved in the Ramsey interferometry, and $|mF'\rangle$ is the spin state for the impurity atoms. To calculate this average phase, I first start by defining the density profile of the gas in a 3D harmonic trap. The density $n_{mF'}(x,y,z)$ of a thermal gas in a three-dimensional (3D) harmonic trap for the spin state $|mF'\rangle$ follows a Maxwell-Boltzmann distribution and is given by:

$$n_{mF'}(x,y,z) = n_{mF'}^0 \exp\left(-\frac{m}{2k_B T}\left(\omega_x^2 x^2 + \omega_y^2 y^2 + \omega_z^2 z^2\right)\right) \tag{4.2.1}$$

Where $n^0_{mF'}$ is the peak density at the center of the trap, m is the atomic mass, ω_x, ω_y, and ω_z are the trap frequencies along the respective axes, k_B is Boltzmann's constant, and T is the temperature of the gas. The gas density is distributed spatially within a finite space. Therefore, the phase associated with the mean-field interactions takes the spatial dependence:

$$\phi(x, y, z) = \frac{4\pi\hbar^2 a_{mF, mF'}}{m} \frac{t}{\hbar} n_{mF'}(x, y, z) \tag{4.2.2}$$

Where t is the interferometer time and $a_{mF, mF'}$ is the scattering length for the interaction between the spin states $|mF'\rangle$ and $|mF\rangle$. Moving on, I define the ratio f such that $f = \frac{n_{mF'}(x,y,z)}{n_{mF}(x,y,z)} = \frac{n^0_{mF'}}{n^0_{mF}}$. This ratio is valid because both the spin species are confined in the same trap and have the same temperature profile. Then, the average phase due to the interaction between the two spin species is given by:

$$\bar{\phi}_{mF, mF'} = \frac{1}{N_{mF}} \int n_{mF}(x, y, z)\, \phi(x, y, z)\, dx\,dy\,dz \tag{4.2.3}$$

$$= \frac{f}{N_{mF}} \frac{4\pi\hbar^2 a_{mF, mF'}}{m} \frac{t}{\hbar} \int n^2_{mF}(x, y, z)\, dx\,dy\,dz \tag{4.2.4}$$

$$= \frac{f}{N_{mF}} \frac{4\pi\hbar^2 a_{mF, mF'}}{m} \frac{t}{\hbar} \frac{(n^0_{mF})^2}{2\sqrt{2}} \frac{N_{mF}}{n^0_{mF}} \tag{4.2.5}$$

$$= \frac{4\pi\hbar^2 a_{mF, mF'}}{m} \frac{t}{\hbar} \frac{n^0_{mF'}}{2\sqrt{2}} \tag{4.2.6}$$

$$\tag{4.2.7}$$

If the two spin states involved in the Ramsey interferometer are $|mF_1\rangle$ and $|mF_2\rangle$, the total phase difference accumulated $\delta\phi$ in the interferometer is given by:

$$\Delta\phi = \bar{\phi}_{mF_1, mF'} - \bar{\phi}_{mF_2, mF'} \tag{4.2.8}$$

$$= \frac{4\pi\hbar^2}{m} \frac{n^0_{mF'}}{2\sqrt{2}} \frac{t}{\hbar} \delta a \tag{4.2.9}$$

Where δa is the differential scattering length $\delta a = a_{mF_1, mF'} - a_{mF_2, mF'}$. After rearranging we get:

$$\delta a = \frac{m}{4\pi\hbar t} \frac{2\sqrt{2}}{n^0_{mF'}} \Delta\phi \tag{4.2.10}$$

and the uncertainty on it:

$$\sigma_{\delta a} = \frac{m}{4\pi\hbar t} \cdot 2\sqrt{2} \cdot \sqrt{\left(\frac{\Delta\phi \cdot \sigma_{n^0_{mF'}}}{(n^0_{mF'})^2}\right)^2 + \left(\frac{\sigma_{\Delta\phi}}{n^0_{mF'}}\right)^2} \tag{4.2.11}$$

This expression assumes that the fluctuations in $\Delta\phi$ and $n^0_{mF'}$ are uncorrelated. We now have the expression for the differential scattering length and the uncertainty on it. For a well-defined interferometer time t, this expression requires the estimation of the peak density $n^0_{mF'}$ and the phase difference $\Delta\phi$ of the interferometer. I move on to the following sub-section to calculate the peak density of the impurity atoms.

4.2.3 Determination of the peak density of the impurity atoms

To calculate the peak density of the impurity atoms, we need to find the total number of atoms. To find the total number of particles $N_{mF'}$, we integrate the density profile over the entire volume $N_{mF'} = \int n_{mF'}(x, y, z) \, dx \, dy \, dz$. The result of the integration is given by:

$$N_{mF'} = n^0_{mF'} \left(\frac{2\pi k_B T}{m}\right)^{3/2} \frac{1}{\omega_x \omega_y \omega_z} \tag{4.2.12}$$

Thus, the peak density $n^0_{mF'}$ of the impurity atoms, considering the mean trap frequency $\bar{\omega}$, is given by:

$$n^0_{mF'} = N_{mF'} \left(\frac{m\bar{\omega}^2}{2\pi k_B T}\right)^{3/2} \tag{4.2.13}$$

where $\bar{\omega}$ is the effective trapping frequency of the optical dipole trap and is the geometric mean of the angular trapping frequencies $\bar{\omega} = \sqrt[3]{\omega_x \omega_y \omega_z}$ along the three directions.

In order to calculate the peak density of impurity atoms, we need to determine the temperature T of the gas and the effective confinement frequency $\bar{\omega}$. The temperature is obtained by analyzing the absorption image of the thermal gas presented in the figure 25 (a). To extract the temperature, a two-dimensional Gaussian function is fitted, as shown in 25 (b). This fitting function is given by:
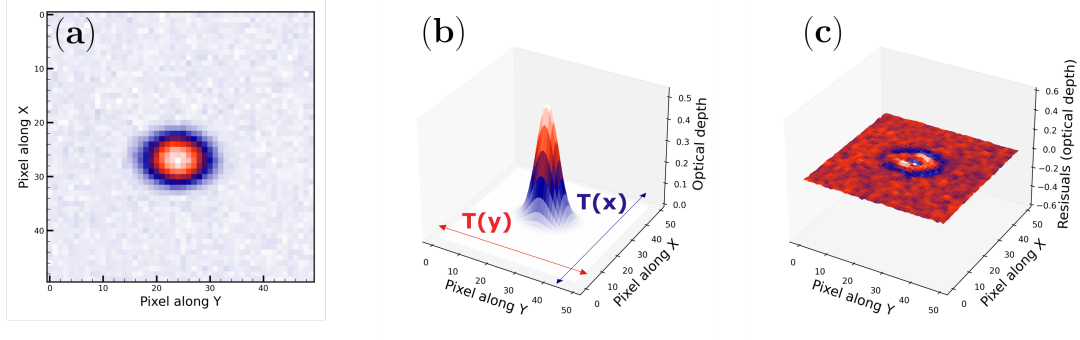
Figure 25: Temperature calculation for the 3D Gaussian gas inside the optical dipole trap's harmonic potential. Figure (a) shows an absorption image in 50 by 50 pixels following a 5-ms time of flight (TOF) experiment. Figure (b) shows a 2D Gaussian fit on the figure (a) to extract T_x and T_y. Figure (c) shows the residuals of the two-dimensional Gaussian fit.

$$I(x, y) = A \left(\exp \left(-\frac{(x - x_0)^2}{2\sigma_x^2} \right) + \exp \left(-\frac{(y - y_0)^2}{2\sigma_y^2} \right) \right) + I_0, \tag{4.2.14}$$

Where A represents the amplitude of the Gaussian, x_0 and y_0 is the center position of the Gaussian peak, σ_x and σ_y are the standard deviation of the Gaussian width along the X and Y direction, and I_0 accounts for any background noise or offset in the image. The widths $\{\sigma_x, \sigma_y\}$ obtained from this fitting procedure is directly related to the temperature of the gas as:

$$\sigma_x \cdot S_{pixel} = \sqrt{\frac{k_B \cdot T_x \cdot \Delta t_{TOF}^2}{m}} \tag{4.2.15}$$

$$\sigma_y \cdot S_{pixel} = \sqrt{\frac{k_B \cdot T_y \cdot \Delta t_{TOF}^2}{m}} \tag{4.2.16}$$

Where m is the mass of the ^{87}Sr atom, k_B is the Boltzmann constant, and Δt_{TOF} is the time-of-flight. Since the width is in pixels, the LHS is multiplied by the size of one pixel S_{pixel}, which is 6.5 μm. With the help of this process, the gas temperature is determined along the two direction as $T_x = 148 \pm 2$ nK and $T_y = 258 \pm 2$ nK. The temperature along the two axis are different because the gas is not thermalized. There-

fore, I make an assumption here to take the geometric mean of the two temperature for further calculation which is $T = \sqrt{T_x T_y} = 195 \pm 3$ nK.

The next step is to determine the number of impurity atoms $N_{-9/2}$ inside the gas. For this, I start by calculating the optical density (OD) of the atomic gas and relate it to the number of atoms N. Consider the direction of the absorption beam along the z-axis. The density profile of the gas is given by the equation 4.2.13. Starting from the Beer-Lambert law $\frac{dI}{I} = -n(x, y, z)\, \sigma\, dz$, we can show that the optical density profile in xy-plane is given by:

$$OD(x, y) = \log(\frac{I_0}{I}) = \sigma \int_{-\infty}^{\infty} n(x, y, z)\, dz \tag{4.2.17}$$

Where I_0 is the initial intensity of the beam, and I is the final intensity after the absorption by a 3D thermal gas with a density profile $n(x, y, z)$. For resonant imaging, $\delta = \omega - \omega_0 << \Gamma$ (here, δ is specifically the detuning between the laser frequency ω to the transition frequency ω_0), the absorption cross-section σ is given by $\sigma = \frac{3\lambda^2}{2\pi}$ with λ being the wavelength of the light used for absorption imaging. The integral of the optical density $OD(x, y)$ over x and y direction leads to:

$$\int_{-\infty}^{\infty} \int_{-\infty}^{\infty} OD(x, y)\, dx\, dy = \sigma\, n_0 \left(\frac{2\pi k_B T}{m}\right)^{3/2} \frac{1}{\omega_x \omega_y \omega_z} = \sigma N \tag{4.2.18}$$

Therefore, we can use the absorption image to determine $OD(x, y)$ and then fit it with a 2D Gaussian along the x-axis and y-axis to directly calculate the area under the curve, thus obtaining the number of atoms in the gas. The process involves fitting the absorption images of a mixture two-spin component gas and a single component gase. In the first case, the image corresponding to a mixture of spin states $|-5/2\rangle$ and $|-9/2\rangle$ is fitted, giving the number of atoms $N_{-5/2} + N_{-9/2}$. The $N_{-5/2}$ is obtained by fitting the single component gas in the $|-5/2\rangle$ spin state. The number of impurity atoms $N_{-9/2}$ in the $|-9/2\rangle$ spin state is then obtained by subtracting the number of atoms in the single component gas from the number of atoms in the mixture of two-component gas. The estimated number of atoms are $N_{-9/2} = 3000 \pm 100$. This number is the average number obtained from fitting of five pictures.

Moving on, the effective trapping frequency $\bar{\omega}$, the geometric mean of the trapping frequencies of ODT in the three spatial directions, is calculated based on calibration by measuring the optical power near the experimental cell. Based on this measurement

and the geometry of the dipole trap, the trapping frequencies along the three orthogonal axes are known. The trapping frequency $\bar{\omega}$ is estimated as $\bar{\omega} = 2\pi 50$ rad/s. Our measurement errors on $\bar{\omega}$ are substantial because the dipole trapping frequencies uncertainties are particularly sensitive to the crossing of the two dipole trap beams at the end stage of evaporation. This can have a significant impact on the trap's geometry; as a result, there are significant uncertainties when determining the trapping frequencies straight from the optical power measurement. Based on our calculations, it can be higher by $2\pi 10$s of rad/s and as low as zero. Here, I will use $\bar{\omega} = 2\pi \times 50$ rad/s for our estimation, considering the high uncertainties on $\bar{\omega}$.

Putting the values of temperature T, trapping frequency $\bar{\omega}$ and number of atoms N, the mean density and the uncertainity associated with it is known $(4.5 \pm 0.2) \times 10^{16}$ m^{-3}. This density is however without taking into account the uncertainty in the $\bar{\omega}$. Considering the uncertainty in our case for $\bar{\omega}$, the density can range from $(7.3 \pm 0.2) \times 10^{16}$ m^{-3}to o. I will proceed with the tentative density $(4.5 \pm 0.2) \times 10^{16}$ m^{-3} for this chapter.

4.2.4 Estimation of the phase difference and the uncertainty associated with it

Figure 26 shows the experimental data for estimating the phase difference. The interferometer data is obtained for the two cases discussed in this section. The figure inset displays data for two cases. The first case is represented by black circles, indicating the absence of impurity atoms $|-9/2\rangle$. The second case is shown with green circles, signifying the presence of impurity atoms $|-9/2\rangle$. We notice that the contrast of the interferometer appears to be lower when impurity atoms $|-9/2\rangle$ are present. The reduction, however, is not the contrast reduction in the Ramsey interferometer fringe but rather because of the change in the ratio of the diffracted cloud to the central cloud. This occurs in our spin-dependent momentum transfer scheme because the central cloud contains $|-9/2\rangle$ atoms. Therefore, the ratio is smaller than that of the case when there are no impurity atoms. This reduction is constant throughout all the datasets.

For extracting the phase in both cases, the population in the spin state $|-5/2\rangle$ is fitted with the function $P_{-5/2} = A\sin(\omega(t-t_0)+\phi)+A_0$ to extract fitting parameters. The function is fitted such that at $t = 0$, ϕ lies on the middle of the slope of the fringe for maximum sensitivity, the middle being approximately at t_0. Then, I applied a resampling technique called Bootstrapping with the help of a Python library [Bradley Efron and Tibshirani, 1993].
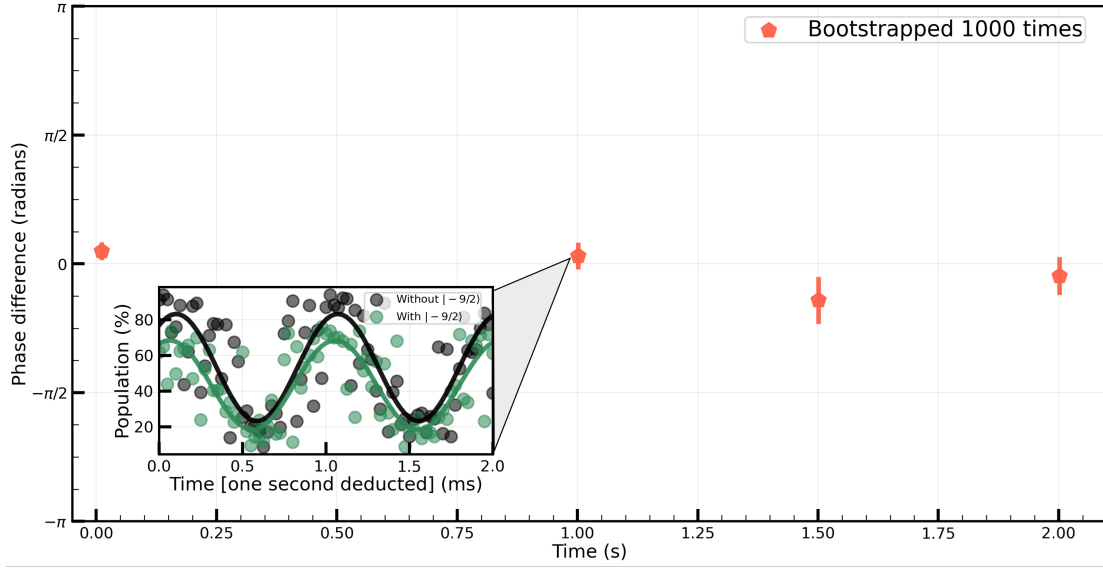
Figure 26: Main figure: phase difference $\Delta\phi$ in radians plotted as a function of dark time. Analyzing a single interferometer data set of 2 ms provided one data point in the figure. The error bars on the data are standard deviations from bootstrapping. Inset figure: Black dots represent the population in the spin state $|-5/2\rangle$ without the presence of the impurity state $|-9/2\rangle$ while the green dots are in the same population but with impurity atoms. The time window for the inset figure is 1000 ms to 1002 ms.

In this process, new datasets (resample) of the same size as the original are generated by randomly selecting data points from the original dataset with replacements. Every resample is used to fit the model and record the estimated parameters for each resample of the bootstrap approach. The mean of these fitted parameters represents the final fitted parameters and the standard deviation of the fitted parameters gives an estimate of the uncertainty. As a non-parametric approach, bootstrapping is adaptable and data-driven since it makes no assumptions about the distribution of the dataset.

After performing the process on both cases, the phase difference is $\Delta\phi = |\phi_1 - \phi_2|$, where ϕ_1 and ϕ_2 are the fitted phase in the two cases. The standard deviation on $\Delta\phi$ is the quadrature sum of the standard deviation of the phase in the two cases. Main figure 26 plots the phase difference and the uncertainty associated with it.

For the interferometer times $\{0.01, 1, 1.5, 2\}$ seconds, the phase difference with the corresponding uncertainty is calculated as $\{0.15 \pm 0.11, 0.10 \pm 0.16, 0.44 \pm 0.29, 0.15 \pm 0.23\}$ radians. I illustrate how these uncertainties are translated to the energy differences in figure 27. The standard deviation in Hz equal to the interferometer time is represented as the grey dashed line in figure representing the linearly growing uncertainty with time. The energy difference in Hz associated with this phase difference is
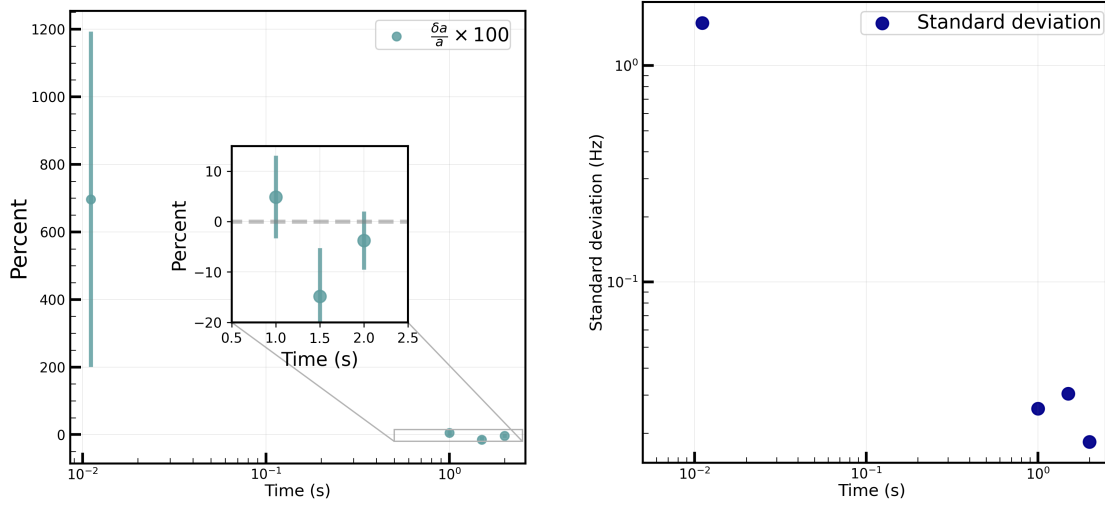
Figure 27: Figure left: estimated relative differential scattering length $\frac{\delta a}{a} \times 100$ plotted as a percentage for different interferometer times. Figure right: standard deviation on the measurement of energy difference in Hz vs the interferometer time. Dark blue dots represent the energy difference. The dashed grey line represents the baseline where the standard deviation equals the interferometer time. Both the figure represents the data for interferometer time $\{0.01, 1, 1.5, 2\}$ s.

given by $\Delta E(Hz) = \frac{\Delta \phi}{2\pi \hbar t}$, where t is the interferometer time. Since the interferometer time is well known, the uncertainty on the energy difference is simply uncertainty on the phase difference divided by the interferometer time. Because of the sub-linear growth of the phase difference uncertainty, the measurement uncertainty of the energy difference reduces with t. The blue dots in the figure represent the energy difference uncertainty for each interferometer time, which is estimated as $\{1.6, 0.03, 0.03, 0.02\}$ Hz. In conclusion, the uncertainty in the energy difference is reduced by two orders of magnitude when the interferometer time is increased by two orders of magnitude. In all, I report that we can probe an energy difference of the order of 10^{-2} Hz (precisely 0.02 Hz) at an interferometer time of 2 seconds.

The parameters needed to determine the differential scattering length and its related uncertainty have been obtained in this subsection. Plugging the values of the average density of the cloud and the phase difference in the equations 4.2.10 and 4.2.11, we obtained δa and the uncertainty $\sigma_{\delta a}$ associated with it for each interferometer time. In figure 27 on the left, I present these results as the relative percentage $\frac{\delta a}{a} \times 100$. I have used the value of the scattering length a for ^{87}Sr as 5.09(10) nm [Martinez de Escobar et al., 2008]. As expected, we find that at 10 ms, there is a substantial amount of uncertainty in the measured value of differential scattering length due to the high degree of uncertainty in the energy measurement. This uncertainty decreases

with longer interferometer times. The measurement of the relative scattering length for each interferometer time is $\{700 \pm 500, 5 \pm 8, 15 \pm 10, 4 \pm 6\}$ %. Considering the measurement done at the interferometer time of 2 s, the estimation of differential scattering length is 4 ± 6 %, of the order of $10^{-2} \pm 10^{-2}$ %. In conclusion, we observe the SU(N) symmetry in the ground state $^1S_0$ manifold $\delta a/a$ within the uncertainty of the order of 10^{-2}.

Moving on to the following subsection, I will demonstrate how applying an additional potential will increase the average density of the gas. This is achieved by turning on the 1064 nm 1D lattice during the interferometric sequence. The increased density can result in a more precise measurement of the SU(N) symmetry.

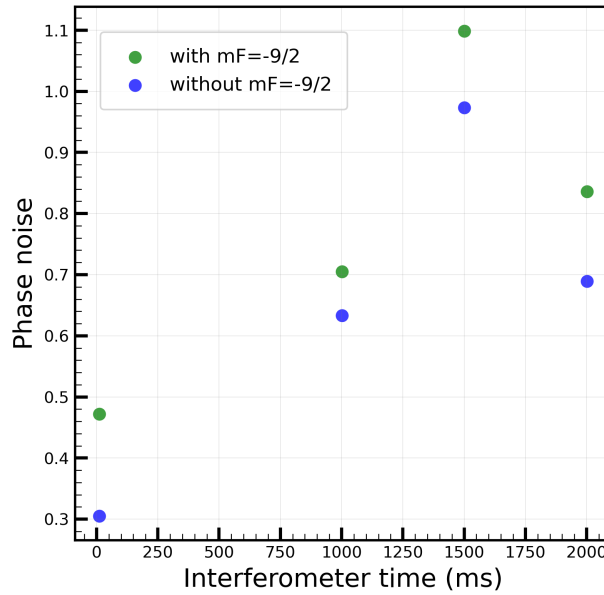### 4.2.5 Investigating the phase noise of the interferometer in the dark

Figure 28: The phase noise (in radian) of the interferometer as a function of the dark time for the spin state $|-5/2\rangle$.

During the precession of the qubit (phase accumulation of the Ramsey interferometer) only the external magnetic field is present. The fluctuation in the external magnetic fields appears as a noise in the phase of the interferometer. The external magnetic field during the interferometric sequence is produced by the coils that receive the current from the power supply Delta Electronika ES150. The current in the power supply has the relative temperature stability of 10^{-4}. Then the fluctuation in the phase of the

Ramsey interferometer due to the variation of the ambient temperature is given by the equation 4.2.19

$$\delta\phi_{\text{field}} = 2\pi\,\Delta E\,\alpha_T\,\Delta T\,t/h \qquad\qquad (4.2.19)$$

where ΔE is the Zeeman splitting in the ground state manifold due to the external magnetic field, α_T is the temperature coefficient of the driving power supply, ΔT is the ambient temperature change, and t is the dark time. The $\delta\phi_{\text{field}}$ at 2 s is approximately 1 radians. The fluctuations in the phase of the interferometer due to the stability of the DDS that drives the two beams is given by the equation 4.2.20

$$\delta\phi_{\text{DDS}} = 2\pi\cdot\delta(\omega_1 - \omega_2)\cdot t/h \qquad\qquad (4.2.20)$$

where $\delta(\omega_1 - \omega_2)$ is given by the relationship $\delta(\omega_1 - \omega_2) = \mathcal{R}\cdot(\omega_1 - \omega_2)$, $\mathcal{R}$ being the relative stability of the DDS which is 10^{-5}. The $\delta\phi_{\text{DDS}}$ at 2 s is approximately 0.1 radian. Hence, the overall technical phase noise of the interferometer is expected to be $\delta\phi = \sqrt{\delta\phi_{\text{field}}^2 + \delta\phi_{\text{DDS}}^2} \approx 1$ radian.

The measurement noise in our interferometer is dominated by the phase noise. For instance, at the darktime of the order of seconds, the phase noise is estimated as approximately 1 radian as shown in figure 28. Based on the DDS stabilities and the power sources used to create the magnetic field as previously mentioned, this noise can be understood. Moreover, the dominating noise comes from the power source used to create the magnetic field in the experiment. They are purely technical and can be improved in the future by changing the equipment with better stability. At the limit of the noise, the estimation of the error in measuring the SU(N) will be minimal. We have now understood the noise limitations in the dark in our interferometer. I will now move on to the next section.

4.2.6 Increase of confinement density by an additional potential

When performing the interferometry, the Fermi gas is held in the optical dipole trap. The density of the gas in the trap is determined by parameters such as the depth of the optical dipole trap, confinement frequencies in the three orthogonal directions, and the temperature of the gas. After the evaporation in the optical dipole trap, the effective confinement frequency is approximately 50 Hz. By adiabatically applying

an additional potential, we can increase the effective confinement frequency without introducing excess energy into the system. This can be achieved by using 1064 nm infrared light, which aims to create a 1D lattice parallel to the direction of gravity. Using this 1D lattice, the confinement frequency along the lattice's axis can be increased significantly by an order of magnitude of two 10^2. This potential also provides an additional radial confinement within 10s of Hz. Overall, by combining these two potentials, we can increase the density of the gas. It is worth doing the interferometric test to probe SU(N) symmetry with this increased density. However, the gas density is spatially modulated due to the presence of the 1D lattice. Therefore, I shall begin by describing the theoretical calculation of gas density in the presence of a 1D lattice before presenting the experimental results in this subsection.

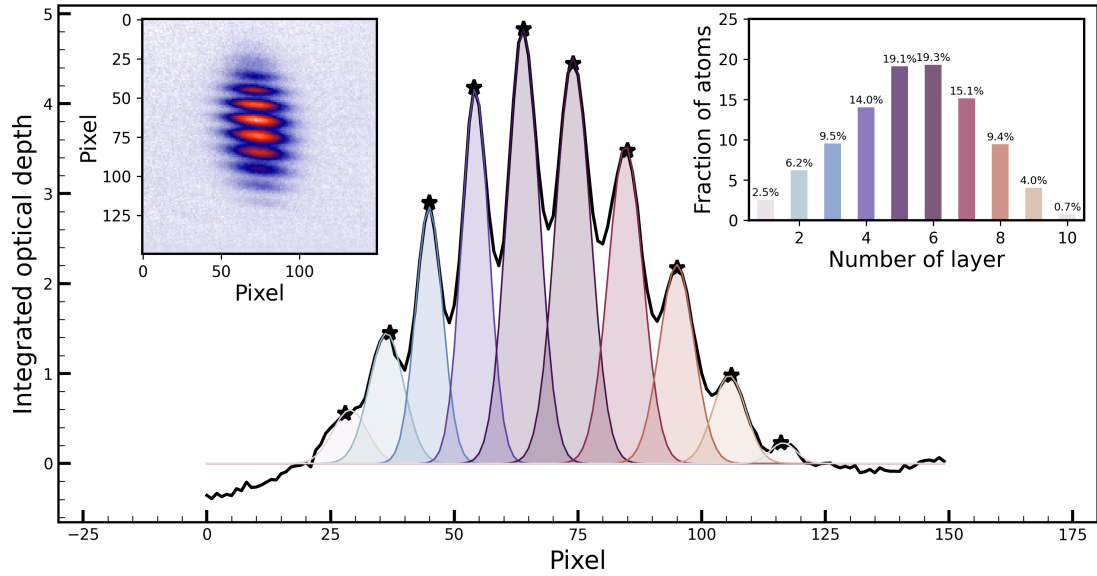### 4.2.7 Determination of the differential scattering inside a 1D lattice

Figure 29: Density profile of the gas within each layer of 1064 nm 1D lattice. Left figure: 2D picture of the density as a function of camera pixel measured after the quantum gas magnifier experiment. Central figure: the integrated version of the 2D picture along the axis of the 1D lattice with the sum of the Gaussian fits. Right figure: estimated fraction of the population of the number of atoms in each layer of the 1D lattice, calculated from the central picture.

The combination of the 1064 nm lattice and the optical dipole trap creates multiple layers of quasi-2D gas in a plane perpendicular to the direction of the lattice beam. A projection of this configuration along the line of sight of the imaging beam is shown

in the left inset figure 29. Within each quasi-2D layer, the gas density profile can be considered equivalent to a thermal gas in an anisotropic harmonic potential. For a thermal gas confined in an anisotropic harmonic potential, the density distribution depends on the temperatures and the trapping frequencies along the three perpendicular directions. In this configuration, the radial temperature along the two radial axes of the lattice is similar (I assume the gas to be thermalized), while the axial temperature is different. I define the two temperatures as T_r and T_z. T_r represents the temperature across the radial direction (perpendicular to gravity), while T_z represents the temperature along the axial direction (aligned with gravity). The temperatures T_r and T_z are measured by time-of-flight experiments and correspond to the kinetic energy spread in the radial and axial directions, respectively.

I start by calculating the peak density of a thermal gas in an anisotropic harmonic potential. Lets assume there are several number of quasi-2D layers. For i'th layer, the density profile $n_{mF}^{(i)}(x, y, z)$ of the gas in the spin state $|mF\rangle$ is given by:

$$n_{mF}^{(i)}(x, y, z) = n_{mF}^{0,(i)} \, \exp\left(-\frac{m\omega_r^2(x^2 + y^2)}{2k_B T_r}\right) \exp\left(-\frac{m\omega_z^2 z^2}{2k_B T_z}\right) \tag{4.2.21}$$

Here, $n_{mF}^{0,(i)}$ is the peak density of the gas in the i'th layer at the location (x,y,z)= (0,0,0). ω_r and ω_z are the global angular trapping frequencies in the radial and axial directions respectively. The trapping frequencies result from the combination of the two beams and are given by $\omega_r = \sqrt{\omega_{r,1064}^2 + \omega_{r,ODT}^2}$ and $\omega_z = \sqrt{\omega_{z,1064}^2 + \omega_{z,ODT}^2}$. Then, we can calculate the total number of atoms $N_{mF}^{(i)}$ in each layer by integrating the density over the 3D space $N_{mF}^{(i)} = \int n_{mF}^{(i)}(x, y, z) \, dx dy dz$. After rearranging, the peak density of the 3D gas Gaussian gas for the spin state $|mF\rangle$ in each layer at the center of the anharmonic trap is then given by:

$$n_{mF}^{0,(i)} = \frac{N_{mF}^{(i)} \cdot m^{3/2}\omega_r^2\omega_z}{(2\pi)^{3/2}k_B^{3/2}T_r T_z^{1/2}} \tag{4.2.22}$$

I will use this expression later in this sub-section. Now, I will determine the total phase shift $\Delta\phi$ in the Ramsey interferometer due to the mean-field interactions. The density inside each layer varies as a function of (x,y,z). Therefore, the phase of the Ramsey interferometer initiated by the mean-field interaction between the impurity atoms $|mF'\rangle$ and the atoms in the spin state $|mF\rangle$ also varies as a function of (x,y,z). Hence, I will calculate the average phase due to the mean-field interactions.

Given that the atoms are distributed across several layers labeled as i, let the fraction of atoms in the i'th layer be given by $f_i = \frac{N_{m_F}^{(i)}}{N_{m_F}} = \frac{n_{m_F}^{0,(i)}}{n_{m_F}^0}$. Here, N_{m_F} is the total number of atoms in the spin state $|mF\rangle$, and $n_{m_F}^0$ is the peak density if all the atoms are in one layer. Further, I assume each layer has the same temperatures T_r, T_z, and the trapping frequencies ω_r and ω_z. The total phase difference accumulated in the Ramsey interferometer is $\Delta\phi = \bar{\phi}_{mF_1,mF'} - \bar{\phi}_{mF_2,mF'}$. Where $\bar{\phi}_{mF_{\{1,2\}},mF'}$ is the average phase due to the inter-species mean field interaction between either of the spin states $\{|mF_1\rangle, |mF_2\rangle\}$ and the impurity atoms $|mF'\rangle$. Then, the average phase difference $\Delta\phi$ over the entire configuration is given by:

$$\bar{\phi}_{mF,mF'} = \sum_i \frac{N_{m_F}^{(i)}}{N_{m_F}} \bar{\phi}_{mF,mF'}^{(i)} = \sum_i f_i\, \bar{\phi}_{mF,mF'}^{(i)} \tag{4.2.23}$$

$\bar{\phi}_{mF,mF'}^{(i)}$ represents the average shift in each layer and is given by:

$$\bar{\phi}_{mF,mF'}^{(i)} = \frac{1}{N_{m_F}^{(i)}} \int dx\, dy\, dz\, n_{m_F}^{(i)}(x,y,z)\, \frac{4\pi\hbar^2 a_{mF,mF'}}{m}\, \frac{t}{\hbar}\, n_{mF'}^{(i)}(x,y,z) \tag{4.2.24}$$

$$= \frac{gt}{\hbar} \frac{1}{N_{m_F}^{(i)}} f_j \int dx\, dy\, dz\, n_{m_F}^{(i)\,2}(x,y,z) \tag{4.2.25}$$

$$= \frac{gt}{\hbar} \frac{n_{m_F}^0}{2\sqrt{2}} f_i f_j \tag{4.2.26}$$

where, I have defined f_j is the fraction of number of atoms $f_j = \frac{N_{mF'}}{N_{mF}} = \frac{n_{m_F'}^0}{n_{m_F}^0} = \frac{n_{m_F'}^{(i)}(x,y,z)}{n_{m_F}^{(i)}(x,y,z)}$ in the impurity spin state $|mF'\rangle$ and the spin state $|mF\rangle$. The coupling constant g is given by $g = \frac{4\pi\hbar^2 a_{mF,mF'}}{m}$. Then, using the equation 4.2.23, the average shift for all the layers is simply:

$$\bar{\phi}_{mF,mF'} = \frac{gt}{\hbar} \frac{n_{m_F}^0}{2\sqrt{2}} f_j \left(\sum_i f_i^2 \right) \tag{4.2.27}$$

and the total phase difference accumulated in the Ramsey interferometer is given by:

$$\Delta\phi = \bar{\phi}_{mF_1,mF'} - \bar{\phi}_{mF_2,mF'} \tag{4.2.28}$$

$$= \frac{4\pi\hbar^2}{m} \frac{t}{\hbar} \frac{n^0_{mF'}}{2\sqrt{2}} \left(a_{mF_1,mF'} - a_{mF_2,mF'}\right) \left(\sum_i f_i^2\right) \tag{4.2.29}$$

$$= \frac{4\pi\hbar^2}{m} \frac{t}{\hbar} \frac{n^0_{mF'}}{2\sqrt{2}} \delta a \left(\sum_i f_i^2\right) \tag{4.2.30}$$

In this equation, $n^0_{mF'}$ is the peak density of the impurity atoms if all the atoms are in one layer. Here, I have used the fact that $f_j \cdot n^0_{mF} = n^0_{mF'}$. Thus, the total average shift is proportional to the peak density of the impurity atoms, the sum of the squares of the fractional populations f_i in each layer, and the differential scattering length δa. Finally, the differential scattering length δa and the uncertainty $\sigma_{\delta a}$ associated with it is given by:

$$\delta a = \frac{m}{4\pi\hbar} \frac{1}{t} \frac{2\sqrt{2}}{n^0_{mF'}} \Delta\phi \left(\sum_i f_i^2\right)^{-1} \tag{4.2.31}$$

and

$$\sigma_{\delta a} = \frac{m}{4\pi\hbar t} \frac{2\sqrt{2}}{n^0_{mF'} \left(\sum_i f_i^2\right)} \cdot \sqrt{\sigma_{\Delta\phi}^2 + \left(\frac{\Delta\phi \sigma_{n^0_{mF'}}}{n^0_{mF'}}\right)^2 + \sum_i \left(\frac{-2f_i \Delta\phi \sigma_{f_i}}{\left(\sum_i f_i^2\right)}\right)^2} \tag{4.2.32}$$

In order to calculate the differential scattering length δa and the uncertainty $\sigma_{\delta a}$ on it, we need to estimate f_i, $\Delta\phi$ and $n^0_{mF'}$. Let's begin by calculating the fraction of atom f_i in each layer.

As shown in the inset figure 29 left, the quantum gas magnifier experiment [Asteria et al., 2021] reveals the fraction of population of atoms in each layer for the combination of 1064 nm 1D lattice and ODT. First, I integrated the pixels of this picture along the direction of the 1D lattice to produce a 1D array of integrated pixels, represented by the central plot in this figure. Then, this plot is fitted with the sum of 1D Gaussians given by:

$$I(x) = I_0 + \sum_i A_i \exp\left(-\frac{(x-\mu_i)^2}{2\sigma_i^2}\right) \tag{4.2.33}$$

Where $I(x)$ represents the integrated optical depth, and I_0 is the background noise. The number of atoms in the i'th layer centered at μ_i (here μ_i and x are in pixels) is proportional to the $A_i \cdot \sigma_i$. The fraction of atoms in the i'th layer is given by $f_i = \frac{A_i \cdot \sigma_i}{\sum_i A_i \cdot \sigma_i}$. The bar graph in the right inset bar graph represents the fraction of atoms in each layer. After determining the fraction of atoms in each layer, we can proceed to calculate the peak density of the impurity atoms.

Furthermore, the kinetic energy K of a 3D Gaussian gas in an anisotropic trap can be calculated using the equipartition theorem. In 3D, the average kinetic energy per particle is $\frac{3}{2}k_B T$, however, the temperatures differ along radial T_r and axial T_z directions. The total kinetic energy for N atoms is given by $K = \frac{1}{2}N(2k_B T_r + k_B T_z)$. Similarly, the potential energy U in a harmonic trap follows the equipartition theorem. Each direction contributes $\frac{1}{2}k_B T$ per particle, resulting total kinetic energy equal to the total potential energy:

$$K = U = \frac{1}{2}N(2k_B T_r + k_B T_z) \tag{4.2.34}$$

Therefore, if the kinetic energy is measured by observing the momentum spread in a time-of-flight (TOF) experiment, the potential energy can be directly inferred, as they are identical. This equality simplifies the analysis of such systems, allowing one to determine the total energy distribution by measuring either the kinetic or potential energy.

Since the effective potential of the 1064 nm 1D lattice and the optical dipole trap is an anharmonic trap, it is essential to determine the temperature along different spatial directions. The temperature of the gas can be extracted by fitting a 2D Gaussian function to the spatial distribution of the optical depth in the absorbtion image. The process begins with obtaining the 2D Gaussian fit to the spatial distribution of the thermal gas after it has expanded during a time-of-flight (TOF) of 5 ms. Here, I assume that the gas is thermalized so that the temperature along the plane perpendicular to the gravity axis (along z) are same, meaning $T_x = T_y = T_r$ and I shall denote these temperature by T_r. The widths of the Gaussian fit along the z and r axes, denoted as σ_z and σ_r, respectively, are directly related to the temperature of the gas along those axes. These parameters are derived from the fitted 2D Gaussian model:
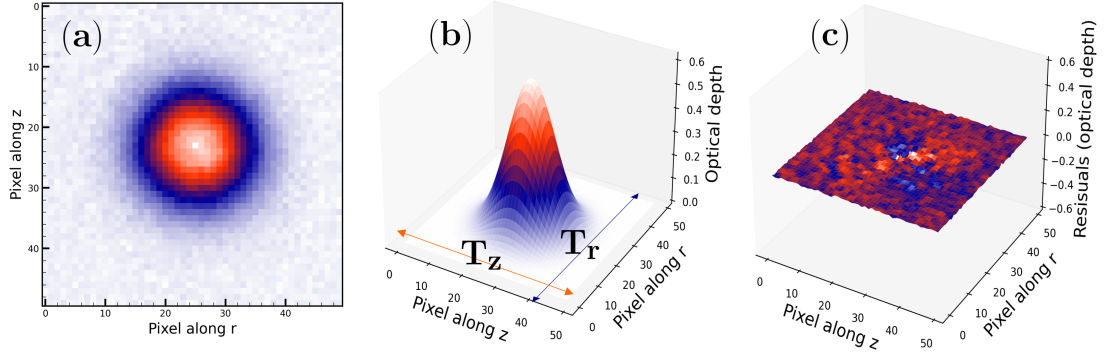
Figure 30: Temperature calculation for the 3D Gaussian gas inside the optical dipole trap's harmonic potential. Figure (a) shows an absorption image in pixels following a 5-ms time of flight (TOF) experiment. Figure (b) shows a 2D Gaussian fit of the absorbtion image in figure (a) to extract T_z and T_r along their respective axes. Figure (b) shows the residuals of the two-dimensional Gaussian fit.

$$I(z,r) = I_0 + A \exp\left(-\left(\frac{(z-z_0)^2}{2\sigma_z^2} + \frac{(r-r_0)^2}{2\sigma_r^2}\right)\right) \tag{4.2.35}$$

In this model, σ_z and σ_r correspond to the standard deviations of the Gaussian distribution along the z and r directions, respectively. These widths capture the spatial spread of the gas after expansion, reflecting the underlying velocity distribution of the atoms. Furthermore, $I(z,r)$ is the optical depth in the absorbtion image and A is the amplitude of the Gaussian fit. Once σ_z and σ_r are obtained from the 2D Gaussian fit, they are used to calculate the temperatures T_z and T_r along the respective axes z and r by the relationships:

$$T_z = \frac{\sigma_{v(z)}^2 \cdot m}{k_B} = \frac{\sigma_{r(z)}^2 \cdot m \cdot \left(S_{pixel}\right)^2}{k_B \left(\Delta t_{TOF}\right)^2} \tag{4.2.36}$$

and

$$T_r = \frac{\sigma_{v(r)}^2 \cdot m}{k_B} = \frac{\sigma_{r(r)}^2 \cdot m \cdot \left(S_{pixel}\right)^2}{k_B \left(\Delta t_{TOF}\right)^2} \tag{4.2.37}$$

σ_z and σ_r are the Gaussian widths obtained from the fit in the position space, m is the mass of a single ^{87}Sr atom, k_B is the Boltzmann constant, S_{pixel} is the size of a pixel in the image and is 6.5 µm, and Δt_{TOF} is the duration of the time-of-flight expansion. To convert Gaussian width from velocity to position space, we use the formula $\sigma_{v\{z,r\}}^2 = \sigma_{r\{z,r\}}^2 \cdot (S_{pixel})^2 / (\Delta t_{TOF})^2$. From this analysis the temperature $T_z = 830 \pm 5$ nK and $T_r = 720 \pm 5$ nK are known.

4.2.8 Measurement of the depth of 1064 nm 1D lattice

In order to finally calculate the peak density $n_{mF'}^0$ of the impurity atoms inside the trap, we need $\omega_{z,1064}$ and $\omega_{r,1064}$. Which can be calculated from the depth of the 1064 nm lattice V_{1064}. Where $\omega_{z,1064}$ is the harmonic oscillation frequency $\omega_{z,1064} = 2\sqrt{V_{1064}E_r}/\hbar$. V_{1064} is the lattice depth and E_r is the recoil energy associated with lattice. We turned on the lattice with a square pulse with a duration τ to determine the lattice depth at 1064 nm. After the square pulse, the TOF experiment is performed. The potential energy of the atoms is fully converted into kinetic energy, leading to a spread in momentum that is measured after TOF. In our experiment, atoms are confined in a one-dimensional optical lattice. Therefore, we need to measure the momentum spread in one direction only. The spatial spread Δx of the atomic cloud after TOF Δt, related to the velocity spread Δv_{max} by $\Delta v_{max} = \Delta x/2\Delta t$, allows us to calculate the maximum kinetic energy and hence infer the lattice depth:

$$V_{1064} = \frac{1}{2}m\Delta v_{max}^2 \tag{4.2.38}$$

For deep lattice potentials, where $V_{1064} \gg E_R$ (with E_R being the recoil energy $E_R = \frac{\hbar^2 k^2}{2m}$) of the lattice, the energy bands become very flat, and the motion of the atoms is primarily confined to the bottom of the potential wells. In this regime, the potential at each lattice site can be locally approximated by a harmonic potential $V_{1064}(x \approx x_i) \approx \frac{1}{2}m\omega_{z,1064}^2(x - x_i)^2$ [Gerbier, 2015], where $\omega_{z, 1064}$ is the band gap from the lowest to the first excited band (equal to harmonic oscillation frequency), and x_i represents the positions of the lattice minima. The band gap $\omega_{z, 1064}$ is then given by:

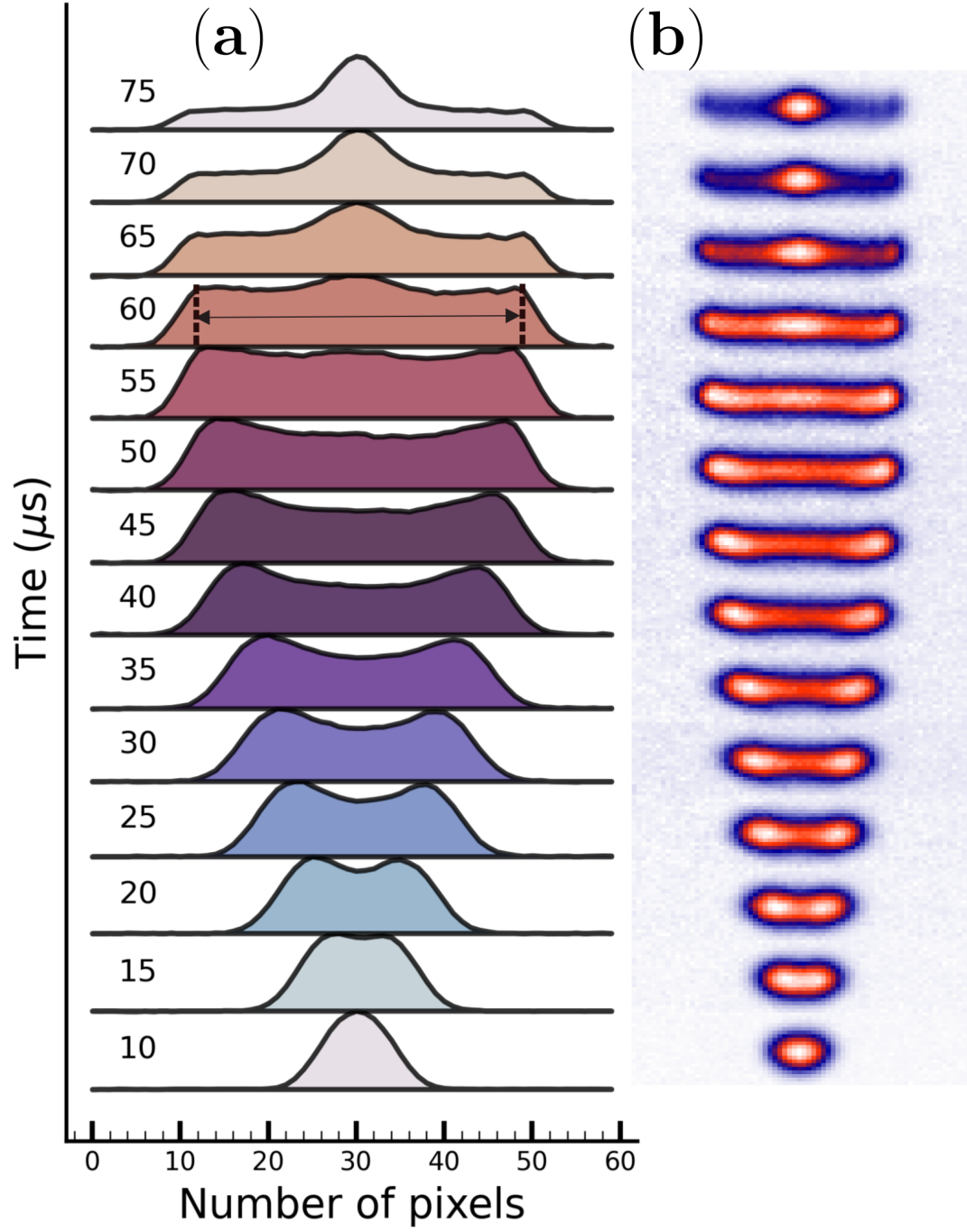$$\omega_{z, 1064} = \frac{2}{\hbar}\sqrt{V_{1064}E_R} \tag{4.2.39}$$

Figure 31: Measurement of lattice depth V_{1064} using TOF experiment. Figure (a) depicts the momentum spread of the gas after a 5 ms TOF in pixels, with each pixel measuring 6.5 μm. Figure (b) depicts the raw image from the experiment used to generate Figure (a). In both cases, each image is the average of five images taken in random order and merged to show the dynamics.

This indicates that the local curvature of the lattice potential is directly related to the lattice depth and the recoil energy. Finally, the radial trapping frequency can be estimated using a straightforward relation of the potential energy of the harmonic oscillator:

$$\omega_{\text{r, 1064}} = \sqrt{\frac{4V_0}{mw^2}} \tag{4.2.40}$$

where w is the Gaussian beam waist, governs the confinement in the transverse direction. This frequency, along with the band gap and lattice depth, characterizes the overall dynamics of atoms in the lattice and are needed for the calculation of the peak density n_{mF}^0 of the atoms inside the trap.

The experimental result of the lattice depth measurement is shown in Figure 31. The dynamics of momentum spread as a function of lattice pulse time are plotted vertically in pixels. The lattice depth is given by the maximum momentum spread, which is the maximum potential energy in the lattice. Each picture is taken after 5 µs to capture the dynamics. The lattice depth using the relation 4.2.38 is calculated as V_{1064} = 92 kHz. Then using the relations 4.2.39 and 4.2.40, the band gap and the radial confinement frequency is $\{\omega_{\text{z, 1064}}, \omega_{\text{r, 1064}}\}$ = $\{7000, 45\}$ Hz.

Based on the calculation of these frequencies, the effective trapping frequencies in the presence of 1D lattice are approximately $\{\omega_r, \omega_z\} = 2\pi\{7000, 67\}$ rad/s. With the knowledge of temperature estimated in the earlier subsection, The average density $n_{\text{mF}}^0/2\sqrt{2}$ of the impurity atoms is known $(9.3 \pm 0.3) \times 10^{17}$ m^{-3}. The density is one order of magnitude higher than the density of the bulk gas. Our next goal is to find the phase difference $\Delta\phi$ to estimate the differential scattering length.

4.2.9 Estimation of the phase difference in the presence of a 1D 1064 nm lattice

Figure 32 shows the experimental data of the interferometer done in the presence of the 1D 1064 nm lattice. The experiment is repeated five times, and each data point in the figure represents the interferometer's output for a time window ranging from 1000 ms to 1002 ms. Each interferometer dataset is obtained for the two cases shown by the inset figure. The first case is represented by black circles, indicating the absence of impurity atoms $|-9/2\rangle$. The second case is shown with green circles, signifying the presence of impurity atoms $|-9/2\rangle$. For extracting the phase, I applied the same analysis used for phase estimation in the bulk gas. After performing the analysis, the
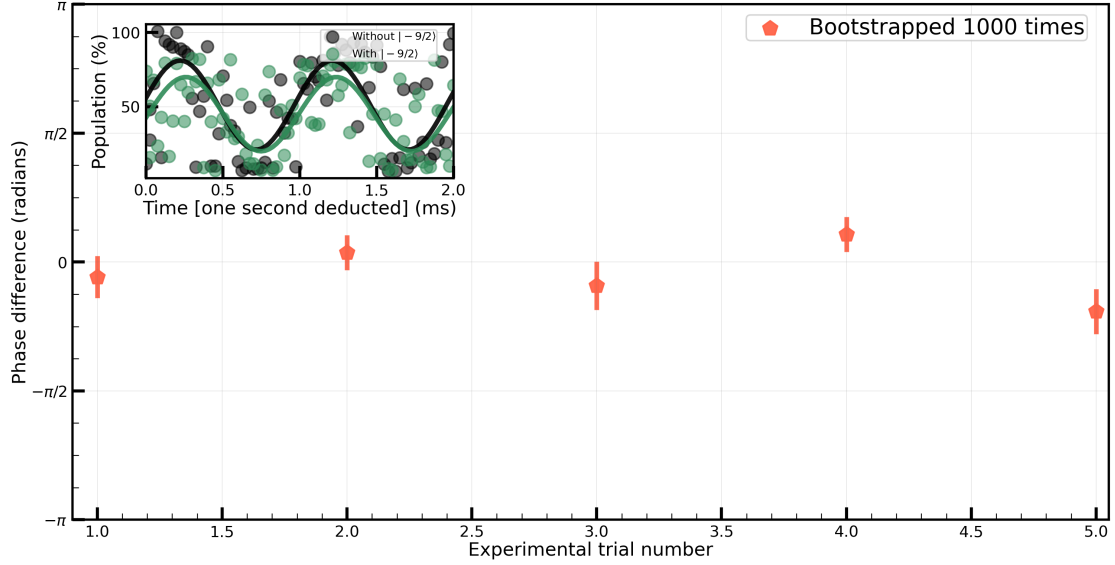
Figure 32: Main figure: phase difference $\Delta\phi$ in radians plotted as a function of experimental trials. Analyzing a single interferometer data set of 2 ms provided one data point in the figure. The error bars on the data are standard deviations from bootstrapping. Inset figure: Black dots represent the population in the spin state $|-5/2\rangle$ without the presence of the impurity state $|-9/2\rangle$ while the green dots are in the same population but with impurity atoms. The time window for the inset figure is 1000 ms to 1002 ms. All the datasets are taken for the same time window.

phase difference is $\Delta\phi = |\phi_1 - \phi_2|$, where ϕ_1 and ϕ_2 are the fitted phase in the two cases. The standard deviation on $\Delta\phi$ is the quadrature sum of the standard deviation of the phase in the two cases. The phase difference and the associated uncertainty for each dataset are obtained as $\{0.18 \pm 0.25, 0.11 \pm 0.21, 0.29 \pm 0.29, 0.21 \pm 0.23, 0.60 \pm 0.27\}$ radians. The main figure 32 plots the phase difference and the uncertainty associated with them.

Now, we have found all the necessary parameters to estimate the differential scattering length and the uncertainty associated with it. Plugging all the parameters in the equations 4.2.31 and 4.2.32 the desired result are estimated. Figure 33 shows the estimated results. We observe that our results $\frac{\delta a}{a} \times 100$ ranges roughly from $(2-10) \pm 5\%$. Here, I have taken the upper limit of the uncertainties of the datasets as a global uncertainty. We also observe that this result exhibits the same level of precision as the result of the SU(N) symmetry test in the bulk gas. The reason being the differential scattering length scales with modified effective density as $\delta a \propto \frac{1}{n^0_{mF'} \sum_i f_i^2}$. We effectively increase the term (modified density) $n^0_{mF'} \sum_i f_i^2$ by a factor of two. The reason was that the temperature of the gas in the 1D lattice was high (which can be fixed by loading the gas adiabatically in the lattice). However, in contrast to the bulk gas
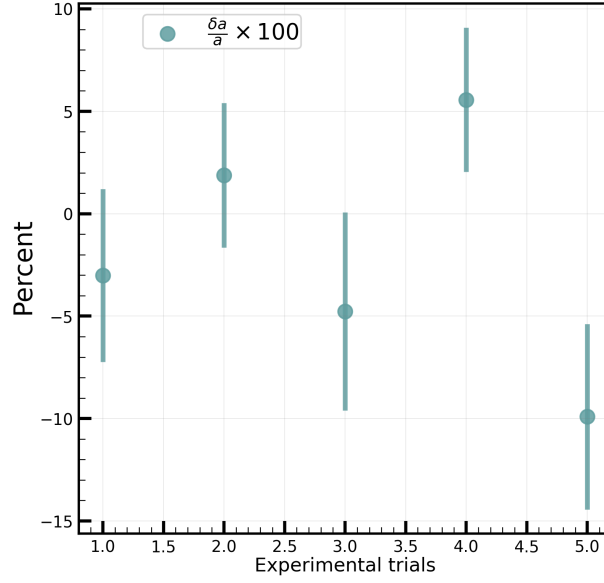
Figure 33: The differential scattering length and its associated uncertainty in the presence of a 1064 nm 1D lattice. The results are presented as the relative percentage $\frac{\delta a}{a} \times 100$, where a is the scattering length for ^{87}Sr.

case, these results are more reliable because we have measured the lattice depth (confinement frequencies) directly in the experiment. Furthermore, the standard deviation on the mean of each dataset giving $\frac{\delta a}{a} \times 100$ is about 5%, where the standard deviation on each dataset is roughly 4.5%. Since the standard deviation in the mean of each dataset is comparable to the standard deviation on each dataset, I can't take the average of these datasets. Based on these findings, I can state that we have seen the relative differential scattering length $\frac{\delta a}{a} \times 100$ values scattered between +5 to -10 with error bars of nearly ±5%.

4.3 FINAL THOUGHTS AND FUTURE OUTLOOK

I have presented the results for probing the SU(N) symmetric interactions within the nuclear spin in the ground state manifold. We noticed that the differential scattering length is inversely proportional $\delta a \propto 1/n^0_{mF'}$ to the peak density of the impurity atoms in the trap. Thus, increasing the density with the help of the tighter trap has more precision in the estimation of δa. I presented a preliminary result where I gained a factor of two in the density of the impurity atoms $n^0_{mF'}$. However, due to the diabatic loading of gas in the 1D lattice, I failed to achieve expected (one order of magnitude

more) precision in the measurement of the differential scattering length δa. Overall, I have have tested the SU(N) symmetry with no breaking within the experimental relative uncertainty of around 10^{-2}. Furthermore, the noise is ultimately bigger while compression was performed.

In the future, I could point out a few procedures that could result in more precise measurements of the differential scattering length δa. For instance, during the interferometer, the gas can be re-compressed in the ODT to a full intensity which provides an effective confinement frequency of approximately 200 Hz. This frequency can be directly measured in the experiment by an experiment like parametric heating by modulating the laser intensity of the position of the trap to increase the reliability of the data. It is possible to load the gas within approximately two quasi 2D layers of the 1064 nm 1D lattice giving $\sum_i f_i^2$ as 0.5. With these steps, it will be possible to increase the density of the gas inside the 1064 nm by an order of magnitude more than present. Moreover, taking more data points or repeating the dataset for the same dark time will increase the precision of the estimation of $\Delta\phi$. I have presented the same by repeating the same dataset five times. For instance, on a given day the dataset can be repeated as much as 10 times which will increase the precision on $\Delta\phi$ by $\sqrt{10}$ times. With only these three steps, we can lower the precision on δa by roughly a factor of 30. Furthermore, we can minimize the phase noise of the interferometer by upgrading the DDS and power supplies to enhance their stability. With technical enhancements, improved density, and greater sensitivity in the phase of the interferometer, we can achieve a precision of 10^{-3} in probing the SU(N) symmetry.

Furthermore, our qubit coherence time is of the order of the lifetime of the Fermi gas, Ramsey interferometer visibility is not limited by the incoherent processes. Our measurement is at optimum precision in terms of the visibility of the interferometer without the need for schemes like dynamical de-coupling.
****

CONCLUSION

In this thesis, I have experimentally demonstrated the preparation and control over two isolated nuclear spins from the ground state manifold by optical methods. In the future of our experiment, this approach paves the way for simulating the 2D Fermi-Hubbard model with enhanced SU(N) symmetry using ^{87}Sr. In addition, I have also demonstrated that ^{87}Sr can be employed for high-dimensional interferometry, enabling access to physical quantities that are beyond the reach of standard two-state interferometry. Furthermore, we can test the SU(N) symmetry of ^{87}Sr itself. This thesis utilizes the large spin symmetry of ^{87}Sr and the long coherence of its nuclear spins. These are among the key requirements in the fields of quantum simulation, quantum computing, and metrology. Therefore, the studies done in this thesis can be applied in such fields.

In the first chapter I have presented manipulation of the nuclear spins by optical methods. I started by experimentally demonstrating the tensor light shifts which is in good agreement of my theoretical calculations. Then, I demonstated the Raman adiabatic passages with 80% one way efficiency limited by amplified spontaneous emission. During these experiments we noticed the anomalous heating on the Fermi gas that is coming from the laser that is used to create the tensor light shift, I confirmed this result by setting up a temporary filtering cavity.

When the adiabatic passages are realized inside the optical lattices, we will be able to write spin textures. It will then be possible to adiabatically approach the regime where many-body interactions are dominated by super-exchange mechanism, by slowly reducing the depth of the spin-dependent superlattice. This requires loading the Fermi gas inside the 3D optical lattice which is the combination of 1064 nm 1D lattice plus 532 nm 2D lattice. During the second year of my thesis, I worked on loading the gas in the lattice. I measured the excessive heating by an order of magnitude more than the expected one of the gas inside the 532 nm lattice. To solve this issue, we are currently preparing the active intensity stabilization to reduce the RIN.

I experimentally demonstrated coherent Rabi oscillations between three isolated pairs of nuclear spin states. In principle, it is possible to couple any two neighboring pairs of nuclear spin states within the entire ground state manifold. The next question

is how long is the coherence of the two isolated pairs and what is the dominant limitation? I was able to increase the coherence time of these Rabi oscillations by increasing the beam waist. Finally, I was able to achieve Rabi oscillations with a quality factor of nearly 100. Furthermore, I was able to demonstrate the coherent Rabi oscillation between the spin states $|mF\rangle$ and $|mF+2\rangle$. This way I showed the two different pairs possibilities to control the spins by optical methods. The advantage of controlling spin states $|mF\rangle$ and $|mF+2\rangle$ is that both the spin states can be measured simultaneously. This opens the door to measuring the correlations between the measured spin states.

The next chapter is dedicated to the high-dimensional interferometry with nuclear spins with long coherence. I have demonstrated two experimental applications of high-dimensional interferometers. The first one is a combination of two parallel Ramsey interferometers that run simultaneously. We can separate the two types of measured fields, tensor light shift and the linear field which is the combination of vector light shift and linear Zeeman shift. The second interferometers measure two or more collective atomic variables simultaneously. This can be one of the ways to measure the correlations between these two variables. One advantage of this interferometer is that we do not require standard tomography of the spin states to measure the correlations.

Furthermore, I identified the main sources of the phase noise in our interferometers. I was able to reduce the phase noise significantly such that direct fitting of the data with the model provides the estimation of parameters with reduced chi-square reaching one. In addition, we measured the coherence of the qubit in the presence of the tensor light shift. The next question was how long is the coherence of the superposition of the nuclear spins when the tensor light shift is not present? As we expected, the coherence is maintained as long as the lifetime of the Fermi gas itself. I also pointed out that our measurement precision has not yet reached the standard quantum limit, but is approaching it.

In the last chapter, I have presented a scheme to test the SU(N) symmetry for ^{87}Sr based on the Ramsey interferometer. The scheme exploits the long coherence time of nuclear spin superpositions, which remain highly isolated from environmental perturbations. The precision of SU(N) symmetry measurements is inversely proportional to the density of impurity atoms. I attempted to increase the density of the gas with the help of a 1D 1064 nm lattice. Our first result is tentative and it necessitates precise measurement of the trapping frequencies in the optical dipole trap to improve the reliability of the outcome. Therefore, the next step is careful measurements of the trapping frequency of the optical dipole trap, which can be measured directly in the experiment. Additionally, by loading the gas into a 1064 nm 1D lattice and using

re-compression of the gas inside the dipole trap, achieving a precision of 10^{-3} in the SU(N) symmetry test should become straightforward. I've shown that the phase noise in our interferometer data is purely technical and can be reduced with a more stable power supply, which will further increase the precision of the estimation of the phase of the interferometer fringe.

BIBLIOGRAPHY

Affleck, Ian and J Brad Marston

    1988   "Large-n limit of the Heisenberg-Hubbard model: Implications for high-T c superconductors," *Physical Review B*, 37, 7, p. 3774.

Aguado, Miguel and Guifre Vidal

    2008   "Entanglement renormalization and topological order," *Physical review letters*, 100, 7, p. 070404.

Aidelsburger, Monika, Luca Barbiero, Alejandro Bermudez, Titas Chanda, Alexandre Dauphin, Daniel González-Cuadra, Przemysław R Grzybowski, Simon Hands, Fred Jendrzejewski, Johannes Jünemann, et al.

    2022   "Cold atoms meet lattice gauge theory," *Philosophical Transactions of the Royal Society A*, 380, 2216, p. 20210064.

Asteria, Luca, Henrik P Zahn, Marcel N Kosch, Klaus Sengstock, and Christof Weitenberg

    2021   "Quantum gas magnifier for sub-lattice-resolved imaging of 3D quantum systems," *Nature*, 599, 7886, pp. 571-575.

Babazadeh, Amin, Manuel Erhard, Feiran Wang, Mehul Malik, Rahman Nouroozi, Mario Krenn, and Anton Zeilinger

    2017   "High-dimensional single-photon quantum gates: concepts and experiments," *Physical review letters*, 119, 18, p. 180510.

Baillard, Xavier, Mathilde Fouché, Rodolphe Le Targat, Philip G Westergaard, Arnaud Lecallier, Frédéric Chapelet, Michel Abgrall, Giovanni D Rovera, Philippe Laurent, Peter Rosenbusch, et al.

    2008   "An optical lattice clock with spin-polarized 87 Sr atoms," *The European Physical Journal D*, 48, pp. 11-17.

Barnes, Katrina, Peter Battaglino, Benjamin J Bloom, Kayleigh Cassella, Robin Coxe, Nicole Crisosto, Jonathan P King, Stanimir S Kondov, Krish Kotru, Stuart C Larsen, et al.

    2022a   "Assembly and coherent control of a register of nuclear spin qubits," *Nature Communications*, 13, 1, p. 2779.

Barnes, Katrina, Peter Battaglino, Benjamin J. Bloom, Kayleigh Cassella, Robin Coxe, Nicole Crisosto, Jonathan P. King, Stanimir S. Kondov, Krish Kotru, Stuart C. Larsen, Joseph Lauigan, Brian J. Lester, Mickey McDonald, Eli Megidish, Sandeep Narayanaswami, Ciro Nishiguchi, Remy Notermans, Lucas S. Peng, Albert Ryou, Tsung-Yao Wu, and Michael Yarwood

2022b "Assembly and coherent control of a register of nuclear spin qubits," *Nature Communications*, 13, 1 [May 2022], ISSN: 2041-1723, DOI: 10.1038/s41467-022-29977-z, http://dx.doi.org/10.1038/s41467-022-29977-z.

Bataille, Pierre, Andrea Litvinov, Isam Manai, John Huckans, Fabrice Wiotte, Albert Kaladjian, Olivier Gorceix, Etienne Maréchal, Bruno Laburthe-Tolra, and Martin Robert-De-Saint-Vincent

2020 "Adiabatic spin-dependent momentum transfer in an SU (N) degenerate Fermi gas," *Physical Review A*, 102, 1, p. 013317.

Bernabeu, Jose

2020 "Symmetries and Their Breaking in the Fundamental Laws of Physics," *Symmetry*, 12, 8, ISSN: 2073-8994, DOI: 10.3390/sym12081316, https://www.mdpi.com/2073-8994/12/8/1316.

Billy, Juliette, Vincent Josse, Zhanchun Zuo, Alain Bernard, Ben Hambrecht, Pierre Lugan, David Clément, Laurent Sanchez-Palencia, Philippe Bouyer, and Alain Aspect

2008 "Direct observation of Anderson localization of matter waves in a controlled disorder," *Nature*, 453, 7197, pp. 891-894.

Björck, Åke

1996 *Numerical Methods for Least Squares Problems*, Society for Industrial and Applied Mathematics, DOI: 10.1137/1.9781611971484, eprint: https://epubs.siam.org/doi/pdf/10.1137/1.9781611971484, https://epubs.siam.org/doi/abs/10.1137/1.9781611971484.

Blatt, S, AD Ludlow, GK Campbell, Jan Westenkær Thomsen, T Zelevinsky, MM Boyd, J Ye, Xavier Baillard, Mathilde Fouché, Rodolphe Le Targat, et al.

2008 "New limits on coupling of fundamental constants to gravity using Sr 87 optical lattice clocks," *Physical review letters*, 100, 14, p. 140801.

Bloch, Immanuel, Jean Dalibard, and Wilhelm Zwerger

2008 "Many-body physics with ultracold gases," *Reviews of modern physics*, 80, 3, pp. 885-964.

Boggs, Paul T and Janet E Rogers

1990 "Orthogonal distance regression," *Contemporary mathematics*, 112, pp. 183-194.

Bouton, Quentin, Jens Nettersheim, Sabrina Burgardt, Daniel Adam, Eric Lutz, and Artur Widera

2021 "A quantum heat engine driven by atomic collisions," *Nature Communications*, 12, 1, p. 2063.

Boyd, Martin M, Andrew D Ludlow, Sebastian Blatt, Seth M Foreman, Tetsuya Ido, Tanya Zelevinsky, and Jun Ye

2007 "Sr 87 Lattice Clock with Inaccuracy below 10-15," *Physical Review Letters*, 98, 8, p. 083002.

Bringhurst, Robert

1992 *The Elements of Typographic Style*, Hartley & Marks, Point Roberts, Washington, USA.

Büchler, HP, A Micheli, and P Zoller

2007 "Three-body interactions with cold polar molecules," *Nature Physics*, 3, 10, pp. 726-731.

Bullock, Stephen S, Dianne P O'Leary, and Gavin K Brennen

2005 "Asymptotically optimal quantum circuits for d-level systems," *Physical review letters*, 94, 23, p. 230502.

Buluta, Iulia and Franco Nori

2009 "Quantum simulators," *Science*, 326, 5949, pp. 108-111.

Cadoret, Malo, Estefania de Mirandes, Pierre Cladé, Saïda Guellati-Khélifa, Catherine Schwob, Fran çois Nez, Lucile Julien, and Fran çois Biraben

2008 "Combination of Bloch Oscillations with a Ramsey-Bordé Interferometer: New Determination of the Fine Structure Constant," *Phys. Rev. Lett.*, 101 [23 Dec. 2008], p. 230801, DOI: `10.1103/PhysRevLett.101.230801`, `https://link.aps.org/doi/10.1103/PhysRevLett.101.230801`.

Canuel, B, A Bertoldi, L Amand, E Pozzo di Borgo, T Chantrait, C Danquigny, Miguel Dovale Álvarez, B Fang, Andreas Freise, R Geiger, et al.

2018 "Exploring gravity with the MIGA large scale atom interferometer," *Scientific Reports*, 8, 1, p. 14064.

Capponi, Sylvain, Philippe Lecheminant, and Keisuke Totsuka

2016   "Phases of one-dimensional SU (N) cold atomic Fermi gases—From molecular Luttinger liquids to topological phases," *Annals of Physics*, 367, pp. 50-95.

Castro Neto, Antonio H, Francisco Guinea, Nuno MR Peres, Kostya S Novoselov, and Andre K Geim

2009   "The electronic properties of graphene," *Reviews of modern physics*, 81, 1, pp. 109-162.

Cazalilla, M A, A F Ho, and M Ueda

2009   "Ultracold gases of ytterbium: ferromagnetism and Mott states in an SU(6) Fermi system," *New Journal of Physics*, 11, 10 [Oct. 2009], p. 103033, ISSN: 1367-2630, DOI: 10.1088/1367-2630/11/10/103033, http://dx.doi.org/10.1088/1367-2630/11/10/103033.

Cazalilla, Miguel A, AF Ho, and M Ueda

2009   "Ultracold gases of ytterbium: ferromagnetism and Mott states in an SU (6) Fermi system," *New Journal of Physics*, 11, 10, p. 103033.

Cazalilla, Miguel A and Ana Maria Rey

2014a   "Ultracold Fermi gases with emergent SU (N) symmetry," *Reports on Progress in Physics*, 77, 12, p. 124401.

2014b   "Ultracold Fermi gases with emergent SU(N) symmetry," *Reports on Progress in Physics*, 77, 12 [Nov. 2014], p. 124401, ISSN: 1361-6633, DOI: 10.1088/0034-4885/77/12/124401, http://dx.doi.org/10.1088/0034-4885/77/12/124401.

Cetina, Marko, Michael Jag, Rianne S. Lous, Isabella Fritsche, Jook T. M. Walraven, Rudolf Grimm, Jesper Levinsen, Meera M. Parish, Richard Schmidt, Michael Knap, and Eugene Demler

2016   "Ultrafast many-body interferometry of impurities coupled to a Fermi sea," *Science*, 354, 6308, pp. 96-99, DOI: 10.1126/science.aaf5134, eprint: https://www.science.org/doi/pdf/10.1126/science.aaf5134, https://www.science.org/doi/abs/10.1126/science.aaf5134.

Clemmen, Stéphane, Alessandro Farsi, Sven Ramelow, and Alexander L Gaeta

2016   "Ramsey interference with single photons," *Physical review letters*, 117, 22, p. 223601.

Coleman, Piers

1983   "1 N expansion for the Kondo lattice," *Physical Review B*, 28, 9, p. 5255.

Comparin, Tommaso, Fabio Mezzacapo, Martin Robert-de-Saint-Vincent, and Tommaso Roscilde

2022 "Scalable spin squeezing from spontaneous breaking of a continuous symmetry," *Physical Review Letters*, 129, 11, p. 113201.

Cozzolino, Daniele, Beatrice Da Lio, Davide Bacco, and Leif Katsuo Oxenløwe

2019 "High-dimensional quantum communication: benefits, progress, and future challenges," *Advanced Quantum Technologies*, 2, 12, p. 1900038.

Das, Purnendu, Valentin Leeb, Johannes Knolle, and Michael Knap

2024 "Realizing altermagnetism in fermi-hubbard models with ultracold atoms," *Physical Review Letters*, 132, 26, p. 263402.

Derevianko, Andrei and Hidetoshi Katori

2011 "Colloquium: Physics of optical lattice clocks," *Reviews of Modern Physics*, 83, 2, pp. 331-347.

DeSalvo, Brian J, Mi Yan, Pascal Gerry Mickelson, YN Martinez de Escobar, and Thomas C Killian

2010 "Degenerate fermi gas of sr 87," *Physical Review Letters*, 105, 3, p. 030402.

Efron, B.

1979 "Bootstrap Methods: Another Look at the Jackknife," *The Annals of Statistics*, 7, 1, pp. 1-26, DOI: 10.1214/aos/1176344552, https://doi.org/10.1214/aos/1176344552.

Efron, Bradley and Robert J Tibshirani

1993 "An introduction to the bootstrap Chapman & Hall," *New York*, 436.

Feng, XN and LF Wei

2021 "Multilevel atomic Ramsey interferometry for precise parameter estimations," *Chinese Physics B*, 30, 12, p. 120601.

Feynman, Richard P

1966 "Symmetry in physical laws," *The Physics Teacher*, 4, 4, pp. 161-174.

Fickler, Robert, Radek Lapkiewicz, William N Plick, Mario Krenn, Christoph Schaeff, Sven Ramelow, and Anton Zeilinger

2012 "Quantum entanglement of high angular momenta," *Science*, 338, 6107, pp. 640-643.

Fixler, J. B., G. T. Foster, J. M. McGuirk, and M. A. Kasevich

2007 "Atom Interferometer Measurement of the Newtonian Constant of Gravity," *Science*, 315, 5808, pp. 74-77, DOI: `10.1126/science.1135459`, eprint: `https://www.science.org/doi/pdf/10.1126/science.1135459`, `https://www.science.org/doi/abs/10.1126/science.1135459`.

Fixler, Jeffrey B, GT Foster, JM McGuirk, and MA Kasevich

2007 "Atom interferometer measurement of the Newtonian constant of gravity," *Science*, 315, 5808, pp. 74-77.

Gadway, Bryce, Daniel Pertot, René Reimann, Martin G Cohen, and Dominik Schneble

2009 "Analysis of Kapitza-Dirac diffraction patterns beyond the Raman-Nath regime," *Optics express*, 17, 21, pp. 19173-19180.

Georgescu, Iulia M, Sahel Ashhab, and Franco Nori

2014 "Quantum simulation," *Reviews of Modern Physics*, 86, 1, pp. 153-185.

Gerbier, Fabrice

2015 "Quantum gases in optical lattices," *Physics World.()*

Gerbier, Fabrice and Jean Dalibard

2010 "Gauge fields for ultracold atoms in optical superlattices," *New Journal of Physics*, 12, 3 [Mar. 2010], p. 033007, ISSN: 1367-2630, DOI: `10.1088/1367-2630/12/3/033007`, `http://dx.doi.org/10.1088/1367-2630/12/3/033007`.

Giovanazzi, S

2005 "Hawking radiation in sonic black holes," *Physical review letters*, 94, 6, p. 061302.

Godfrin, Clément, Rafik Ballou, Edgar Bonet, Mario Ruben, Svetlana Klyatskaya, Wolfgang Wernsdorfer, and Franck Balestro

2018a "Generalized Ramsey interferometry explored with a single nuclear spin qudit," en, *npj Quantum Information*, 4, 1 [Oct. 2018], pp. 1-7, ISSN: 2056-6387, DOI: `10.1038/s41534-018-0101-3`, `https://www.nature.com/articles/s41534-018-0101-3`.

2018b "Generalized Ramsey interferometry explored with a single nuclear spin qudit," en, *npj Quantum Information*, 4, 1 [Oct. 2018], pp. 1-7, ISSN: 2056-6387, DOI: `10.1038/s41534-018-0101-3`, `https://www.nature.com/articles/s41534-018-0101-3` [visited on 07/19/2024].

Gorshkov, A. V., M. Hermele, V. Gurarie, C. Xu, P. S. Julienne, J. Ye, P. Zoller, E. Demler, M. D. Lukin, and A. M. Rey

2010 "Two-orbital S U(N) magnetism with ultracold alkaline-earth atoms," *Nature Physics*, 6, 4 [Feb. 2010], pp. 289-295, ISSN: 1745-2481, DOI: 10.1038/nphys1535, http://dx.doi.org/10.1038/NPHYS1535.

Gorshkov, Alexey Vyacheslavovich, M Hermele, V Gurarie, C Xu, Paul S Julienne, J Ye, Peter Zoller, Eugene Demler, Mikhail D Lukin, and AM Rey

2010 "Two-orbital SU (N) magnetism with ultracold alkaline-earth atoms," *Nature physics*, 6, 4, pp. 289-295.

Greiner, Markus, Olaf Mandel, Tilman Esslinger, Theodor W Hänsch, and Immanuel Bloch

2002 "Quantum phase transition from a superfluid to a Mott insulator in a gas of ultracold atoms," *nature*, 415, 6867, pp. 39-44.

Griffin, P F, K J Weatherill, S G MacLeod, R M Potvliege, and C S Adams

2006 "Spatially selective loading of an optical lattice by light-shift engineering using an auxiliary laser field," *New Journal of Physics*, 8 [Jan. 2006], pp. 11-11, ISSN: 1367-2630, DOI: 10.1088/1367-2630/8/1/011, http://dx.doi.org/10.1088/1367-2630/8/1/011.

Gross, Christian and Immanuel Bloch

2017 "Quantum simulations with ultracold atoms in optical lattices," *Science*, 357, 6355, pp. 995-1001.

Heinz, A., A. J. Park, N. Šanti ć, J. Trautmann, S. G. Porsev, M. S. Safronova, I. Bloch, and S. Blatt

2020 "State-Dependent Optical Lattices for the Strontium Optical Qubit," *Phys. Rev. Lett.*, 124 [20 May 2020], p. 203201, DOI: 10.1103/PhysRevLett.124.203201, https://link.aps.org/doi/10.1103/PhysRevLett.124.203201.

Heinz, André, Annie Jihyun Park, Neven Šantić, Jan Trautmann, SG Porsev, MS Safronova, Immanuel Bloch, and Sebastian Blatt

2020 "State-dependent optical lattices for the strontium optical qubit," *Physical review letters*, 124, 20, p. 203201.

Henriet, Loïc, Lucas Beguin, Adrien Signoles, Thierry Lahaye, Antoine Browaeys, Georges-Olivier Reymond, and Christophe Jurczak

2020 "Quantum computing with neutral atoms," *Quantum*, 4, p. 327.

Hensen, Bas, Wister Wei Huang, Chih-Hwan Yang, Kok Wai Chan, Jun Yoneda, Tuomo Tanttu, Fay E Hudson, Arne Laucht, Kohei M Itoh, Thaddeus D Ladd, et al.

2020 "A silicon quantum-dot-coupled nuclear spin qubit," *Nature nanotechnology*, 15, 1, pp. 13-17.

Hermele, Michael, Victor Gurarie, and Ana Maria Rey

2011 "Mott Insulators of Ultracold Fermionic Alkaline Earth Atoms: Underconstrained Magnetism and Chiral Spin Liquid (vol 103, 135301, 2009)," *PHYSICAL REVIEW LETTERS*, 107, 5.

Hölzl, C., A. Götzelmann, E. Pultinevicius, M. Wirth, and F. Meinert

2024 "Long-Lived Circular Rydberg Qubits of Alkaline-Earth Atoms in Optical Tweezers," *Physical Review X*, 14, 2 [May 2024], ISSN: 2160-3308, DOI: 10.1103/physrevx.14.021024, http://dx.doi.org/10.1103/PhysRevX.14.021024.

Huang, Kerson and Chen Ning Yang

1957 "Quantum-mechanical many-body problem with hard-sphere interaction," *Physical review*, 105, 3, p. 767.

Huie, William, Lintao Li, Neville Chen, Xiye Hu, Zhubing Jia, Won Kyu Calvin Sun, and Jacob P. Covey

2023 "Repetitive Readout and Real-Time Control of Nuclear Spin Qubits in 171 Yb Atoms," *PRX Quantum*, 4, 3 [Sept. 2023], ISSN: 2691-3399, DOI: 10.1103/prxquantum.4.030337, http://dx.doi.org/10.1103/PRXQuantum.4.030337.

Jackson, Daniel M, Dorian A Gangloff, Jonathan H Bodey, Leon Zaporski, Clara Bachorz, Edmund Clarke, Maxime Hugues, Claire Le Gall, and Mete Atatüre

2021 "Quantum sensing of a coherent single spin excitation in a nuclear ensemble," *Nature Physics*, 17, 5, pp. 585-590.

Jarmola, Andrey, Sean Lourette, Victor M. Acosta, A. Glen Birdwell, Peter Blümler, Dmitry Budker, Tony Ivanov, and Vladimir S. Malinovsky

2021 "Demonstration of diamond nuclear spin gyroscope," *Science Advances*, 7, 43, eabl3840, DOI: 10.1126/sciadv.abl3840, eprint: https://www.science.org/doi/pdf/10.1126/sciadv.abl3840, https://www.science.org/doi/abs/10.1126/sciadv.abl3840.

Kaltenbaek, Rainer, Jonathan Lavoie, Bei Zeng, Stephen D Bartlett, and Kevin J Resch

2010 "Optical one-way quantum computing with a simulated valence-bond solid," *Nature Physics*, 6, 11, pp. 850-854.

Kassal, Ivan, James D Whitfield, Alejandro Perdomo-Ortiz, Man-Hong Yung, and Alán Aspuru-Guzik

2011 "Simulating chemistry using quantum computers," *Annual review of physical chemistry*, 62, 1, pp. 185-207.

KATZIR, SHAUL

2004 "The emergence of the principle of symmetry in physics," *Historical Studies in the Physical and Biological Sciences*, 35, 1, pp. 35-65, ISSN: 08909997, http://www.jstor.org/stable/10.1525/hsps.2004.35.1.35 [visited on 08/03/2024].

Kiktenko, EO, AK Fedorov, AA Strakhov, and VI Man'Ko

2015 "Single qudit realization of the Deutsch algorithm using superconducting many-level quantum circuits," *Physics Letters A*, 379, 22-23, pp. 1409-1413.

Kolkowitz, S., S. L. Bromley, T. Bothwell, M. L. Wall, G. E. Marti, A. P. Koller, X. Zhang, A. M. Rey, and J. Ye

2016 "Spin–orbit-coupled fermions in an optical lattice clock," *Nature*, 542, 7639 [Dec. 2016], pp. 66-70, ISSN: 1476-4687, DOI: 10.1038/nature20811, http://dx.doi.org/10.1038/nature20811.

Kruse, I., K. Lange, J. Peise, B. Lücke, L. Pezzè, J. Arlt, W. Ertmer, C. Lisdat, L. Santos, A. Smerzi, and C. Klempt

2016 "Improvement of an Atomic Clock using Squeezed Vacuum," *Phys. Rev. Lett.*, 117 [14 Sept. 2016], p. 143004, DOI: 10.1103/PhysRevLett.117.143004, https://link.aps.org/doi/10.1103/PhysRevLett.117.143004.

Kunkel, Philipp, Maximilian Prüfer, Stefan Lannig, Rodrigo Rosa-Medina, Alexis Bonnin, Martin Gärttner, Helmut Strobel, and Markus K Oberthaler

2019 "Simultaneous readout of noncommuting collective spin observables beyond the standard quantum limit," *Physical review letters*, 123, 6, p. 063603.

Ladd, Thaddeus D, Fedor Jelezko, Raymond Laflamme, Yasunobu Nakamura, Christopher Monroe, and Jeremy Lloyd O'Brien

2010 "Quantum computers," *nature*, 464, 7285, pp. 45-53.

Lamporesi, G., A. Bertoldi, L. Cacciapuoti, M. Prevedelli, and G. M. Tino

2008 "Determination of the Newtonian Gravitational Constant Using Atom Interferometry," *Phys. Rev. Lett.*, 100 [5 Feb. 2008], p. 050801, DOI: 10.1103/PhysRevLett.100.050801, https://link.aps.org/doi/10.1103/PhysRevLett.100.050801.

Lan, Zhihao, Nathan Goldman, Alejandro Bermudez, Wenshu Lu, and P Öhberg

2011 "Dirac-Weyl fermions with arbitrary spin in two-dimensional optical super-lattices," *Physical Review B—Condensed Matter and Materials Physics*, 84, 16, p. 165115.

Lanyon, Benjamin P, Marco Barbieri, Marcelo P Almeida, Thomas Jennewein, Timothy C Ralph, Kevin J Resch, Geoff J Pryde, Jeremy L O'brien, Alexei Gilchrist, and Andrew G White

2009 "Simplifying quantum logic using higher-dimensional Hilbert spaces," *Nature Physics*, 5, 2, pp. 134-140.

Le Targat, Rodolphe, Xavier Baillard, Mathilde Fouché, Anders Brusch, Olivier Tcherbakoff, <? format?> Giovanni D Rovera, and Pierre Lemonde

2006 "Accurate optical lattice clock with Sr 87 atoms," *Physical Review Letters*, 97, 13, p. 130801.

Lee, P J, K-A Brickman, L Deslauriers, P C Haljan, L-M Duan, and C Monroe

2005 "Phase control of trapped ion quantum gates," *Journal of Optics B: Quantum and Semiclassical Optics*, 7, 10 [Sept. 2005], S371-S383, ISSN: 1741-3575, DOI: 10.1088/1464-4266/7/10/025, http://dx.doi.org/10.1088/1464-4266/7/10/025.

Li, Linshu, Chang-Ling Zou, Victor V. Albert, Sreraman Muralidharan, S. M. Girvin, and Liang Jiang

2017 "Cat Codes with Optimal Decoherence Suppression for a Lossy Bosonic Channel," *Phys. Rev. Lett.*, 119 [3 July 2017], p. 030502, DOI: 10.1103/PhysRevLett.119.030502, https://link.aps.org/doi/10.1103/PhysRevLett.119.030502.

Li, Tracy, Lucia Duca, Martin Reitter, Fabian Grusdt, Eugene Demler, Manuel Endres, Monika Schleier-Smith, Immanuel Bloch, and Ulrich Schneider

2016 "Bloch state tomography using Wilson lines," *Science*, 352, 6289, pp. 1094-1097, DOI: 10.1126/science.aad5812, eprint: https://www.science.org/doi/pdf/10.1126/science.aad5812, https://www.science.org/doi/abs/10.1126/science.aad5812.

Lis, Joanna W., Aruku Senoo, William F. McGrew, Felix Rönchen, Alec Jenkins, and Adam M. Kaufman

2023 *Mid-circuit operations using the omg-architecture in neutral atom arrays*, arXiv: 2305.19266 [quant-ph], https://arxiv.org/abs/2305.19266.

Lisdat, Christian, Gesine Grosche, N Quintin, C Shi, SMF Raupach, C Grebing, D Nicolodi, F Stefani, A Al-Masoudi, S Dörscher, et al.

2016   "A clock network for geodesy and fundamental science," *Nature communications*, 7, 1, p. 12443.

Litvinov, Andrea

2023   *Manipulation of the Nuclear Spin States of 87 Sr in Degenerate SU(N)-Symmetric Fermi Gases*, Thesis, Sorbonne Paris Nord, https://sorbonne-paris-nord.hal.science/tel-04201342.

Ludlow, Andrew D, Martin M Boyd, Jun Ye, Ekkehard Peik, and Piet O Schmidt

2015   "Optical atomic clocks," *Reviews of Modern Physics*, 87, 2, pp. 637-701.

Ludlow, Andrew D, T Zelevinsky, GK Campbell, S Blatt, MM Boyd, Marcio HG de Miranda, MJ Martin, JW Thomsen, Seth M Foreman, Jun Ye, et al.

2008   "Sr lattice clock at 1× 10–16 fractional uncertainty by remote optical evaluation with a Ca clock," *Science*, 319, 5871, pp. 1805-1808.

Madjarov, Ivaylo S., Amanda Cooper, Alex L. Shaw, Jacob P. Covey, Vladimir Schkolnik, Tae Hoon Yoon, Jason R. Williams, and Manuel Endres

2020   "High-Fidelity Entanglement and Detection of Alkaline-Earth Rydberg Atoms," *Nature*, 580, pp. 532-536, DOI: 10.1038/s41586-020-3006-1, https://www.nature.com/articles/s41586-020-3006-1.

Mandel, Olaf, Markus Greiner, Artur Widera, Tim Rom, Theodor W. Hänsch, and Immanuel Bloch

2003   "Coherent Transport of Neutral Atoms in Spin-Dependent Optical Lattice Potentials," *Phys. Rev. Lett.*, 91 [1 July 2003], p. 010407, DOI: 10.1103/PhysRevLett.91.010407, https://link.aps.org/doi/10.1103/PhysRevLett.91.010407.

Manzano, Daniel

2020   "A short introduction to the Lindblad master equation," *AIP Advances*, 10, 2 [Feb. 2020], ISSN: 2158-3226, DOI: 10.1063/1.5115323, http://dx.doi.org/10.1063/1.5115323.

Marston, J Brad and Ian Affleck

1989   "Large-n limit of the Hubbard-Heisenberg model," *Physical Review B*, 39, 16, p. 11538.

Martinez de Escobar, YN, PG Mickelson, P Pellegrini, SB Nagel, A Traverso, M Yan, R Côté, and TC Killian

2008   "Two-photon photoassociative spectroscopy of ultracold Sr 88," *Physical Review A—Atomic, Molecular, and Optical Physics*, 78, 6, p. 062708.

Maurer, Peter Christian, Georg Kucsko, Christian Latta, Liang Jiang, Norman Ying Yao, Steven D Bennett, Fernando Pastawski, David Hunger, Nicholas Chisholm, Matthew Markham, et al.

2012   "Room-temperature quantum bit memory exceeding one second," *Science*, 336, 6086, pp. 1283-1286.

Mazurenko, Anton, Christie S Chiu, Geoffrey Ji, Maxwell F Parsons, Márton Kanász-Nagy, Richard Schmidt, Fabian Grusdt, Eugene Demler, Daniel Greif, and Markus Greiner

2017   "A cold-atom Fermi–Hubbard antiferromagnet," *Nature*, 545, 7655, pp. 462-466.

MOGLabs

n.d.   *Tunable Cateye Lasers (CEL)*, https://www.moglabs.com/products/tunable-lasers/cateye-laser, Accessed: 2025-02-21.

Morishita, H., S. Kobayashi, M. Fujiwara, H. Kato, T. Makino, S. Yamasaki, and N. Mizuochi

2020   "Room Temperature Electrically Detected Nuclear Spin Coherence of NV Centres in Diamond," en, *Scientific Reports*, 10, 1 [Jan. 2020], p. 792, ISSN: 2045-2322, DOI: 10.1038/s41598-020-57569-8, https://www.nature.com/articles/s41598-020-57569-8 [visited on 07/17/2024].

Mukherjee, Bijit, Jeremy M Hutson, and Kaden RA Hazzard

2024   "SU (N) magnetism with ultracold molecules," *arXiv preprint arXiv:2404.15957*.

Muralidharan, Sreraman, Chang-Ling Zou, Linshu Li, Jianming Wen, and Liang Jiang

2017   "Overcoming erasure errors with multilevel systems," *New Journal of Physics*, 19, 1, p. 013026.

Neeley, Matthew, Markus Ansmann, Radoslaw C Bialczak, Max Hofheinz, Erik Lucero, Aaron D O'Connell, Daniel Sank, Haohua Wang, James Wenner, Andrew N Cleland, et al.

2009   "Emulation of a quantum spin with a superconducting phase qudit," *Science*, 325, 5941, pp. 722-725.

Norcia, M. A., W. B. Cairncross, K. Barnes, P. Battaglino, A. Brown, M. O. Brown, K. Cassella, C.-A. Chen, R. Coxe, D. Crow, J. Epstein, C. Griger, A. M. W. Jones, H. Kim, J. M. Kindem, J. King, S. S. Kondov, K. Kotru, J. Lauigan, M. Li, M. Lu, E. Megidish, J. Marjanovic, M. McDonald, T. Mittiga, J. A. Muniz, S. Narayanaswami, C. Nishiguchi, R. Notermans, T. Paule, K. A. Pawlak, L. S. Peng, A. Ryou, A. Smull, D. Stack, M. Stone, A. Sucich, M. Urbanek, R. J. M. van de Veerdonk, Z. Vendeiro, T. Wilkason, T.-Y. Wu, X. Xie, X. Zhang, and B. J. Bloom

    2023   "Midcircuit Qubit Measurement and Rearrangement," *Physical Review X*, 13, 4 [Nov. 2023], ISSN: 2160-3308, DOI: 10.1103/physrevx.13.041034, http://dx.doi.org/10.1103/PhysRevX.13.041034.

Outeiral, Carlos, Martin Strahm, Jiye Shi, Garrett M Morris, Simon C Benjamin, and Charlotte M Deane

    2021   "The prospects of quantum computing in computational molecular biology," *Wiley Interdisciplinary Reviews: Computational Molecular Science*, 11, 1, e1481.

Pagano, Guido, Marco Mancini, Giacomo Cappellini, Pietro Lombardi, Florian Schäfer, Hui Hu, Xia-Ji Liu, Jacopo Catani, Carlo Sias, Massimo Inguscio, and Leonardo Fallani

    2014   "A one-dimensional liquid of fermions with tunable spin," *Nature Physics*, 10, 3 [Feb. 2014], pp. 198-201, ISSN: 1745-2481, DOI: 10.1038/nphys2878, http://dx.doi.org/10.1038/nphys2878.

Park, Jee Woo, Zoe Z Yan, Huanqian Loh, Sebastian A Will, and Martin W Zwierlein

    2017   "Second-scale nuclear spin coherence time of ultracold 23Na40K molecules," *Science*, 357, 6349, pp. 372-375.

Pearson, Karl

    1896   "Mathematical Contributions to the Theory of Evolution. III. Regression, Heredity, and Panmixia," *Philosophical Transactions of the Royal Society of London. Series A, Containing Papers of a Mathematical or Physical Character*, 187, pp. 253-318.

Peters, Achim, Keng Yeow Chung, and Steven Chu

    2001   "High-precision gravity measurements using atom interferometry," *Metrologia*, 38, 1, p. 25.

Poli, Nicola, F-Y Wang, MG Tarallo, A Alberti, Marco Prevedelli, and GM Tino

2011 "Precision Measurement of Gravity with Cold Atoms in an Optical Lattice<? format?> and Comparison with a Classical Gravimeter," *Physical review letters*, 106, 3, p. 038501.

Pucher, Sebastian, Valentin Klüsener, Felix Spriestersbach, Jan Geiger, Andreas Schindewolf, Immanuel Bloch, and Sebastian Blatt

2024 "Fine-structure qubit encoded in metastable strontium trapped in an optical lattice," *Physical Review Letters*, 132, 15, p. 150605.

Radiant Dyes Laser & Accessories GmbH

n.d. *NarrowDiode Laser*, https://www.radiant-dyes.com/index.php/products/laser/diode-laser, Accessed: 2025-02-21.

Ramsey, Norman F.

1949 "A New Molecular Beam Resonance Method," *Phys. Rev.*, 76 [7 Oct. 1949], pp. 996-996, DOI: 10.1103/PhysRev.76.996, https://link.aps.org/doi/10.1103/PhysRev.76.996.

Saffman, Mark

2016 "Quantum computing with atomic qubits and Rydberg interactions: progress and challenges," *Journal of Physics B: Atomic, Molecular and Optical Physics*, 49, 20, p. 202001.

Safronova, MS and UI Safronova

2011 "Critically evaluated theoretical energies, lifetimes, hyperfine constants, and multipole polarizabilities in Rb 87," *Physical Review A*, 83, 5, p. 052508.

Safronova, MS, UI Safronova, and SG Porsev

2013 "Polarizabilities, Stark shifts, and lifetimes of the In atom," *Physical Review A—Atomic, Molecular, and Optical Physics*, 87, 3, p. 032513.

Santarelli, G., Ph. Laurent, P. Lemonde, A. Clairon, A. G. Mann, S. Chang, A. N. Luiten, and C. Salomon

1999 "Quantum Projection Noise in an Atomic Fountain: A High Stability Cesium Frequency Standard," *Phys. Rev. Lett.*, 82 [23 June 1999], pp. 4619-4622, DOI: 10.1103/PhysRevLett.82.4619, https://link.aps.org/doi/10.1103/PhysRevLett.82.4619.

Schäffer, Stefan A, Mikkel Tang, Martin R Henriksen, Asbjørn A Jørgensen, Bjarke TR Christensen, and Jan W Thomsen

2020 "Lasing on a narrow transition in a cold thermal strontium ensemble," *Physical Review A*, 101, 1, p. 013819.

Schulte, T, S Drenkelforth, G Kleine Büning, W Ertmer, J Arlt, M Lewenstein, and L Santos

2008 "Dynamics of Bloch oscillations in disordered lattice potentials," *Physical Review A—Atomic, Molecular, and Optical Physics*, 77, 2, p. 023610.

Shi, C., J.-L. Robyr, U. Eismann, M. Zawada, L. Lorini, R. Le Targat, and J. Lodewyck

2015 "Polarizabilities of the 87Sr clock transition," *Phys. Rev. A*, 92 [1 July 2015], p. 012516.

Simon, Jonathan, Waseem S Bakr, Ruichao Ma, M Eric Tai, Philipp M Preiss, and Markus Greiner

2011 "Quantum simulation of antiferromagnetic spin chains in an optical lattice," *Nature*, 472, 7343, pp. 307-312.

Soltamov, V. A., C. Kasper, A. V. Poshakinskiy, A. N. Anisimov, E. N. Mokhov, A. Sperlich, S. A. Tarasenko, P. G. Baranov, G. V. Astakhov, and V. Dyakonov

2019 "Excitation and coherent control of spin qudit modes in silicon carbide at room temperature," en, *Nature Communications*, 10, 1 [Apr. 2019], p. 1678, ISSN: 2041-1723, DOI: 10.1038/s41467-019-09429-x, https://www.nature.com/articles/s41467-019-09429-x [visited on 07/17/2024].

Steck, Daniel A

2001 "Rubidium 87 D line data."

Stellmer, Simon, Rudolf Grimm, and Florian Schreck

2011a "Detection and manipulation of nuclear spin states in fermionic strontium," *Phys. Rev. A*, 84 [4 Oct. 2011], p. 043611, DOI: 10.1103/PhysRevA.84.043611, https://link.aps.org/doi/10.1103/PhysRevA.84.043611.

2011b "Detection and manipulation of nuclear spin states in fermionic strontium," *Physical Review A—Atomic, Molecular, and Optical Physics*, 84, 4, p. 043611.

Sun, Hui, Bing Yang, Han-Yi Wang, Zhao-Yu Zhou, Guo-Xian Su, Han-Ning Dai, Zhen-Sheng Yuan, and Jian-Wei Pan

2021 "Realization of a bosonic antiferromagnet," *Nature Physics*, 17, 9 [July 2021], pp. 990-994, ISSN: 1745-2481, DOI: 10.1038/s41567-021-01277-1, http://dx.doi.org/10.1038/s41567-021-01277-1.

Sun, Wei, Bao-Zong Wang, Xiao-Tian Xu, Chang-Rui Yi, Long Zhang, Zhan Wu, Youjin Deng, Xiong-Jun Liu, Shuai Chen, and Jian-Wei Pan

2017 "Highly Controllable and Robust 2D Spin-Orbit Coupling for Quantum Gases." *Physical review letters*, 121 15, p. 150401, https://api.semanticscholar.org/CorpusID:53103342.

Taie, Shintaro, Yosuke Takasu, Seiji Sugawa, Rekishu Yamazaki, Takuya Tsujimoto, <? format?> Ryo Murakami, and Yoshiro Takahashi

2010 "Realization of a SU (2)× SU (6) system of fermions in a cold atomic gas," *Physical review letters*, 105, 19, p. 190401.

Taie, Shintaro, Yosuke Takasu, Seiji Sugawa, Rekishu Yamazaki, Takuya Tsujimoto, Ryo Murakami, and Yoshiro Takahashi

2010 "Realization of a SU(2) × SU(6) System of Fermions in a Cold Atomic Gas," *Phys. Rev. Lett.*, 105 [19 Nov. 2010], p. 190401, DOI: 10.1103/PhysRevLett.105.190401, https://link.aps.org/doi/10.1103/PhysRevLett.105.190401.

Taie, Shintaro, Rekishu Yamazaki, Seiji Sugawa, and Yoshiro Takahashi

2012 "An SU(6) Mott insulator of an atomic Fermi gas realized by large-spin Pomeranchuk cooling," *Nature Physics*, 8, 11 [Sept. 2012], pp. 825-830, ISSN: 1745-2481, DOI: 10.1038/nphys2430, http://dx.doi.org/10.1038/nphys2430.

Tey, Meng Khoon, Simon Stellmer, Rudolf Grimm, and Florian Schreck

2010 "Double-degenerate Bose-Fermi mixture of strontium," *Phys. Rev. A*, 82 [1 July 2010], p. 011608, DOI: 10.1103/PhysRevA.82.011608, https://link.aps.org/doi/10.1103/PhysRevA.82.011608.

Varshalovich, D. A., A. N. Moskalev, and V. K. Khersonskii

1988 *Quantum Theory of Angular Momentum*, DOI: 10.1142/0270.

Waldherr, Gerald, Johannes Beck, Philipp Neumann, RS Said, M Nitsche, ML Markham, DJ Twitchen, J Twamley, Fedor Jelezko, and J Wrachtrup

2012 "High-dynamic-range magnetometry with a single nuclear spin in diamond," *Nature nanotechnology*, 7, 2, pp. 105-108.

Wikipedia contributors

2025 *Double-sideband suppressed-carrier transmission — Wikipedia, The Free Encyclopedia*, [Online; accessed 28-February-2025], https://en.wikipedia.org/wiki/Double-sideband_suppressed-carrier_transmission.

Wineland, D. J., J. J. Bollinger, W. M. Itano, and D. J. Heinzen

1994 "Squeezed atomic states and projection noise in spectroscopy," *Phys. Rev. A*, 50 [1 July 1994], pp. 67-88, DOI: `10.1103/PhysRevA.50.67`, `https://link.aps.org/doi/10.1103/PhysRevA.50.67`.

Yip, S-K and Tin-Lun Ho

1999 "Zero sound modes of dilute Fermi gases with arbitrary spin," *Physical Review A*, 59, 6, p. 4653.

Zener, Clarence and Ralph Howard Fowler

1932 "Non-adiabatic crossing of energy levels," *Proceedings of the Royal Society of London. Series A, Containing Papers of a Mathematical and Physical Character*, 137, 833, pp. 696-702, DOI: `10.1098/rspa.1932.0165`, eprint: `https://royalsocietypublishing.org/doi/pdf/10.1098/rspa.1932.0165`, `https://royalsocietypublishing.org/doi/abs/10.1098/rspa.1932.0165`.

Zhang, Xiaohang, Michael Bishof, Sarah L Bromley, Christina V Kraus, Marianna S Safronova, Peter Zoller, Ana Maria Rey, and J Ye

2014 "Spectroscopic observation of SU (N)-symmetric interactions in Sr orbital magnetism," *science*, 345, 6203, pp. 1467-1473.